Alma Mater Studiorum - Università di Bologna

SCUOLA DI SCIENZE

Dipartimento di Chimica Industriale"Toso Montanari"

Corso di Laurea Magistrale in

Chimica Industriale

Classe LM-71 - Scienze e Tecnologie della Chimica Industriale

Synthesis, characterisation, and application of new Cu-based Metal-Organic Frameworks (MOFs)

Tesi di laurea sperimentale

CANDIDATO

Michele Coi

RELATORE

Prof.ssa Maria Cristina Cassani

CORRELATORE

Dott.ssa Francesca Gambassi

Prof.ssa Barbara Ballarin

Prof. Daniele Nanni

Anno Accademico 2020-2021

ABSTRACT

This work originates from a previous project of the research group I worked with. In said project, a new propargylcarbamate-functionalised isophthalate organic ligand was synthesised and used for the preparation of a new Cu-based Metal-Organic Framework (MOF), named [Cu(1,3-YBDC)]·$x$$H_2O$. Due to the ability of the proprgylcarbmate group to capture Au(III) ions in solution and to reduce them to Au(0), this new MOF was intended to be used as a support for gold nanoparticles, to be used in applications such as electrocatalysis and nitrite sensing. Unfortunately, due to the low porosity and surface area of the material, the capture of Au(III) with [Cu(1,3-YBDC)]·$x$$H_2O$ occurs only in small extent, and the electro-assisted reduction occurs only partially, resulting in the presence of all the oxidation states of Au (0, I and III) on the external surface of the material.

This work shows the synthesis and characterisation of a new organic ligand, named H_2YL80, which maintains the propargylcarbamate functionality of the previous one but also possesses a larger aromatic moiety, envisaging the possibility to obtain a corresponding Cu-based MOF with higher porosity and surface area.

The reaction of the new ligand with $Cu(NO_3)_2 \cdot 2.5H_2O$ to obtain a new Cu-based MOF was studied under different conditions, in attempt to synthesise the new material in a crystalline shape which allows the characterisation through X-ray spectroscopy measurements. Despite the numerous attempts, the best results obtained consist in polycrystalline materials.

In parallel to those activities, the reactivity of [Cu(1,3-YBDC)]·$x$$H_2O$ towards $HAuCl_4$ was studied, to see if the propargylcarbamate functionalities could reduce Au(III) to Au(0) without the aid of electrochemical devices.

Finally, the alternative application of [Cu(1,3-YBDC)]·$x$$H_2O$ as an adsorbent material for organic dyes was studied by testing the adsorption capacity of the material for Methylene Blue in different conditions.

INDEX

Chapter 1

1 Introduction

1.1 Context of the work

In past studies, the research group I worked with during my thesis has shown that propargylcarbamate group [-NH-C(O)O-CH_2C≡CH], anchored on different oxide supports such as SiO_2, Al_2O_3, TiO_2, Fe_3O_4 (Fig. 1.1) is capable of reducing Au(III) ions to Au(0), yielding supported Gold Nanoparticles (AuNPs) without the addition of any external reducing and/or stabilizing agent (Fig 1.2).[1,2]

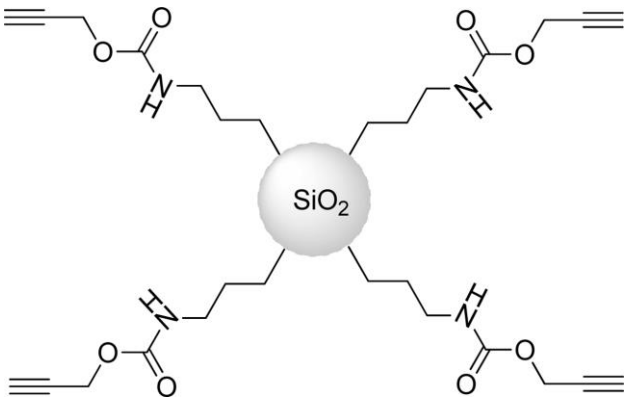

Fig. 1.1: Alkyne-modified silica nanoparticle (SiO_2@Yne).[3]

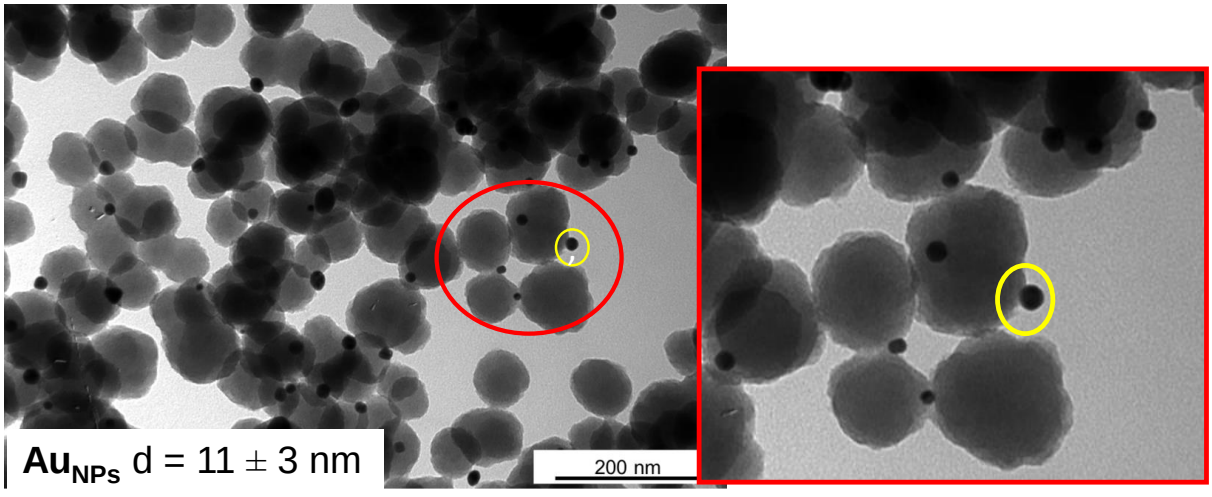

Fig 1.2: TEM image and enlargement of AuNPs supported on silica nanoparticles.

More recently, the research group explored the possibility of anchoring the propargylcarbamate fragment on different supports, such as Metal-Organic Frameworks (MOFs). The functionalization of a MOF with the propargylcarbamate group could provide a

dense, even, and possibly highly symmetric distribution of the reactive alkyne functionality all over the material. Additionally, the porosity of the material and the presence of the metal nodes could influence the reactivity of the alkyl group, and induce different effects on the ensuing gold nanoparticles, compared to when the functional group is attached onto the oxidic surfaces previously cited.

The research group successfully designed and synthesized a new propargylcarbamate functionalised isophtalate ligand, named 5-(2-{[(prop-2-yn-1-yloxy)carbonyl]-amino}ethoxy)isophthalic acid (Fig.1.3 A), abbreviated in 1,3-H_2YBDC, where Y stands for the pendant alkYne and BDC for benzene dicarboxylate. The ligand was used to prepare a Cu-based MOF, named [Cu(1,3-YBDC)]·$x$$H_2O$. The MOF was structurally characterized. It has been shown that the solid [Cu(1,3-YBDC)]·$x$$H_2O$ (x~2) phase contains a complex network of 5-substituted isophthalate anions bound to Cu(II) centres, whose structure belongs to the common paddlewheel dimeric fragments (also known as "Chinese lantern") of $Cu_2(\mu\text{-}COO)_4(D)_2$ formulation, D being a neutral Lewis base, typically bound through a N or O atom. The dimer shows a short Cu···Cu distance (2.633 Å), in line with the data reported for analogous structures.[4]

The peculiarity of this particular structure is that the apical D atom in [Cu(1,3-YBDC)]·$x$$H_2O$ belongs to the carbonyl oxygen atom of the long propargyl carbamate residue (Fig 1.3 B). Such an extra coordination by the propargylcarbamate groups drastically reduces the porosity of the MOF.[5] In fact, the Langmuir surface area was found to be 18.4±0.9 m^2/g, while the BET surface area was 14.5 ± 0.8 $m^{2/}g$. Those are extremely low values considering that there are reported BET areas for Cu-BTC MOFs above 1000 m^2/g.[6]

Several experiments were performed to test the ability of the material to capture Au(III). The results showed that Au(III) is indeed captured by the MOF but to only a small extent (ca. 0.3 wt% of adsorbed gold). Also, the reduction of Au(III) occurs only partially, leading to a material in which all the gold oxidation states (III, I and 0) are present, in ratio depending on the reaction conditions.

The electrochemical properties of the Cu-MOF were studied through cyclic-voltammetry measurements in different electrolyte solutions, performed on Glassy-Carbon electrodes modified by drop-casting a MOF suspension in ethanol on its surface yielding a GC/Cu-YBDC electrode (hereafter abbreviated **GC/Cu-MOF**) as shown in Fig. 1.4. The modified electrodes were then tested as nitrite sensors.

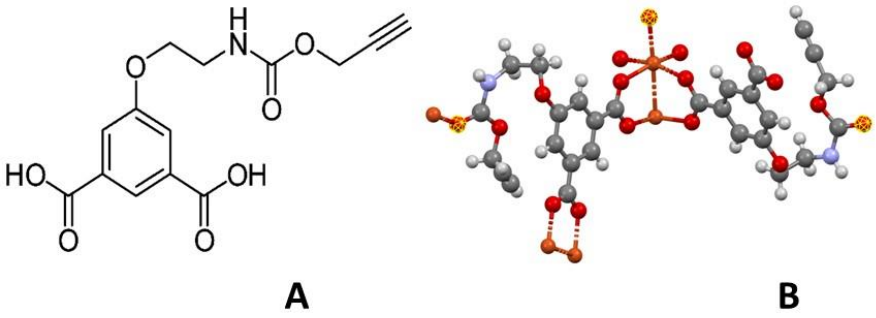

Fig. 1.3: (A) A conventional sketch of the 1,3-H_2YBDC moiety, showing molecular connectivity; (**B**) a 3D drawing of the Cu-YBDC paddlewheel fragment and the location of the carbamate carbonyl oxygen atoms (highlighted in yellow) completing the Cu(II) coordination through C=O···Cu bonds. Atomic coordinates are taken from ref [4] Color codes: Carbon (black); Hydrogen (white); Nitrogen (blue), Oxygen (red) and Copper (orange). The dashed bonds address the weak intermetallic interaction and the apical carbamate coordination mode.

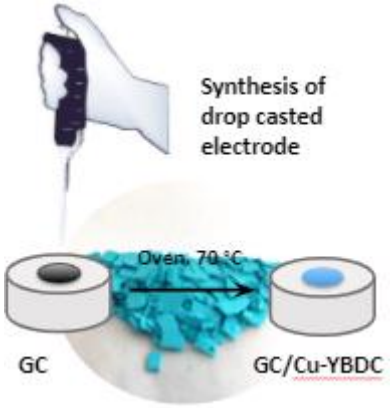

Fig. 1.4: Modification of GC electrodes by drop-casting of a solution of a Cu-YBDC suspension in ethanol, yielding a GC/CU-YBDC electrode.

Due to the affinity of gold to the alkyne group of the MOF's linker, the GC/Cu-MOF electrode was successively modified through AuNPs incorporation. The electrode named **GC/Cu-MOF/Au** was prepared by making the MOF deposited on the electrode surface to adsorb Au(III) from a $HAuCl_4$ solution and then, after washing the electrode with ethanol, the Au(III) retained by the MOF was reduced to Au(0) through the application of a potential of 0.05 V. The GC/Cu-MOF/Au electrode was also characterized and tested for nitrite detection.

Due to the low surface area and pore volume of the Cu-MOF, the modified electrode showed a higher peak potential and a lower peak current for the nitrite oxidation reaction than the bare glassy carbon electrode. Upon incorporation of AuNPs within the MOF through electrodeposition, the nitrite sensing performance of the modified electrode improved beyond that of the glassy carbon electrode. Cyclic voltammetry and EIS characterization of the

electrodes confirmed the semiconductor behaviour of the MOF and the ability of AuNPs to compensate for that by increasing the charge transfer rate. However, due to the drop-casting technique employed in the electrode modification, they showed poor reproducibility in terms of nitrite sensing performance.

1.2 Objectives

The first aim of this work has been the design, synthesis, and characterization of a new organic ligand, named H_2YL80, (where Y stands for the pendant alkyne and L80 indicates the similarity of the aromatic moiety of the ligand with the one of the ligand H_3L80 found in literature[7]) and the corresponding Cu-[YL80] MOF. The new organic linker maintains the propargylcarbamate functionality and the two carboxylic acid groups of 1,3-H_2YBDC but provides a larger spacer between the carboxylic acid groups by adding two benzene rings on the aromatic moiety of the molecule (Fig. 1.5). This new design of the ligand was chosen envisaging that the larger, more rigid and more hindered spacer could prevent the coordination of the propargylcarbamate chains to the Cu(II) ions, in order to achieve a higher porosity in the new MOF.

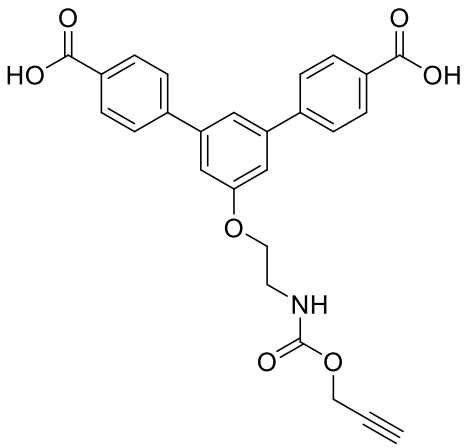

Fig. 1.5: Structure of the new H_2YL80 ligand.

In addition, this work will also cover the study of the chemical reduction of Au(III) performed, without the aid of electrochemical devices, by the propargylcarbamate groups on the surface of the previous MOF [Cu(1,3-YBDC)]·$x$$H_2O$.

In parallel to these activities, this thesis will also show the studies carried on by the group to explore the possible application of [Cu(1,3-YBDC)]·$x$$H_2O$ as an adsorbent material for dyes. The adsorption of dyes is currently a topic of great interest in the field of wastewaters

treatments, and MOFs, thanks to their unique structures and properties, are among the materials that are receiving the greatest attention in said scope.

1.3 Introduction to Metal-Organic Frameworks (MOFs)

1.3.1 Definition

Metal-Organic Frameworks (MOFs), also known as Porous Coordination Polymers (PCPs), are a class of porous, crystalline materials that derive from the assembling of multitopic organic ligands and metal centres (nodes).[8] The organic ligands act as linkers between the nodes (which can consist of metal ions or metallic clusters) to yield 3D coordination structures.

1.3.2 Brief History

Coordination polymers became popular in 1990, when Hoskin and Robson published a paper[9] in which they suggested the existence of a "scaffolding-like" materials that could be afforded by linking together metal centres and rod-like connecting units. The authors had taken into account the fact that such polymerizing systems could lead to disordered amorphous materials of indefinite composition, but they also stated that the formation of highly ordered self-assembly crystalline structures was probable enough to make some trial synthesis worthwhile. Since then, MOFs have become an extremely vibrant topic, with hundreds of papers published every year about newly discovered structures (Fig. 1.6) and applications for those materials.

The term "MOF" was coined by Yaghi et al. in 1995[10] but the first review about coordination polymers dates back to 1964. The study of the MOFs as we know them today has evolved from coordination chemistry and solid state/zeolite chemistry, driven by the objective of creating open metal-organic extended structures of which the pores could be functionalised in order to perform chemistry with them.[11]

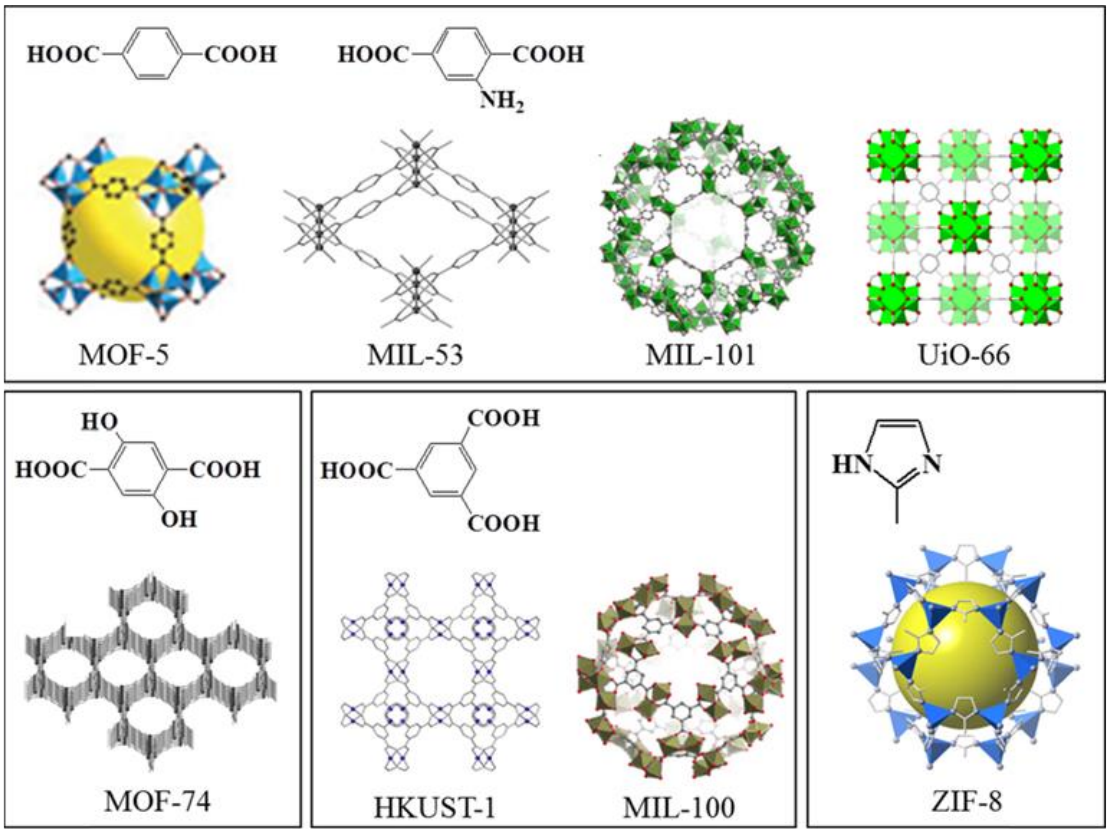

Fig. 1.6: Representative MOFs structures.[6]

1.3.3 Structure and properties

As stated in the definition, MOFs are the resulting combination of two different building units, respectively the organic linkers and the inorganic components, often referred to as Secondary Building Units (SBUs). The organic linkers are characterised by the presence of binding groups, such as carboxylates (by far the most common),[7] phosphates, pyrazolates ecc. The SBUs consist of metal ions (or polynuclear clusters of metal ions), and the binding groups of the organic linkers. These SBUs provide directionality, and, in combination with the strong bonding between the constituents, endow the resulting MOFs with high mechanical, architectural, and chemical stability. SBUs are commonly formed *in situ*, thus allowing for the slow and reversible assembly of the overall structure, error correction, and consequently the formation of highly crystalline products.[12]

Seeing that the crystallinity of the MOFs is tightly related to the reversibility of the bonds between the linker and the metal ions/clusters, it follows that increasing the strength of said bonds leads to more difficulties in the crystallisation of the MOFs (Fig. 1.7). On the other hand, too weak metal-linker bonds may have negative consequences on the chemical and architectural stability of the products. This problem has been quite common until the first half

of the 1990s, when neutral donor linkers were used to prepare coordination network. The turning point was the replacement of neutral linkers with charged chelating ones. As mentioned earlier, the most common class of ligands consists of carboxylate-based ligands, which provide four advantages over neutral donors: (i) the charged carboxylates neutralize the positive charges of the metal nodes, thus allowing for the formation of neutral frameworks and obviating the need for counterions; (ii) their chelating ability provides more structural rigidity and directionality; (iii) they favour the formation of polynuclear clusters (SBUs) with a fixed overall coordination geometry and connectivity; (iv) the strong bonding between the linkers and the metal centres of the SBUs results in MOFs with high thermal, mechanical, and chemical stability.

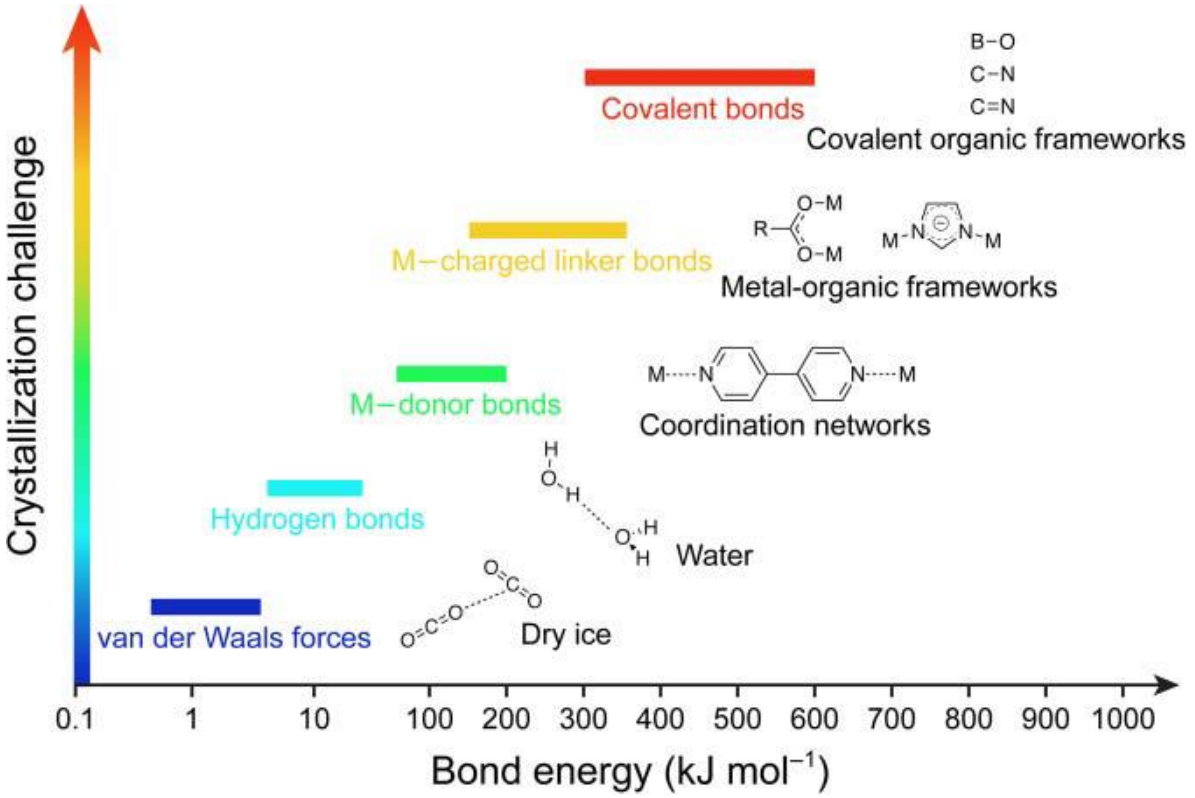

Fig. 1.7: Comparison of the strength of different types of interactions ranging from weak (blue and cyan, van der Waals forces, and hydrogen bonding), to intermediate (green, metal–donor bonds), to strong (yellow and red, metal-charged linker and covalent bonds, respectively). The challenge in crystallizing extended structures based on these interactions increases with increasing bond strength.[12]

1.3.4 Methods of synthesis

A crucial aspect in the study of MOFs is the variety of synthetic methods that can be used to obtain these materials. In most cases, the use of different methods or reaction conditions on the same starting materials can lead to different products.[13,14]

The most common method, so much so that is commonly referred to as "conventional synthesis", consists in carrying out the reaction by conventional electrical heating (Fig. 1.8). For this method, two different sub-categories can be defined: *solvothermal synthesis*, where the reaction is carried at autogenous pressure, in a closed vessel, above the boiling point of the solvent, and *nonsolvothermal*, where the reaction takes place at ambient pressure under the boiling point of the solvent.[13] The most important parameters are the initial concentration of the reactants and the solvent used, which determines the range of temperature that can be used.

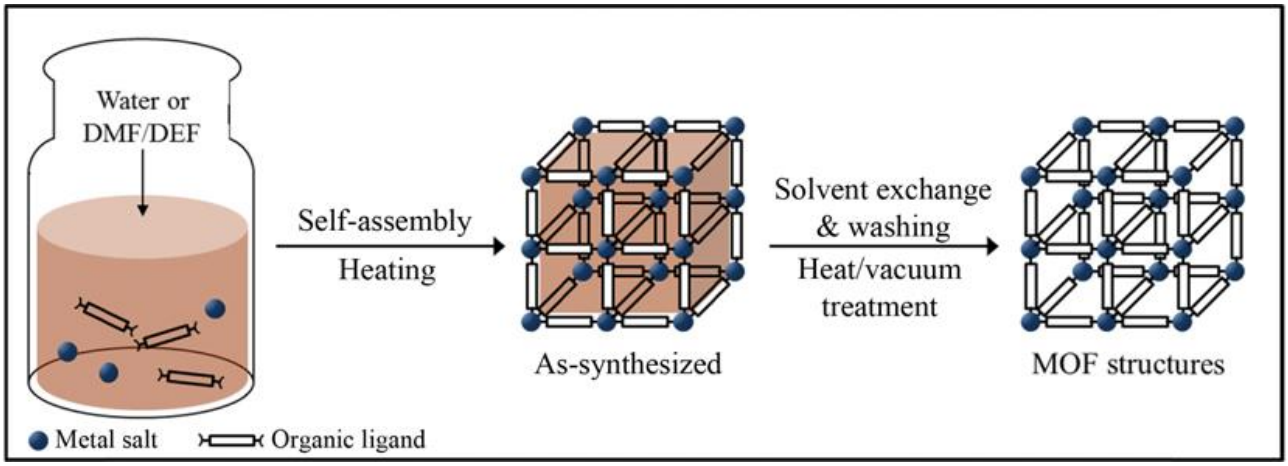

Fig. 1.8: Conventional synthesis of MOFs.[6]

There are also many methods that fall under the category of "non-conventional synthesis". Among the most common ones we find microwave-assisted synthesis (where the microwaves are used to heat the reaction mixtures), electrochemical synthesis (in which the metal ions are introduced continuously by anodic dissolution rather than being added in form of salts), mechanochemical synthesis (solvent-free method in which the reaction is induced by mechanical forces, by grinding the reactants together), sonochemical synthesis (that consists in inserting the reaction mixture inside an ultrasonic bath to provide the necessary energy) and interfacial synthesis (where the reaction takes place at the interface between two different solutions, one containing the metal salt and one containing the organic linker).[6]

1.3.5 Activation of MOFs

During the synthesis of MOFs, the presence of guest molecules (solvents, ligand excess etc…) trapped inside the pores is inevitable, leading to a reduction of the porosity and the surface area of the materials. Since permanent porosity is required for MOFs to be considered viable

materials,[15] numerous methods have been developed to remove those guest molecules, and thus activate the MOFs.

Sometimes the removal of the guest molecules is achieved by simple heating under vacuum, but usually the synthesis of MOFs requires high-boiling solvents, such as *N*,*N*-dimethylformamide (DMF) or dimethyl sulfoxide (DMSO). In those cases, thermal activation could cause significant capillary forces and surface tension[16] which could yield fully or partially collapsed frameworks.[16] In those cases, before applying thermal activation it is common practice to perform a solvent-exchange routine, by soaking the MOF in a low-boiling solvent.[17] The process of activating the MOFs by heating under vacuum is also known as "conventional activation".

Following the logic of avoiding high surface tension and operating under milder conditions, the use of supercritical CO_2 to activate the MOFs represents a valid alternative to conventional activation. The process consists in the exchanging of the solvent molecules with liquid CO_2, below its critical temperature (31 °C) and above its critical pressure (73 bar). Then, the evaporation of CO_2 is carried out in its supercritical state, by depressurizing the CO_2 above its critical temperature (Fig. 1.9), which drastically minimizes the surface tension that would normally happen during a conventional liquid-gas transition phase.[18]

Similarly to supercritical CO_2 drying, another technique that avoids the liquid-gas transition phase is freeze drying. In this case, the initial solvent is exchanged with a high-freezing-point solvent (e.g., benzene[16]) and cooled down to its freezing point. Then, the solvent can be removed under vacuum through sublimation, effectively avoiding the surface tension that would happen during liquid-gas transition phase.[18]

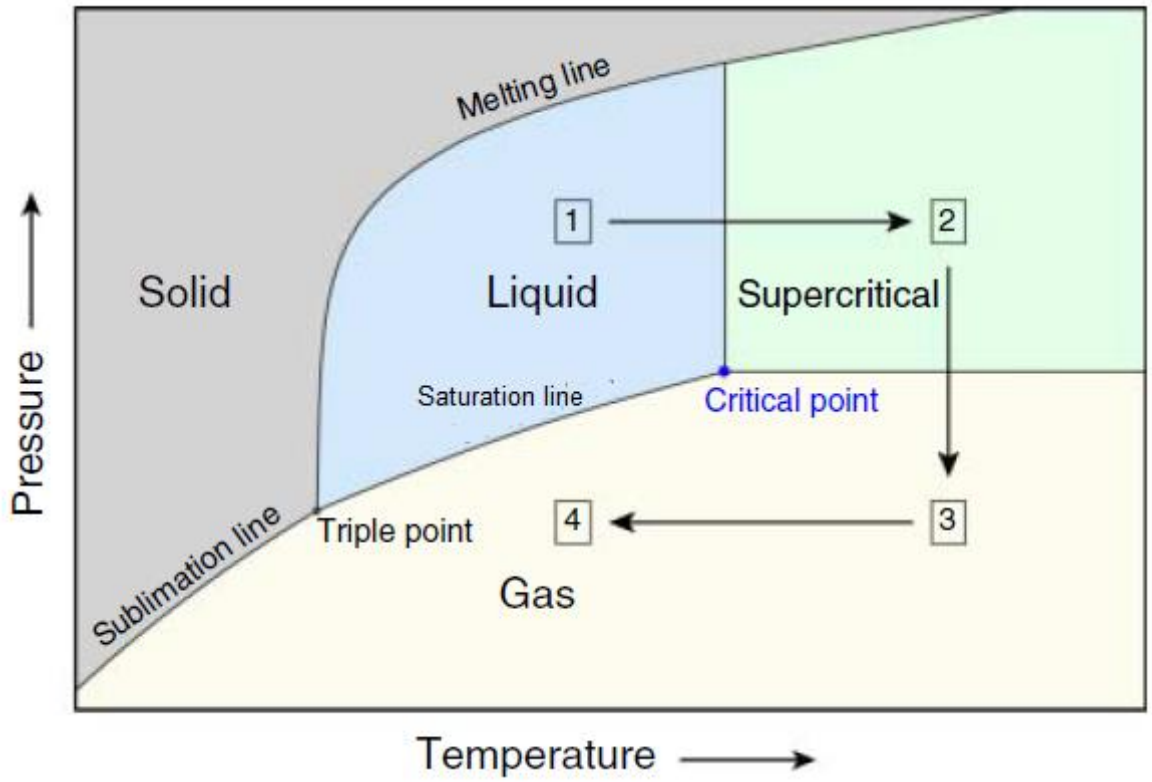

Fig. 1.9: Schematic phase diagram of CO_2 illustrating the path for supercritical activation. By passing through the supercritical state the phase transition between liquid and gaseous phase can be avoided, decreasing the mechanical stress on the framework structure since no surface tension resulting in capillary forces is acting on the framework. This method is especially promising when dealing with mesoporous materials.[12]

1.4 Applications of MOFs

1.4.1 Introduction

One of the greatest advantages of MOFs lies in the easy tunability of their properties. By choosing the right combination of organic ligand and metal nodes, one can synthesize MOFs to exhibit specific pore size and shape, stability under different conditions and peculiar surface functionalisation. Therefore, is not surprising that MOFs represent a versatile class of materials whose utility has been demonstrated in various applications (Fig 1.10) with most of them taking advantage of their high porosities and surface areas. As stated in this chapter at paragraph 1.2, for this work we are particularly interested in the use of MOFs as adsorbent materials for wastewater treatments, but before illustrating the topic in detail in a separated paragraph, we present an overview of the other most important applications.

1.4.2 Gas storage

The potential use of MOFs as gas storage materials is particularly intriguing for the automotive sector. Gases such as methane (CH_4) and hydrogen (H_2) represent valid alternatives to traditional fossil fuels. The major drawback with those combustibles is the need to store them in high-pressure tanks (~250 bar for methane) and, in the case of hydrogen, at low temperatures. It follows that the onboard storage requires compressing and cooling systems, which is costly and potentially unsafe. In recent years, numerous studies have obtained interesting results in the storage of methane and hydrogen with MOFs, showing that the use of those materials could lead to high gas uptake in milder conditions in terms of pressure and temperature compared to traditional methods.[15] For example, IRMOF-6 (Fig. 1.11) has been demonstrated to be able to adsorb 240 cm^3/g methane at 36 atm and room temperature.[19] Regarding H_2 storage, Ni_2(m-dobdc) (a Ni-based MOF with a 1,4-dioxido-1,3-benzenedicarboxylate linker) is a great example of high-performing material with respect to the critical metrics of usable volumetric H_2 capacity at pressures between 5 and 100 bar and near-ambient temperatures.[20]

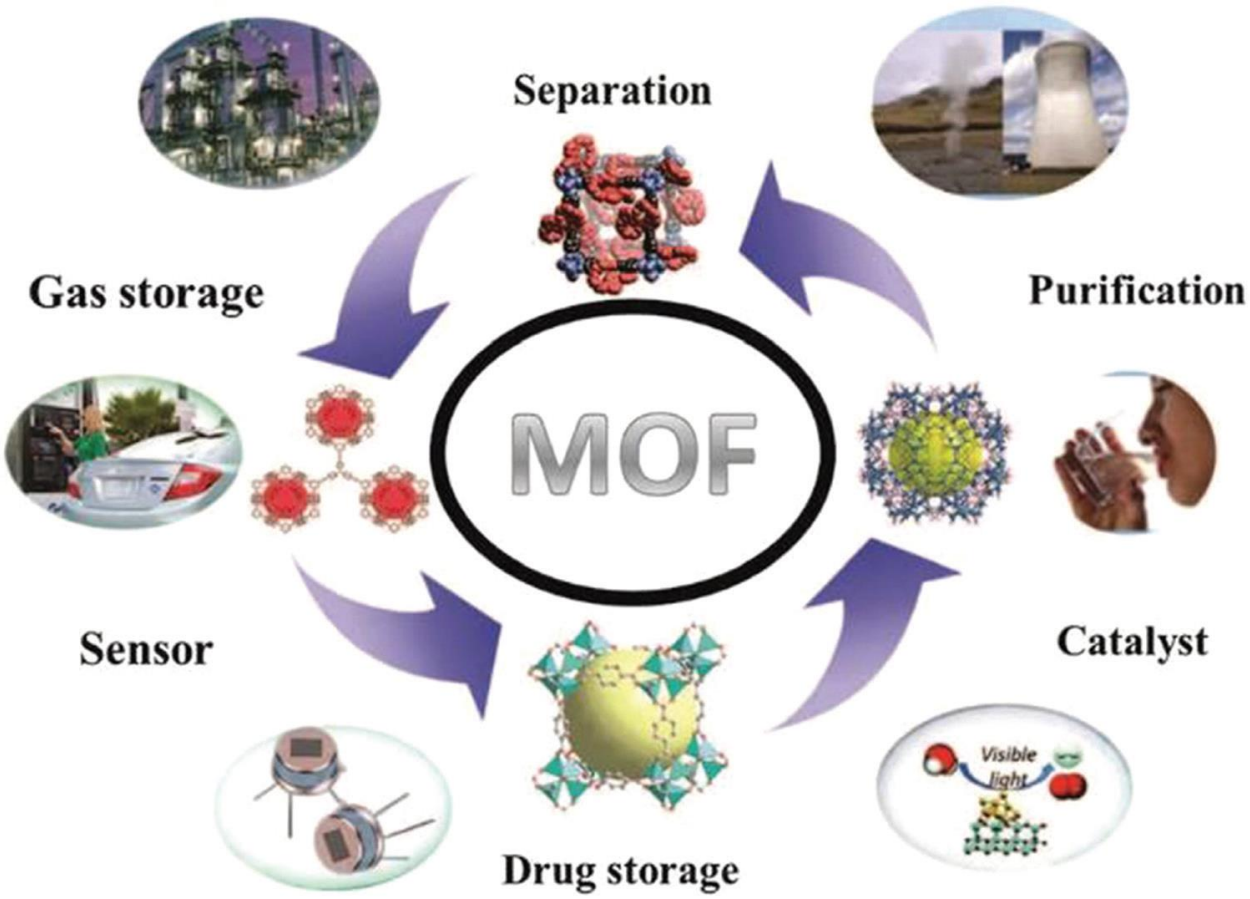

Fig. 1.10: Applications of MOFs.[21]

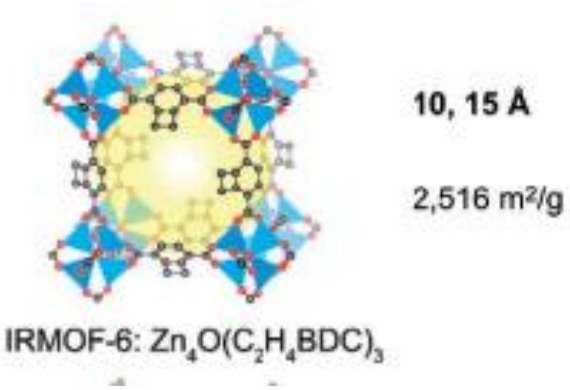

Fig. 1.11: Crystal structure of IRMOF-6, with formula, pore size and surface area.[22]

The high gas-adsorption capacity of MOFs also finds useful applications in the abatement of polluting gaseous emissions (such as CO_2 and NH_3). For example, MOF-177 has been showed to surpass the gravimetric CO_2 capacity of numerous Zeolites and Activated carbons (considered to be benchmark materials) by 1.5 times.[22] To enhance CO_2 uptake in porous MOFs, the incorporation of pendant alkylamine functionalities within the pores has recently been pursued. This latter strategy has been proved an effective way to improve CO_2 adsorption capacity as well as to increase CO_2 binding energy in porous MOFs.[19] Regarding the NH_3 capture, in 2018, Dincâ and colleagues investigated the NH_3 sorption properties of two series of triazolate frameworks, M_2Cl_2BBTA (M= Co, Ni, Cu; BBTA= 1H,5H-benzo(1,2-d),(4,5-d')bistriazole) and M_2Cl_2(BTDD) (M= Mn, Co, Ni, Cu; BTDD= bis(1H-1,2,3-triazolo[4,5-b],[4',5'-i])dibenzo[1,4]dioxin) (Fig. 1.12).[23] These MOFs contain a high density of open metal sites (OMSs), and several of these frameworks exhibited record static and dynamic NH_3 capacities. Under equilibrium conditions at 1 bar, Cu_2Cl_2BBTA adsorbed 19.79 mmol NH_3 per g, more than twice the capacity of activated carbon.[15]

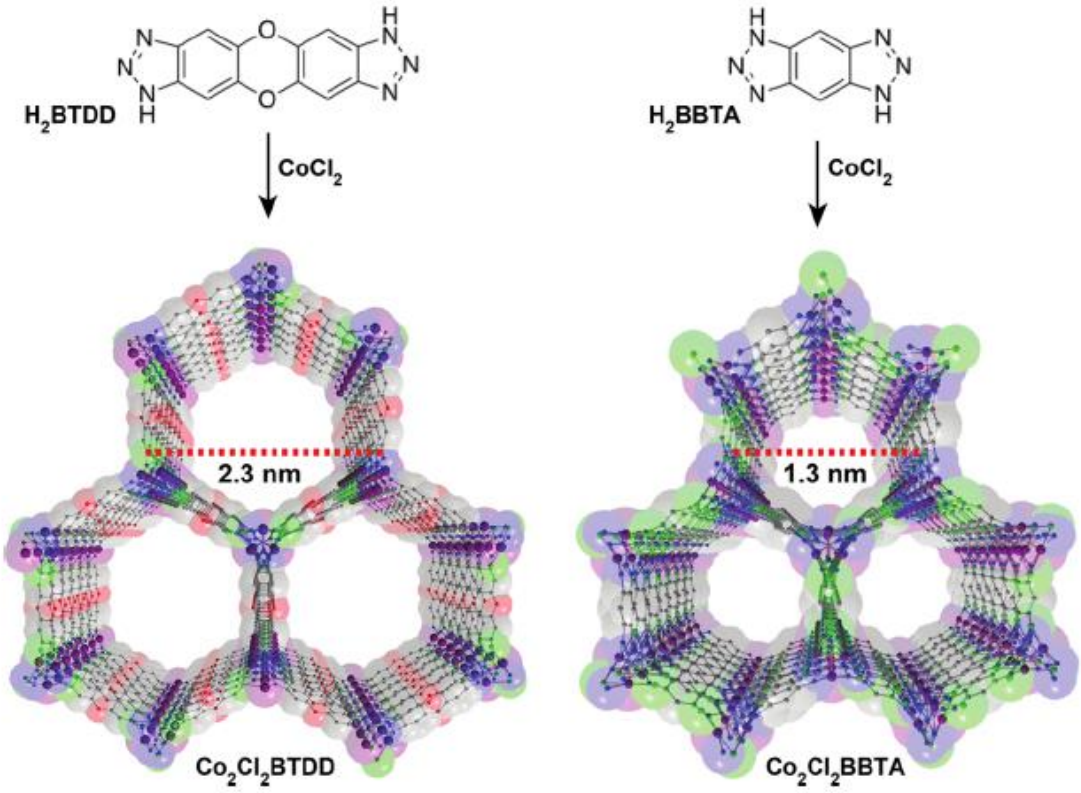

Fig. 1.12: Synthesis and structure of Co2Cl2BTDD (left) and Co2Cl2BBTA (right). C, grey; O, red; N, blue; Cl, green; Co, purple. Hydrogen atoms have been omitted for clarity.[23]

With the functionalisation of the pores surface inside MOFs, it is also possible to obtain adsorbent materials with high selectivity towards specific molecules, in order to perform gas separation via adsorption, for which the energetic demand would be significantly lower compared to traditional gas separation methods such as cryogenic distillation.[24] For example, the MOF $Cu_6(DDCBA)_3$ (also known as ZJU-72), thanks to the combined effect of its open metal sites and the presence of immobilized –COOH groups on the pore surfaces, possesses high selectivity for C_2H_2/CH_4 and CO_2/CH_4 separation.[25]

1.4.3 Catalysis

Chemical industry relies on catalytic processes. Especially for commodities, the synthetic processes involve in most cases heterogeneous catalysts, because they offer many advantages over their homogeneous counterparts such as easier separation of catalysts from reaction products, their applicability to continuous flow processes, and their recyclability. On the other hand, homogeneous catalysts possess different advantages, for examples in terms of selectivity and activity, but most importantly they are chemically better defined, meaning that the structure of the active sites is known and uniform.[26] In most cases, active sites on heterogeneous catalysts

are not uniform, therefore the characterization at a molecular level and a rationalisation in the catalysts design and development are extremely difficult. The use of MOFs as heterogeneous catalysts or supports can help overcome this issue due to their long range ordered structure, that allows a precise characterization and understanding on a molecular level of the active-sites composition. Such property leads to a better comprehension of the structure-activity relationship.[27] The catalytic performances of heterogeneous MOFs often do not exceed those of their homogeneous counterparts, however MOFs do present a few unique features that should be further investigated in their applications in catalysis, and which cannot be achieved by homogeneous catalysts or inorganic solid catalysts.

These characteristics are:[28]

- Size and shape selectivity is possible and has already been demonstrated by MOF catalysts due to restrictions resulting from their pore opening diameters, and therefore limitations regarding the accessibility of the active centres in the MOF structures.
- The great versatility in MOFs preparation is proven by pre- and post-synthetic modification, which can be combined for additional tailoring of the structure. Whereas inorganic solid catalysts possess, most of the time, higher thermal and chemical stability, modification, and post-functionalization of these materials is a complex.
- Chiral MOFs are unmatched by inorganic solid catalysts in promoting asymmetric transformations. The well-defined structure of the MOFs materials can aid in determining mechanisms and asymmetric induction pathways.
- The possibility of creating core–shell structures of the MOF@MOF type or mixed/multivariant-MOFs opens pathways to new architectures allowing new features such as: (i) two different MOFs able to catalyse different multi-step reactions; (ii) the combination of incompatible catalysts in the same solid material; (iii) MOF@MOF materials exhibiting different size and shape selectivity, allowing easy separation of reagents and reaction products without further purification steps.

1.4.4 Commercialisation of MOFs

It is a quite common belief that large-scale production of MOFs would be prohibitively expensive, due to the need of complex materials, peculiar solvents, and reaction conditions. It is also often pointed out that MOFs, being composed in large percentages of organic material, cannot have the necessary stability (thermal, chemical or structural) for any industrial or commercial application.[29] Both affirmations represent although a narrow and incomplete

comprehension of the topic. First, the stability of the MOFs depends on their structure, therefore it can be improved through the choice of the appropriate combination of organic linker and SBUs. Most importantly, the required stability of a MOF depends strictly on the application the material is designed for. For example, the thermal stability required to MOFs used in gas adsorption or gas separation is way lower than the one necessary for the MOFs used in catalysis. Regarding the price issues, while it is true that expensive technologies are employed in the synthesis, the end price is also heavily dependent on many other factors dealing with production scale, market value, and the specific application in question.[29]

To support this last statement, it can be brought up that from 2011 to 2019, the number of annual patents filing related to the field of MOFs has increased from 78 to 665 (more than 9 times), and that around 50% of the patents come from the private sector,[15] demonstrating that the foundations for a future large-scale commercialisation of MOFs are solid and tangible.

Some companies, both small start-ups and larger groups such as BASF, are already producing MOFs in ton scale quantities for various applications, from gas storage to battery materials.[15,29,30]

1.5 MOFs as adsorbent materials for Waste waters treatment

1.5.1 Introduction

The rapid development of industrialisation and the following increase in world population of the last decades, along with obvious advantages, have resulted in some serious environmental threats, one of them being the water contamination. By direct consequence, approximately 30% of world population lacks access to clean water.[31] Water pollution derives from the discharge of hazardous wastewaters into the environment without previous treatments.

It is no surprising that researchers have been studying cheap and efficient methods for wastewaters treatment for a long time. Amongst these, adsorption is one of the most commonly used approach due to simple operation conditions, low energy consumption and no prerequisite to use oxidants/reductants during the treatment process. Adsorption occurs through the uptake of particles, ions, molecules, or atoms (adsorbates) on the surface of the material (adsorbent).[31] In recent years, MOFs are receiving great attention in the studies of adsorbent materials for wastewaters treatment. Among the classes of polluting agents whose removal is being studied with MOFs, the most important are:[32–34]

- Organic dyes: they are produced in large quantities (800000 tons per year) of which around 10-15% directly reaches the environment as effluent or during losses that occur

during drying processes. Many of the released dyes and their breakdown products are toxic, carcinogenic, or mutagenic to life forms. Additionally, many of them remain in the environment for a long period of time. They are often divided in three main categories (Scheme 1.1): cationic dyes (e.g., Methylene Blue [MB]), anionic dyes (e.g., Methyl Orange [MO]) and neutral dyes (e.g., Dimethyl Yellow [DY]). The latter category represents the most difficult to remove via adsorption due to the weaker electrostatic interactions with the surface of the adsorbent.

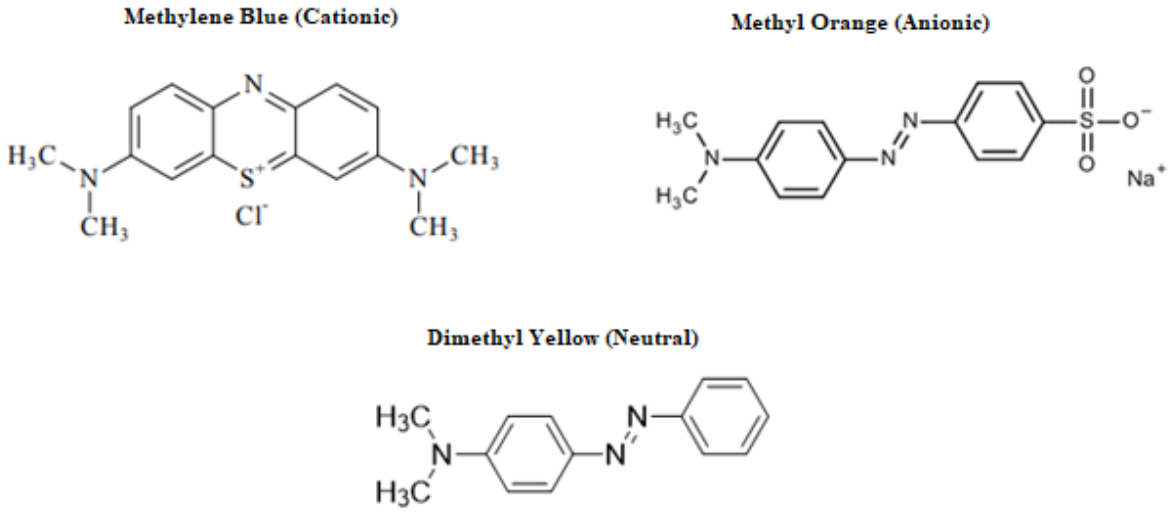

Scheme 1.1: examples of the three main categories of organic dyes.

- Pharmaceuticals and Personal Care Products: this class of pollutants is unique due to their ability to induce physiological effects on humans in low doses. They can be introduced into the environment from various sources, including sewage treatment plants, hospitals, runoff from agriculture and animal farming and aquaculture facilities.
- Herbicides and Pesticides: agricultural activities are responsible for the contamination of more than the 50% of polluted water sources, as consequence of the input of agrochemicals (herbicides and pesticides) in surface and groundwaters. This data is particularly worrying, because most of public environmental protection projects are urban-oriented, while the extra-urban areas where the agricultural activities take place.
- Industrial compounds and by-products: industrial wastewaters contain a large variety of potential pollutants, the composition of which depends a lot on the specific industrial sector they come from (pharmaceutical, polymeric, food…). Such pollutants include, but are not limited to, solvents, heavy metals, plasticizers (phthalates), and food additives (e.g., benzoic acid).

1.5.2 Adsorption Mechanisms over MOFs

Due to the infinite number of possible combinations of organic linkers and Open Metal Sites (OMSs) that can be found inside the structure of MOFs, it is possible to obtain materials with a wide range of superficial functionalities. When MOFs are used as adsorbent materials, these functionalities may have different kind of interactions with the adsorbate molecules, resulting in a variety of possible mechanisms by which the adsorption can take place (Fig. 1.13). The most important mechanisms are briefly illustrated in the following list:[31]

- Electrostatic interactions: they occur between electric charges present on the surface of the MOF and in the adsorbate molecules. Often, the charges on the adsorbent surface are obtained by grafting foreign species on said surface, or by protonation or deprotonation of superficial functionalities led by changes in the pH of the aqueous solution. It is the most important adsorption mechanism for this application.
- Acid-Base interactions: not as common as electrostatic interactions, usually they are obtained by grafting acidic (e.g., $-SO_3H$) or basic groups (e.g., $-NH_2$) over the pore surface.
- Hydrogen bonds: occur between the lone pair of a highly electronegative atom and the hydrogen atom of a N-H, O-H or F-H bond. When they occur between the surface of the MOF and the adsorbate, they can improve the adsorption performance.
- π -π stacking: typical mechanism for the adsorption of organic molecules. If the adsorbate molecule possesses a π electronic system, it can interact with OMSs or other π systems belonging to the MOFs surface (typically to the organic ligands, that often contain aromatic rings), resulting in a strong adsorption.
- Hydrophobic interactions: some MOFs have highly hydrophobic surfaces, due to the presence of functionalities such as benzene rings or perfluorinated groups. Those surfaces can have strong interactions with non-polar pollutants, for example oils and molecules with long carbon chains in general.

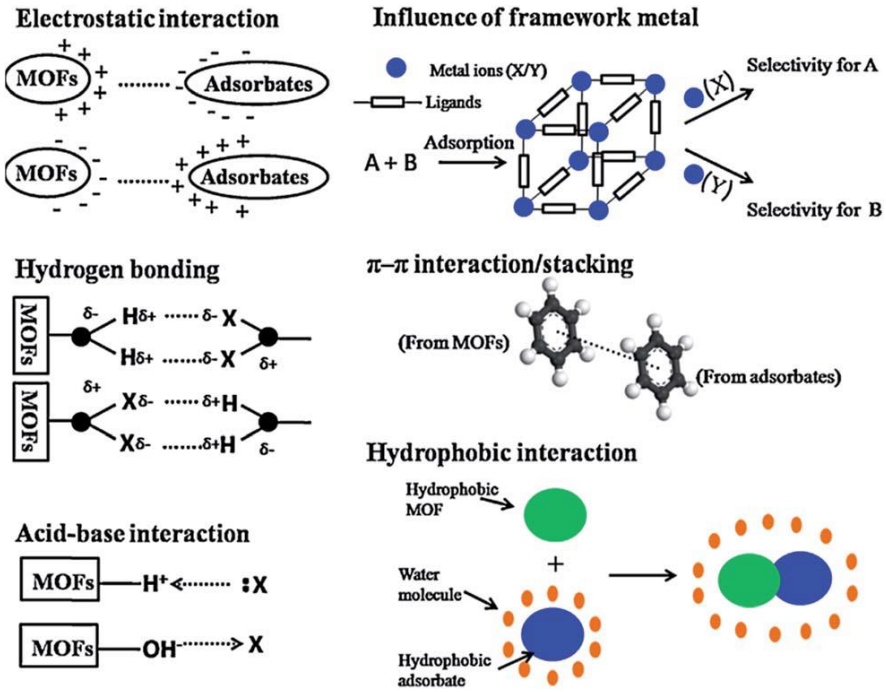

Fig. 1.13: Adsorption mechanisms for organic molecules over MOFs.[33]

1.5.3 Adsorption selectivity over MOFs

The adsorption mechanisms that occur during the processes are obviously not determined by the functionalization of the adsorbent surface alone, but they depend also on the nature of the adsorbate molecules. It follows that, in presence of a mixture of different pollutants, it is possible to tune the properties of the MOF used as the adsorbent in order to selectively remove a single component (or class of components) of the mixture. It is noteworthy that in the synthesis of MOFs, it is possible to tune also the size and shape of the pores, therefore the selectivity can be also influenced by the different dimensions of the adsorbate molecules.[35]

1.5.4 Alternative use of MOFs in Waste waters treatment

Adsorption is not the only technique used in wastewaters treatments. Another possibility is to perform chemical treatments, specifically oxidation reactions, to decompose and remove organic pollutants from the water. Those methods require the use of oxidating agents, such as Chlorine, Chlorine Dioxide, Ozone, which can unfortunately lead to the formation of potentially toxic disinfecting by-products. In recent years, Advanced Oxidation Processes (often abbreviated as AOPs) such as photocatalysis, Fenton reactions, and sulphate radical mediated oxidations using MOFs have attracted attention to treat pollutants due to their simplicity and reproducibility. Highly reactive species (such as hydrogen peroxide [H_2O_2] and sulphate radicals [$SO_4^{\bullet-}$]) are used, in combination with MOFs, to produce radicals ($OH^{\bullet}$ or $SO_4^{\bullet-}$) to

enhance the oxidation of organic pollutants to less toxic products.[32] Additionally, the abundance of OMSs available and the possibility to involve organic ligands with high light-adsorption capacities are drawing a lot of attention towards the potential use of MOFs in photocatalytic removal of organic pollutants (especially dyes).[21]

The catalytic activity of the MOFs can be an intrinsic characteristic of their structure, or can be obtained by post-synthetic modifications, for example the incorporation of homogeneous catalysts. In both cases, MOFs can be used for all the intents and purposes as heterogeneous catalysts, with all the advantages (such as easy separability, regeneration and recycle) that makes them attractive for large-scale operations.

1.5.5 MOFs ad adsorbent materials for Dyes removal

Among all the classes of pollutants whose removal is being studied via adsorption over MOFs, dyes are those which are receiving most attentions. A large number of molecules with diverse shapes, dimensions, and properties belong to this class, so the possibility to easily tune the pore shapes and size and the superficial functionalities of the MOFs represents the main strength of these materials for this specific application. Both the morphology of the pores and the MOF-adsorbate interaction can play a fundamental role in the adsorption performances of MOFs. Obviously, high porosities and surface areas are usually preferred, but there are reported cases where the positive interactions between the adsorbate molecules and the surface of a MOF lead to high adsorption capacities despite the low surface area available. One example is the work of Iman et al.[36] in which a Cu-based and a Co-based MOF, with BET surfaces of 118 and 124 m^2/g respectively, and no evident porosity shown during N_2 adsorption experiments, showed experimental adsorption capacities respectively of 76.35 and 82.15 mg/g for Methylene Blue (MB), and of 46.12 and 48.12 mg/g for Methyl Orange (MO) (superior performances compared to some commercial zeolites)[37].

Another benefit derived by the easy tunability of MOFs is the possibility to obtain adsorbent materials showing high selectivity for a specific dye or class of dyes. For example, Wu et al.[38] synthesized a Cd-based MOF which showed highly selective adsorption capacity towards Methylene Blue (MB) even when mixed with other dyes such as Methyl Orange and Rhodamine B. In this case, the selectivity was attributed to the size matching between the MB molecules and the pores of the MOF.

The adsorption conditions (temperature, pH) also play important roles in the performances and selectivity showed by MOFs. The influence of the temperature is bonded with the adsorption thermality. Physical adsorption is essentially exothermic, so in most cases

the performances increase when the temperature decreases, as exemplified in a paper by Khan et al. where a Cu-based MOF was tested for the adsorption of three different dyes at various temperatures.[39] The influence of pH is more complicated. The variations of pH can lead to the protonation or deprotonation of functional groups, both on the adsorbent surface and the adsorbate molecule, thus altering the superficial net charges and, as direct consequence, the electrostatic interactions.[31] In some cases, variations of pH can also increase the competition for the adsorbent active sites by species such as H^+, with the result of a decreasing in the adsorption performances.[39]

In order to improve the adsorption performances of MOFs, recent studies have been focused their attention on different preparative methods to combine MOFs with other functional materials to create hybrids that exhibit synergistic properties from both materials.[40] Li et al. for example demonstrated that the removal efficiency of MB in high concentrations (36 mg/L) by the Cu-MOF HKUST-1 could be improved from 50% to 80% when the MOF was combined with Graphite Oxide (GO) to yield the hybrid material HKUST-1/GO.[41] This hybrid material showed values of pore volumes and surface area approximately twice as high as the ones of simple HKUST-1, plus the hydrophobicity of GO enhanced the stabilization of the otherwise humidity-sensitive HKUST-1 MOF and the dispersion of the hybrid material in the aqueous system. Similarly, other works showed that analogue enhancements could be obtained by growing MOFs upon different supports such as paper (see Scheme 1.2),[34] fabrics[42] and polymers.[43]

Obviously, to be considered for large-scale applications, an adsorbent material should show the possibility to be regenerated and reused after the first adsorption cycle. Usually the regeneration consists in washing the MOF with solvents such as ethanol, and drying them in oven before reusing them, as shown in the works of Iman et al.[36] and Khan et al.[39] where the considered MOFs maintained their original performances for at least four cycles.

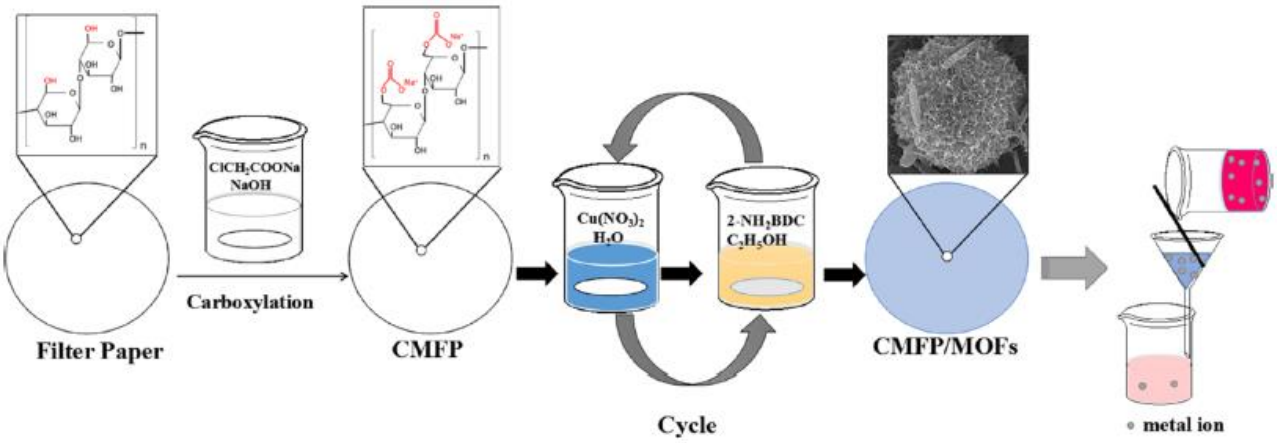

Scheme 1.2: Example of preparation of a MOF supported on CMPF (Carboxymethl-Modified Filter Paper) for the removal of dyes and heavy metal ions.[34]

1.5.6 Adsorption capacity and kinetic studies

To evaluate the dyes adsorption performances of MOFs, it is useful to perform kinetic studies, where the quantity of dye removed by the MOF is measured at different times, and then the data are elaborated to find the best-fitting kinetic model.

The typical experimental procedure for kinetic study consists in immersing a previously weighted quantity of adsorbent material in a sample of aqueous solution with a known concentration of dye and putting the mixture under stirring. At given periods of time, small samples of the mixture are taken out, centrifuged to separate the solid material from the solution, and finally the concentration of the solution is measured via UV-Vis spectroscopy measurements.[36,38,39]

The quantity of dye removed is commonly expressed with the parameter q, also known as adsorption capacity. It is often indicated as q_t when it is calculated at a precise time t, and as q_e when it is calculated at equilibrium.[44] The adsorption capacity at equilibrium q_e is calculated with the following equation:[36]

$$q_e = \frac{(C_0 - C_e)}{m} V \qquad (1)$$

where C_0 and C_e represent the dye concentration measured at t = 0 and at equilibrium respectively, V is the volume of the initial solution and m is the mass of adsorbent material used. Clearly, q_t is calculated with the same formula, using the concentration at t = t C_t instead of C_e.

The variation of q over time can have different trends, depending on the adsorption mechanisms involved. The collected data are usually plotted using different mathematical equations, each one corresponding to a different kinetic model, to see which one better represents the experimental evidence.

Usually, for short contact times the dye removal occurs fast due to the availability of numerous unoccupied active sites on the surface of the MOF, resulting in a rapid growth of q_t values. Commonly, the growth of q_t slows down significantly after a while, due to the increasing saturation of the active sites.[45] Obviously, the starting availability of active sites is related to the load of adsorbent used. The starting adsorption capacity is also connected with the initial concentration of dye in the solution. Increasing the starting dye concentration results in an increasing of the initial value of q_t due to the higher solute concentration gradient,[46] until the point in which the adsorption capacity assumes a stable value, meaning that the adsorbent has reached its saturation point. From this point, any further increase in the starting dye concentration do not modify the adsorption capacity. The minimum starting concentration needed to instantly get to the saturation point is a parameter that can be used to compare different adsorbent materials. With the same starting load, the material which requires a higher starting concentration to get to the saturation point is considered the best adsorbent (more active sites available).[45]

1.5.7 Kinetic models for adsorption

This section contains an overview of the most used kinetic models in the study of dye adsorption over MOFs, with a brief discussion of their assumptions and their mathematical equations.

1.5.7.1 Pseudo Second Order (PSO)

The PSO model corresponds to an adsorption reaction in conditions of non-equilibrium of the kind:

$$A + 2S \rightleftarrows AS_2 \qquad (2)$$

where *A* is the adsorbate molecule and *S* represents an active site.[47,48] This model can be described with the following differential equation:[49]

$$\frac{\mathrm{d}q_t}{\mathrm{d}t} = k_2(q_e - q_t)^2 \qquad (3)$$

where k_2 is the second order rate constant. The differential equation can be integrated, obtaining the following formula:[49]

$$q_t = \frac{k_2 q_e^2 t}{1 + k_2 q_e t} \qquad (4)$$

The integrated formula can be furtherly rearranged to obtain several linear equations, that can be useful to plot the experimental data in order to check the applicability of the PSO model. The most used linear form is the following:[50]

$$\frac{t}{q_t} = \left(\frac{1}{k_2 q_e^2}\right) + \left(\frac{1}{q_e}\right) t \qquad (5)$$

Plotting the experimental data in terms of t/q_t over time, one can see if the linear trend is fitted or not (the parameter R^2 gives a quantitative evaluation of the suitability of the model). The slope and the intersection values of the obtained line allow to calculate q_e and k_2.

The PSO model is quite popular in the adsorption studies of MOFs, because it is often the one who fits the experimental data with higher values of R^2 (see Results and Discussion). Nevertheless, Xiao et al. in a paper published in 2018[47] highlighted the fact that to correctly apply the PSO model, there are some conditions that have to be respected:

- superficial adsorption is the rate-determining step;
- the bulk concentration of dye remains constant (that is where the term "pseudo" comes from);
- no desorption occurs.

If any of those assumptions is not satisfied, the PSO model must be considered incorrect, even in presence of high values of the parameter R^2.

1.5.7.2 Pseudo First Order (PFO)

The other commonly used model to describe the adsorption under non-equilibrium conditions is the PFO model,[49] that can be described by the classic adsorption reaction:[51]

$$A + S \rightleftarrows AS \qquad (6)$$

where *A* is the adsorbate molecule and *S* represents an active site. The assumptions that must be made to correctly apply the model are the same seen for PSO, but the differential equation that describes it is different:[49]

$$\frac{\mathrm{d}q_t}{\mathrm{d}t} = k_1(q_e - q_t) \qquad (7)$$

where k_1 is the first order rate constant. The differential equation can be integrated, obtaining the following formula:

$$q_t = q_e(1 - e^{-k_1 t}) \qquad (8)$$

And subsequentially rearranged in the linear form:

$$\ln(q_e - q_t) = \ln(q_e) - k_1 t \qquad (9)$$

Analogously to the PSO model, one can plot the experimental data in terms of $\ln(q_e\text{-}q_t)$ over time and use the parameter R^2 to evaluate the fitting goodness of the data to the PFO model.

In most cases (see Results and Discussion), the comparison of R^2 values seems to favour the PSO model over the PFO. Some recent studies although have pointed out that some of those results could have been influenced by some methodological biases, and so one must be careful

when using those data. First, one common mistake is the inclusion of data collected after the reaching of equilibrium, or very close to it. Those data, despite yielding satisfying R^2 values, are not significant since they do not give information about the dynamics of the adsorption processes.[51,52] Another issue often pointed out is that the use of linearized equations to compare the two models are actually not very reliable, since they compare different parameters, therefore the use of non-linearized equations is often encouraged.[49,52]

1.5.7.3 Intra-Particle Diffusion (IPD)

When the adsorbate diffusion inside the pores of the adsorbent is the rate-determining step, the equation that better describes this kinetic is the following:[53,54]

$$q_t = k_d t^{1/2} + C \qquad (10)$$

where k_d represents the intraparticle diffusion rate constant and C is the intercept (usually C=0). The linear equation allows to plot the experimental data in terms of q_t over the square root of t, and as always, the parameter R^2 represents a helpful tool to evaluate the fitting of the model. Sometimes, the linear equation obtained interpolating the experimental data has a non-zero intercept: in those cases, it means that the adsorption process may involve more than one mechanism.[45]

The assumption that the adsorbate intraparticle diffusion is the rate determining step is often true for a lot of adsorption processes that take place in batch reactors under rapid stirring.[53] This model has been found useful in the past to describe the adsorption of dyes and metal ions over biosorbents (for example hyacinth roots for the removal of basic dyes such as MB).[55] For the adsorption of dyes with MOFs instead, usually the fitting is not as good as the ones from PSO and PFO (see Results and Discussion).

1.5.7.4 Adsorption Thermodynamics: Langmuir and Freundlich isotherms

As stated in paragraph 1.5.7.2, in conditions close to equilibrium the use of dynamic models such as PSO or PFO is not representative of the real adsorption mechanisms. For those situations, the adsorption can be modelled with many different equations, among which two of the most popular are Langmuir and Freundlich isotherms. Langmuir isotherm assumes that adsorption process is monolayer and occurs on a homogeneous surface with all the adsorption sites possessing identical affinities for the adsorbate.[45,56] On the other hand, Freundlich isotherm assumes multilayer adsorption occurs on the surface of an adsorbent, suggesting non-ideal adsorption on the heterogeneous surface.[57]

Langmuir isotherm is described by the following equation:[45]

$$\frac{C_e}{q_e} = \frac{Ce}{q_m} + \frac{1}{bq_m} \qquad (11)$$

where q_m is the maximum adsorption capacity, and b is a constant value. This represents a linear relationship between C_e/q_e and C_e, and as always, the fitting of the experimental data inside the equation can be evaluated with the parameter R^2.

Freundlich isotherm is described by the following equation:[45]

$$q_e = K_F C_e^{1/n} \qquad (12)$$

where K_F represents the Freundlich constant and $1/n$ is a measure of adsorption intensity or surface heterogeneity.[57] As for the previous models, it is most often used in its linearised form:

$$\ln(q_e) = \frac{1}{n}\ln(C_e) + \ln(K_F) \qquad (13)$$

to study the fitting goodness of the experimental data.

Chapter 2

2 Experimental section

2.1 Materials and instrumentations

All reagents and solvents were used as received, ultrapure water purified with the Milli-Q plus system (Millipore Co, resistivity over 18 MΩ cm) was used in all cases. Reagents were purchased from Sigma-Aldrich (analytical reagent grade). The reactions were monitored by thin-layer chromatography (TLC) on highly purified Silica on TLC-PET foils (with fluorescent indicator 254 nm, Fluka). ESI-MS analyses were performed by direct injection of methanol solutions using a WATERS ZQ 4000 mass spectrometer; working temperature: 80 ÷ 100 °C; working concentrations: ca. 10^{-8} g/L; Cone Voltage: 10 ÷ 30 V; working flow: 10 μL/min. The NMR spectra were recorded at 298 K using a Varian Gemini XL 300 (1H 300.1 MHz, 13C 75.5 MHz) and a Varian MercuryPlus VX 400 (^{1}H, 399.9; ^{13}C, 100.6 MHz); spectra were referenced internally to residual solvent resonances and were recorded at 298 K for characterization purposes; full ^{1}H and ^{13}C NMR assignments were done using standard Varian pulse sequences. Spectra have been edited with the software MestReNova Version: 12.0.1-20212, 2017 Mestrelab Research S.L. Abbreviations: s = singlet, d = doublet, t = triplet, m = multiplet, bs = broad singlet. ATR-FTIR analyses were performed with a Perkin Elmer Spectrum Two spectrophotometer, equipped with a Universal ATR accessory, in the range 4000-600 cm^{-1} with a resolution of 0.5 cm^{-1}. Abbreviations: ν = stretching, δ = bending. Thermogravimetric analyses were carried out using a Perkin Elmer TGA-7. The samples (initial weight ≈10 mg) were heated in air in a platinum crucible at a rate of 10 °C min^{-1} from room temperature to 900 °C. UV-Vis spectra were recorded with a Agilent Cary 3500 multicell spectrophotometer. The atomic adsorption spectroscopy (AAS) measurements were performed with a Thermo Scientific iCE 3300 AA01124707 spectrometer in air-acetylene flame (λ = 242.8 nm; spectral bandwidth = 0.5 nm). XRD was performed by a Philips X'Pert Pro instrument equipped with a fast X'Celerator detector, working at 40 mA and 40 kV and using Cu Kα radiation. Field emission-scanning electron microscopy (FE-SEM) analysis was carried out by means of a Zeiss SUPRA 40VP instrument equipped with an INCAx-act PentaFET Precision spectrometer (Oxford Instruments) for energy dispersive X-ray spectroscopy (EDXS) characterization. The used primary beam acceleration voltages were comprised between 1 kV (for imaging) and 20 kV (for EDXS analyses). X-ray photoelectron (XPS) studies were carried out by means of a Specs EnviroESCA instrument using a monochromated AlKα excitation source ($h\upsilon$ = 1486.6 eV), at

an operating pressure of *ca*. 10^{-6} mbar. Survey scans were performed with 100 eV pass energy, every 1.0 eV·step^{-1}, and for 0.1 sec·step^{-1}. High resolution spectra were acquired with 50 eV pass energy, every 0.1 eV·step^{-1}, and for 0.1 s·step^{-1}. In agreement with the literature,[66] binding energy values (BEs; uncertainty = ± 0.2 eV) were corrected for charging assigning to the adventitious C 1s peak, attributed to adventitious hydrocarbons, the value of 284.8 eV. XPS curves were analyzed using the Specs Keystone software, applying a Shirley-type background substraction.[67] The sensitivity factors of integrated peak areas used for atomic percentages (at. %) quantification were supplied by Specs.

2.2 Ligand synthesis

2.2.1 First approach

2.2.1.1 Synthesis of prop-2-yn-1-yl (2-bromoethyl)carbamate (3)

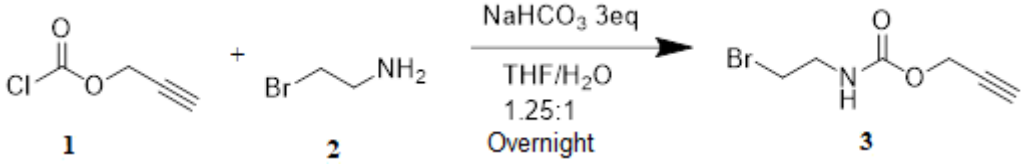

Scheme 2.1: synthesis of **(3)**

A solution of 2-bromoethylamine hydrobromide (**2**, 9.138 g, 44.6 mmol) and $NaHCO_3$ (11.239 g, 133.8 mmol, 3 eq) was prepared in THF/H_2O (107 mL/85 mL) and cooled to 0 °C. Propargyl chloroformate (**1**, 6.075 g, 5 mL, 1.15 eq) was added dropwise. The mixture is kept in the ice-bath under magnetic stirring overnight. THF was then evaporated. The aqueous phase was extracted with ethyl acetate (3 x 20 mL). The organic layer is then washed with HCl 1 M (2 x 10 mL) and Brine (2 x 10 mL) and dried with Mg_2SO_4. The solution was filtered and concentrated under vacuum (first at the rotary evaporator and then for 3 hours at the mechanical pump) under magnetic stirring to favour the evaporation of residual ethyl-acetate. The final product is a colourless oil (6.608 g, 32.2 mmol, 72% yield), that has been used without further purification and stored under Nitrogen at 4 °C.

Rf (in Petroleum Ether/ Ethyl Ether 1:2): 0.48.

ESI-MS(+): (MeOH, m/z): 228 (100) $[C_6H_8NO_2Br + Na]^+$

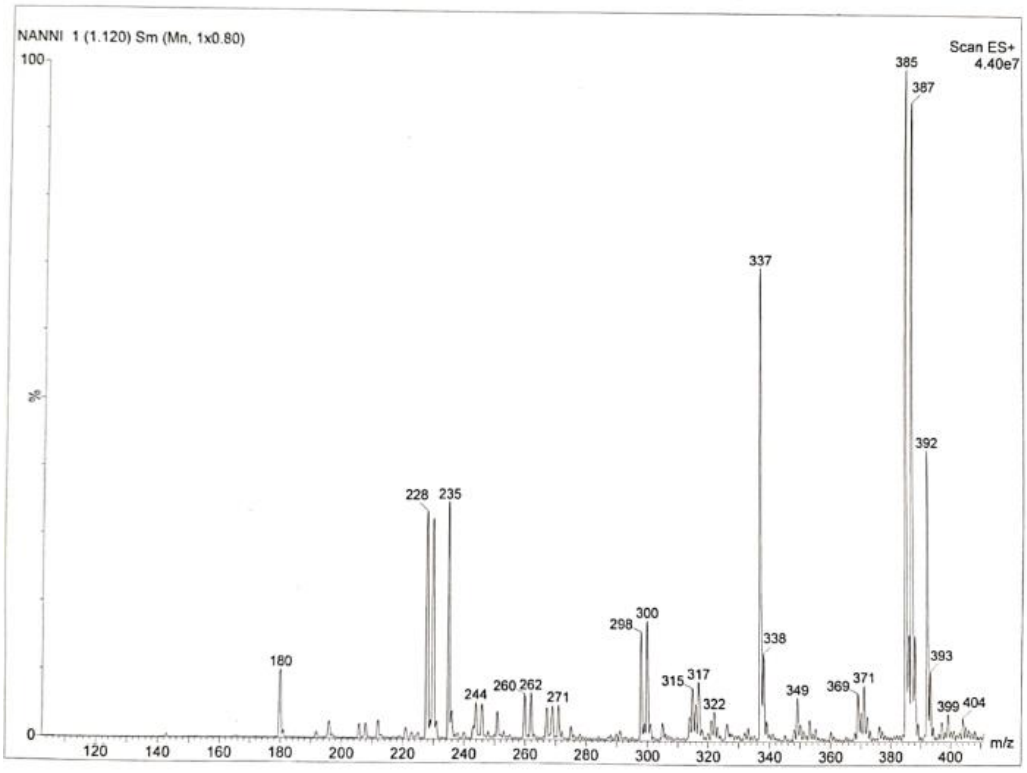

Fig. 2.1: ESI-MS(+) spectrum of **3**. Notice the presence of an unknown co-product at 385, with the typical Br pattern.

^{1}H-NMR (300 MHz, $CDCl_3$): δ 5.24 (bs, N*H*^{3}), 4.69 (d, ^{4}J=2.4, 2H, O-CH_2^4), 3.60 (m, 2H, NH-CH_2^2), 3.46 (t, ^{3}J=5.7, 2H, Br-CH_2^1), 2.48 (t, ^{4}J= 2.4, 1H, C≡C*H*^{5})

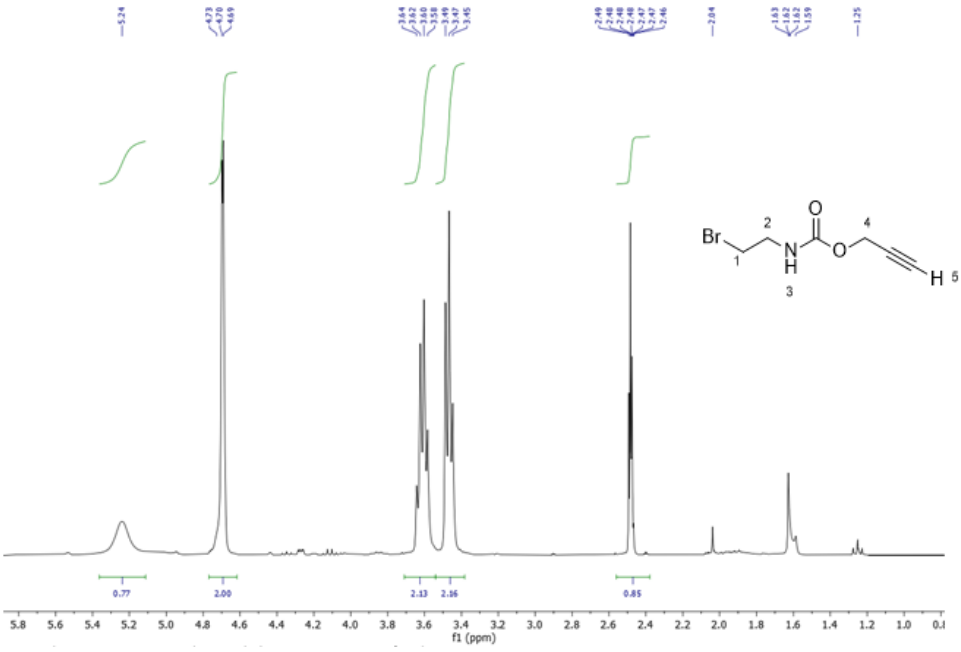

Fig. 2.2: ^{1}H-NMR spectrum of **3**.

^{13}C-NMR (75 MHz, $CDCl_3$): δ 155.22 (Cq, C^3=O), 77.94 (Cq, C^5≡CH), 74.80 (C≡C^6H), 52.70 (-C^4H_2C≡CH), 42.77 (-C^2H_2NH-), 32.20 (-C^1H_2Br) ppm

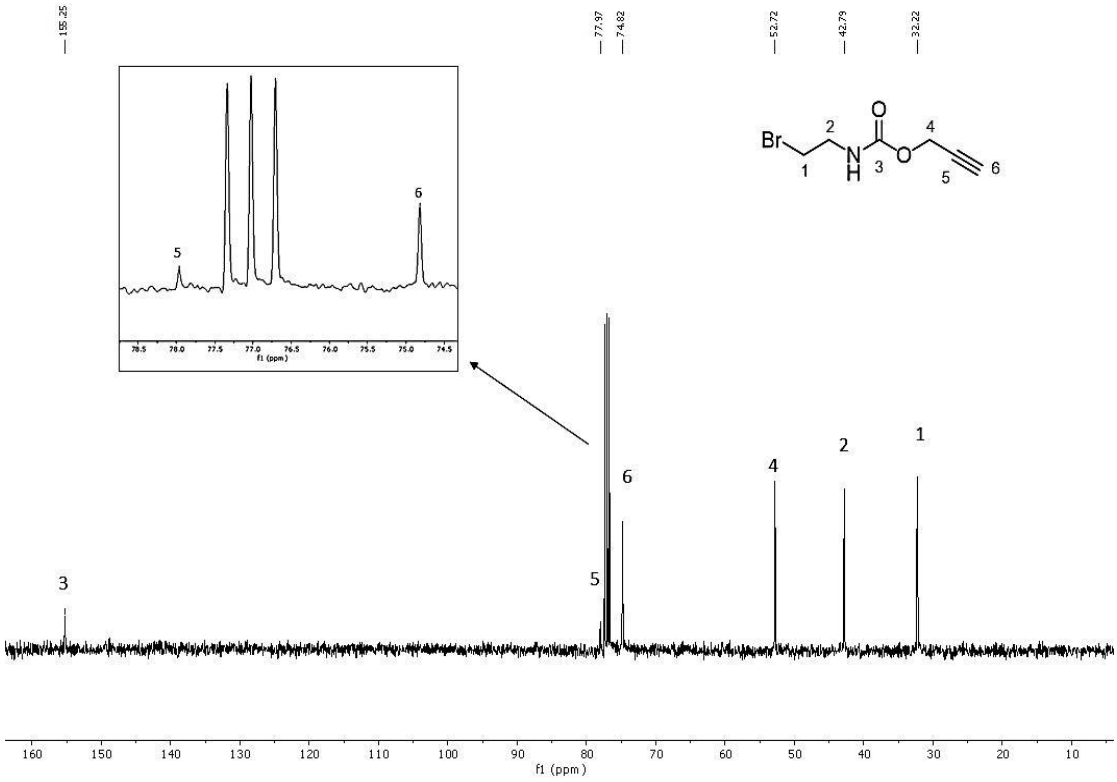

Fig. 2.3: ^{13}C-NMR spectrum of **3**.

2.2.1.2 Synthesis of prop-2-yn-1-yl (2-(3,5-dibromophenoxy)ethyl)carbamate (5)

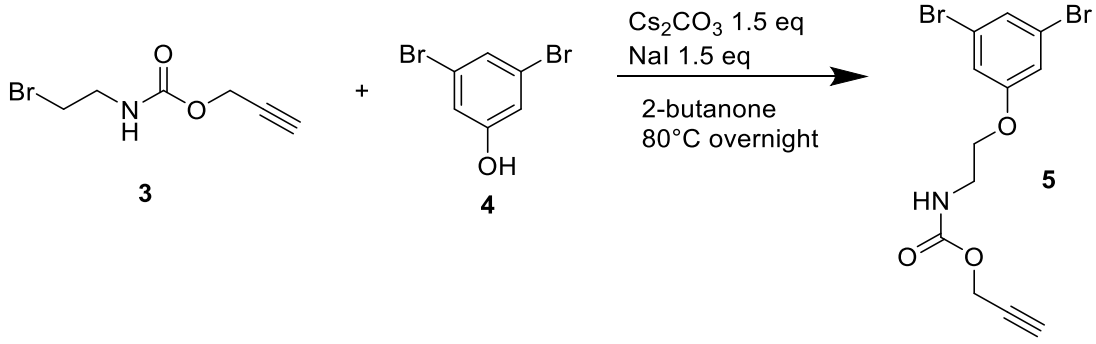

Scheme 2.2: Synthesis of **5**.

A solution of crude **3** (1 g, 2.63 mmol due to the presence of ethyl acetate) and 3,5-dibromophenol (**4**, 1.911 g, 7.59 mmol, 2.88 eq) was prepared in 2-butanone (90 mL). Cs_2CO_3 (2.472 g, 7.59 mmol, 2.88 eq) and NaI (1.137 g, 7.59 mmol, 2.88 eq) were added. The rection is kept overnight at reflux temperature (80 °C) under magnetic stirring. The solution is then cooled at room temperature and concentrated under vacuum. The solid residual is dissolved in CH_2Cl_2 (20 mL) and NaOH 10% w/w (20 mL) and stirred for ten minutes. The organic layer and the aqueous layer are divided with a separating funnel. The aqueous phase is washed with

CH_2Cl_2 (3 x 10 mL), and the washings are added to the organic phase. The organic phase is washed with NaOH 10% w/w (3 x 10 mL), dried with Mg_2SO_4, filtered, and concentrated under vacuum. The final product is a yellow solid (1.043 g, 2.27 mmol, 86% yield). Rf (in Petroleum Ether/ Ethyl Ether 1:2): 0.35.

^{1}H-NMR (300 MHz; DMSO): δ =7.55 (t, ^{3}J=5.4, N*H*^{5}); 7.36 (t, ^{4}J=1.64, 1H, Ar-*H*^{1}); 7.20 (d, ^{4}J=1.64, 2H, Ar-*H*^{2}); 4.63 (d, ^{4}J=2.4, 2H, O-C*H*$_2^{6}$); 4.04 (t; ^{3}J=5.2, 2H, O-C*H*$_2^{3}$); 3.47 (t, ^{4}J=2.4, 1H, C≡C*H*^{7}), 3.34 (d, ^{3}J=5.7, 2H; NH-C*H*$_2^{4}$, partially covered by the water peak).

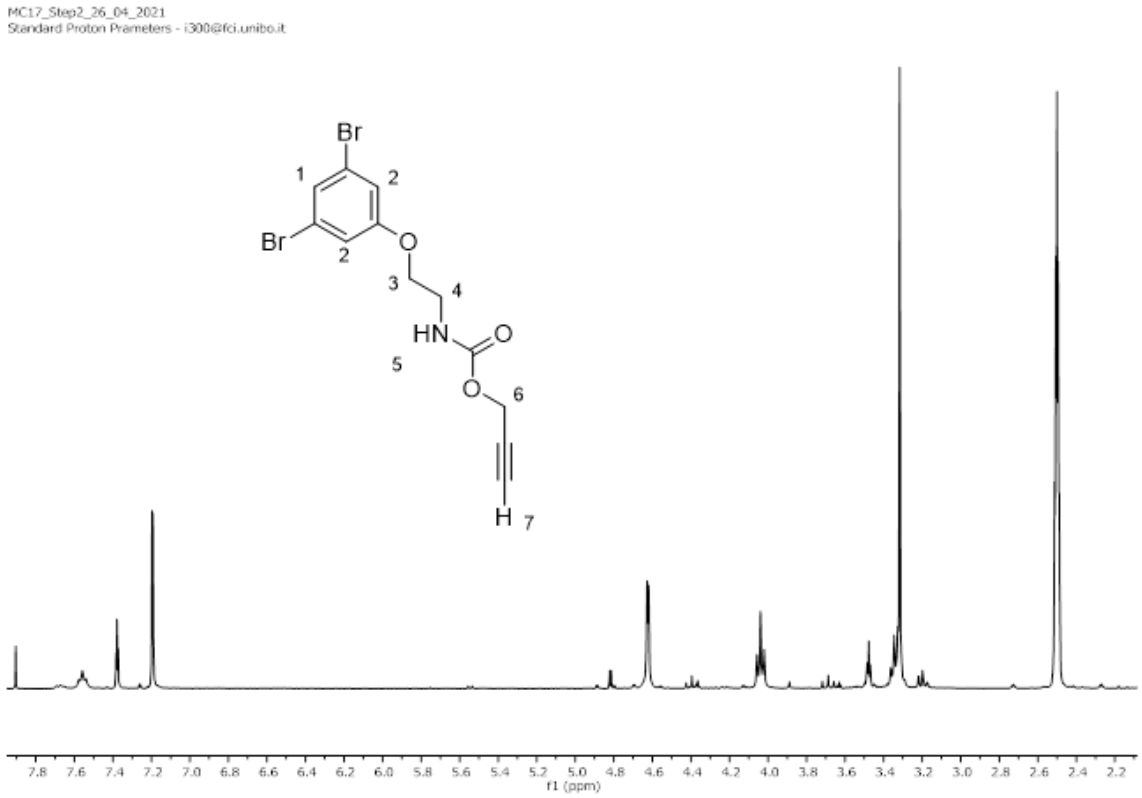

Fig. 2.4: ^{1}H-NMR spectrum of **5**.

^{13}C-NMR (75 MHz; DMSO): δ = 159.95 (Cq, Ar-*C*^{4}-OH), 155.46 (Cq, *C*^{7}=O); 132.91 (Ar-*C*^{1}-H);

125.79 (Ar-*C*^{2}-Br); 122.82 (Ar-*C*^{3}-H); 117.17 (NH-*C*^{6}H$_2$); 79.31 (Cq, *C*^{9}≡CH); 77.14 (C≡*C*^{10}H); 67.11 (O-*C*^{5}H$_2$); 51.63 (O-*C*^{8}H$_2$).

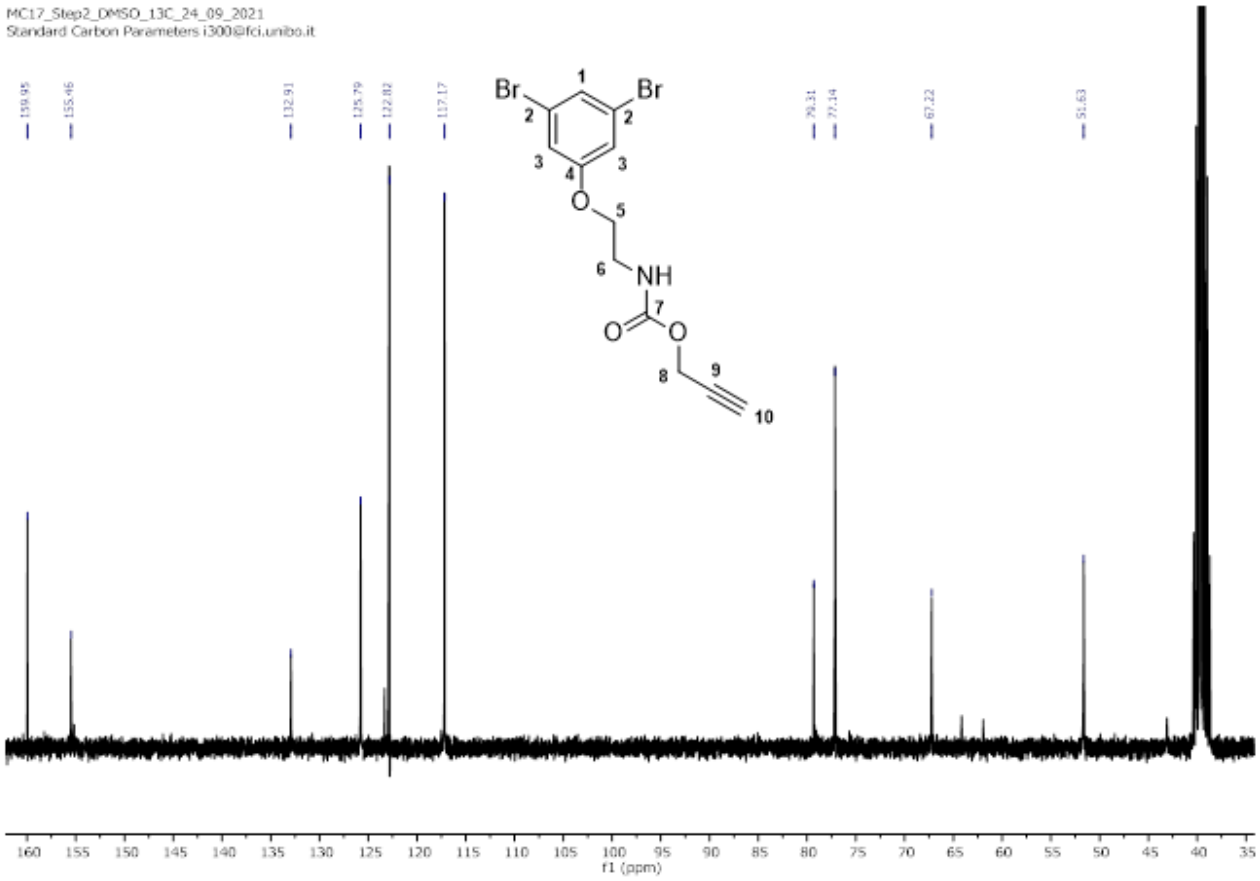

Fig. 2.5: ^{13}C-NMR spectrum of **5**.

ATR-FTIR spectra of neat 5 (cm^{-1}): 3331 (ν NH, m), 3293 (ν ≡C-H, m), 2949 (ν C-H aliphatic, w), 2131 (ν -C≡C-, w), 1703 (ν -C(O)NH- carbamate, s), 1520 (δ NH, s), 1245 (ν C-O, s).

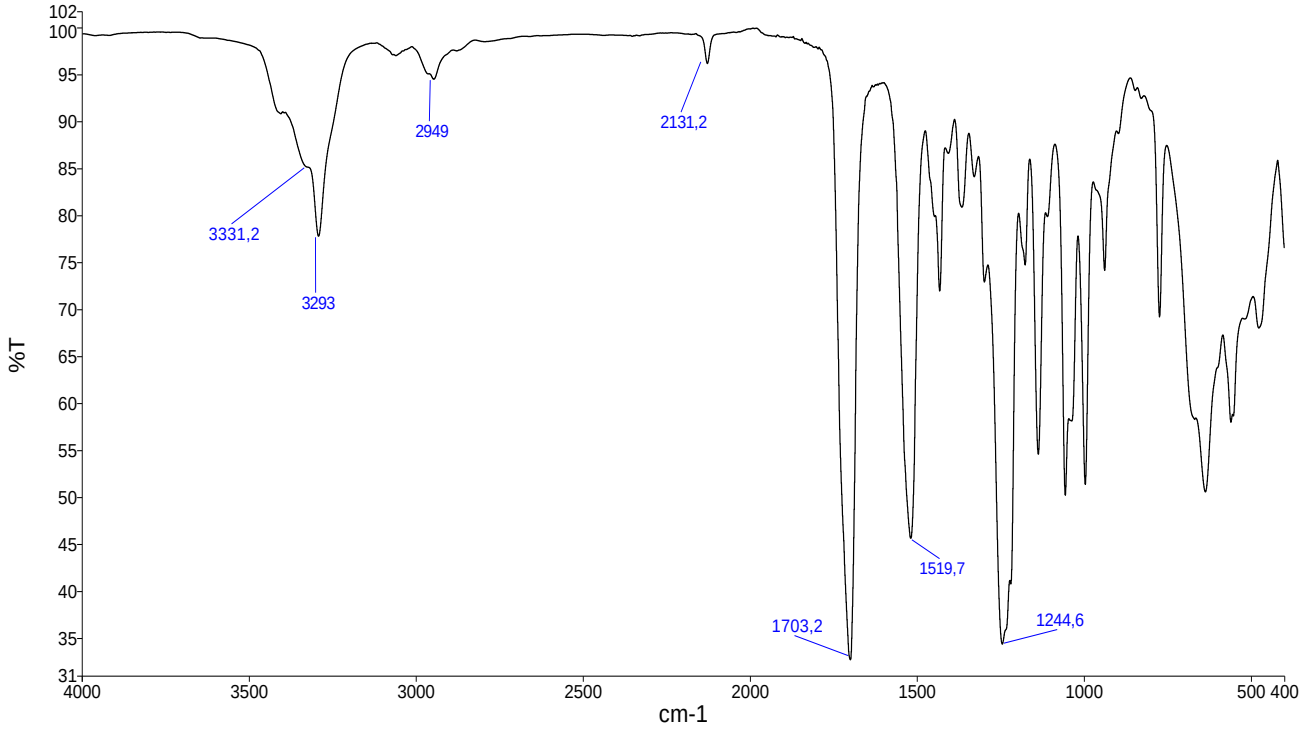

Fig. 2.6: IR-ATR spectrum of **5**.

2.2.1.3 Attempted synthesis of 5'-(2-(((prop-2-yn-1-yloxy)carbonyl)amino)ethoxy)-[1,1':3',1''-terphenyl]-4,4''-dicarboxylic acid (H_2YL80) (first approach)

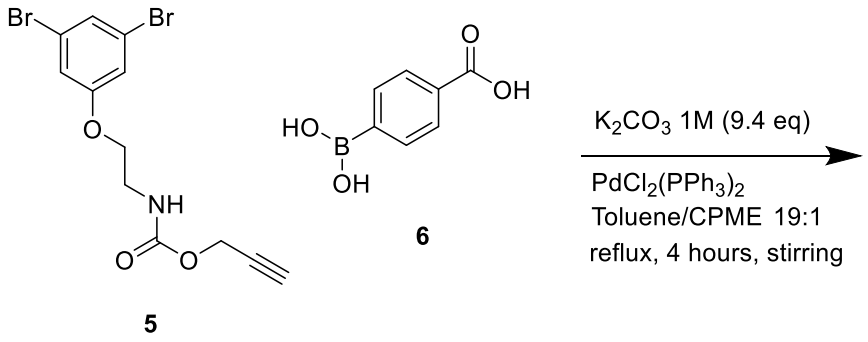

Scheme 2.3: Attempted synthesis of 5'-(2-(((prop-2-yn-1-yloxy)carbonyl)amino)ethoxy)-[1,1':3',1"-terphenyl]-4,4"-dicarboxylic acid [first approach].

In a two-necked round flask, crude **5** (0.2 g, 0.53 mmol) and 4-boronobenzoic acid (**6**, 0.29 g, 1.75 mmol, 3.3 eq) are dissolved in a mixture of toluene/Cyclopenthyl Methyl Ether (CPME) 19:1 (10 mL). A solution of K_2CO_3 1 M (5 mL, 5 mmol, 9.4 eq) is added, then the flask undergoes 3 vacuum/nitrogen cycles. While fluxing nitrogen, a spatula of the catalyst $PdCl_2(PPh_3)_2$ is added. The system is stirred at reflux temperature (110 °C) for 4 hours, keeping the flask wrapped in tin foil. The solution is then filtered on celite and washed with toluene (10 mL) and water (10 ml). The solution is extracted with a mixture of Ethyl Acetate/Hexane 1:1

(2 x 20 mL). The aqueous and the organic phases are separated. The aqueous layer is diluted with water (15 mL) and then 10 mL of HCl 1 M are added. The formation of a white precipitate is observed. The solid is filtered and dried in the oven. The organic layer is dried with Mg_2SO_4, filtered, and concentrated under vacuum. The ^{1}H-NMR analysis showed that the products found in the organic phase and in the aqueous phase are respectively the unreacted reagents **5** and **6** (Fig. 2.5 and 2.6).

^{1}H-NMR organic phase (400 MHz, DMSO) : δ =7.55 (t, ^{3}J=5.4, N*H*^{5}); 7.36 (t, ^{4}J=1.64, 1H, Ar-*H*^{1}); 7.20 (d, ^{4}J=1.64, 2H, Ar-*H*^{2}); 4.89 (d, ^{4}J=2.4, 2H, O-CH_2^{6}); 4.04 (t; ^{3}J=5.2, 2H, O-CH_2^{3}); 3.47 (t, ^{4}J=2.4, 1H, C≡C*H*^{7} partially covered by the water peak).

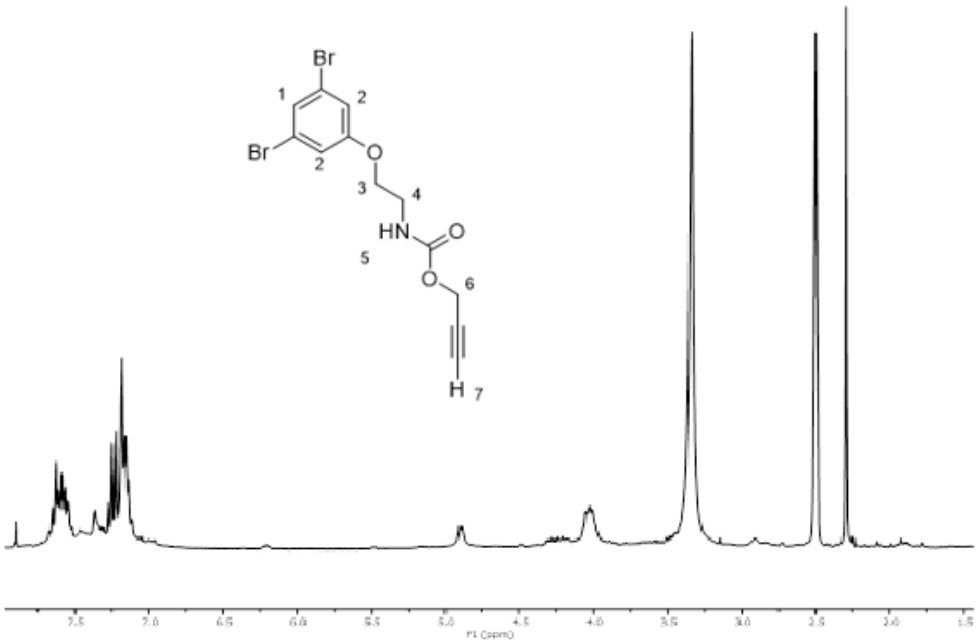

Fig. 2.7: ^{1}H-NMR spectrum of the organic phase, showing the presence of reagent **5** with some impurities.

^{1}H-NMR aqueous phase (400 MHz, DMSO) : δ = 8.24 (s, 1H, O*H*^{3}), 7.87 (s, 2H, Ar-*H*^{1}), 7.87 (s, 2H, Ar-*H*^{2}) (the aromatic protons 1 and 2 are different but their signals fall at the same chemical shift).

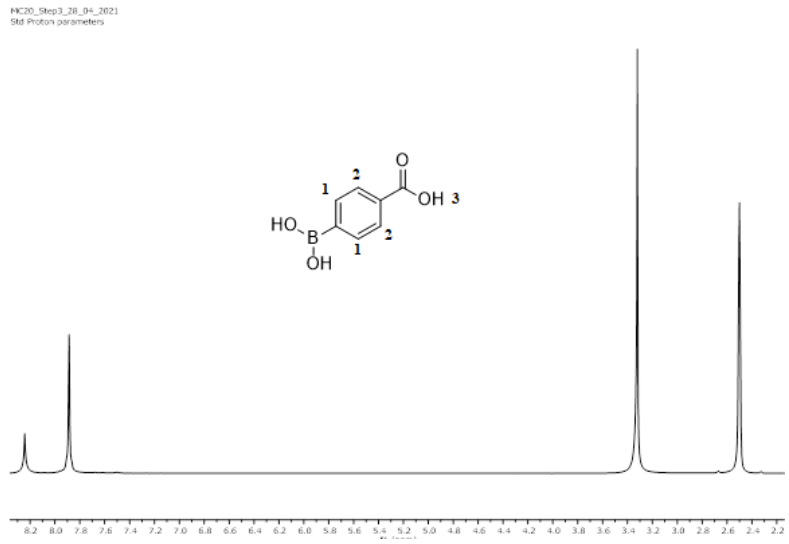

Fig. 2.8: ^{1}H-NMR spectrum of the product found in the organic phase, showing the presence of reagent **6**.

2.2.2 Second approach

2.2.2.1 Synthesis of 3,5-Bis(4-carboxyphenyl)-1-hydroxybenzene (7)

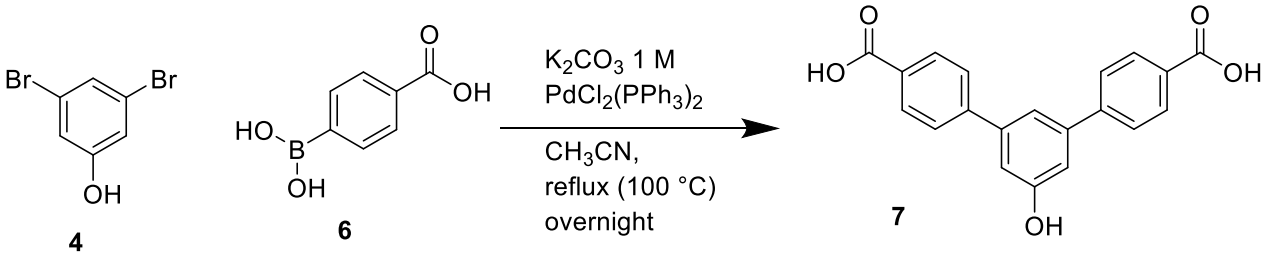

Scheme 2.4: synthesis of **(8)**.

In a two-necked round flask, a solution of **4** (1.8 g, 7.15 mmol) and **6** (2.373 g, 14.3 mmol, 2 eq) is prepared in CH_3CN (60 mL). A solution of K_2CO_3 1 M (57.2 mL, 52.7 mmol, 7.4 eq) is added, and the system undergoes 3 vacuum/nitrogen cycles. The catalyst $PdCl_2(PPh_3)_2$ (0.1 g, 0.143 mmol, 2% catalytic load) is added while fluxing nitrogen, then the flask is wrapped in tin foil, and the system is put at reflux temperature (100 °C) under magnetic stirring overnight. Then the solution is cooled down to room temperature, filtered on celite, washed with DI water (3 x 10 mL) and extracted with a mixture of Ethyl acetate/hexane 1:1 (3 x 50 mL). The organic layer is treated with HCl 2 M (55 mL), and the formation of a dark precipitate is observed. The solution is filtered and the solid is dried in the oven overnight. The final product **7** weights 2.213 g (6.62 mmol, 92.6% yield).

ESI-MS(-) (MeOH, m/z): 333(100) $[C_{20}H_{13}O_5]^-$.

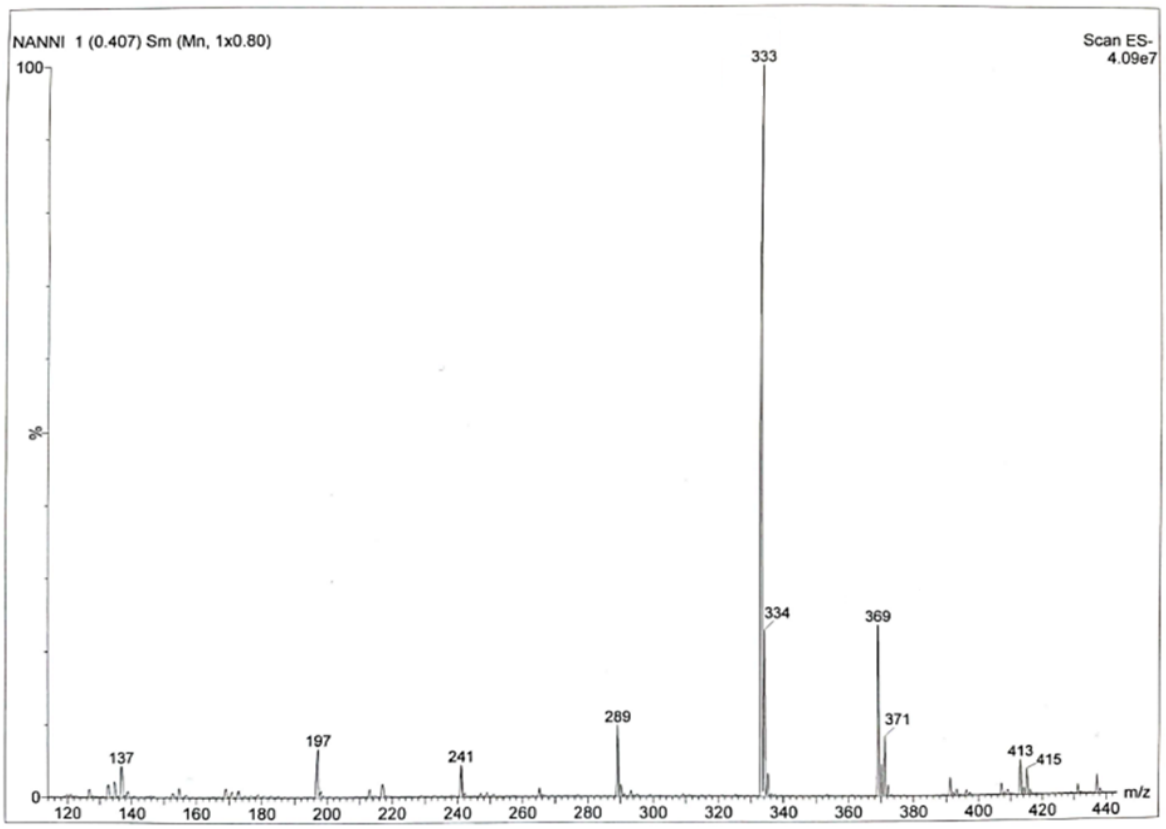

Fig. 2.9: ESI-MS(-) spectrum of **7**.

^{1}H-NMR (300 MHz, DMSO): δ= 12.97 (s, 2H) 9.91 (s, 1H), 8.03 (d, 4H, ^{3}J= 8.41 Hz), 7.85 (d, 4H, ^{3}J= 8.41 Hz), 7.46 (t, 1H, ^{4}J= 1.88 Hz), 7.15 (d, 2H, ^{4}J=1.88 Hz).

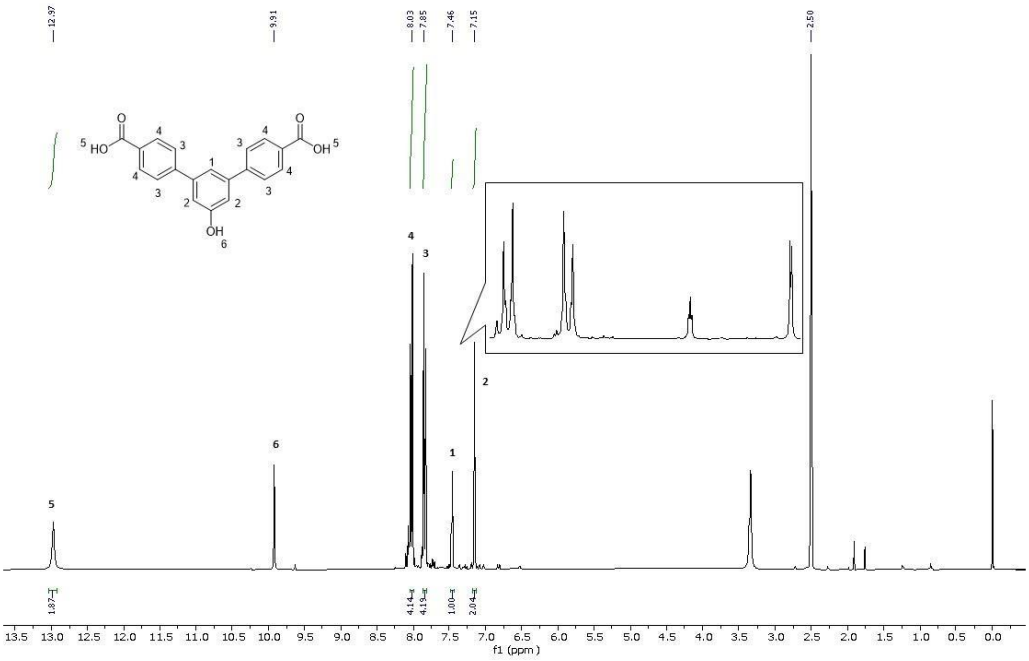

Fig. 2.10: ^{1}H-NMR spectrum of **7**.

^{13}C-NMR (100.6 MHz, DMSO): 167.13 (Cq; *C*^{9}(O)OH); 158.56 (Cq; Ar-*C*^{4}-OH); 144.26 (Cq; Ar-*C*^{5}-Ar); 141.19 (Cq; Ar-*C*^{2}-Ar); 129.93 (Cq; Ar-*C*^{8}-C(O)OH); 129.82 (Ar-*C*^{6}H);127.00 (Ar-*C*^{7}H);116.64 (Ar-*C*^{1}H); 113.15 (Ar-*C*^{3}H).

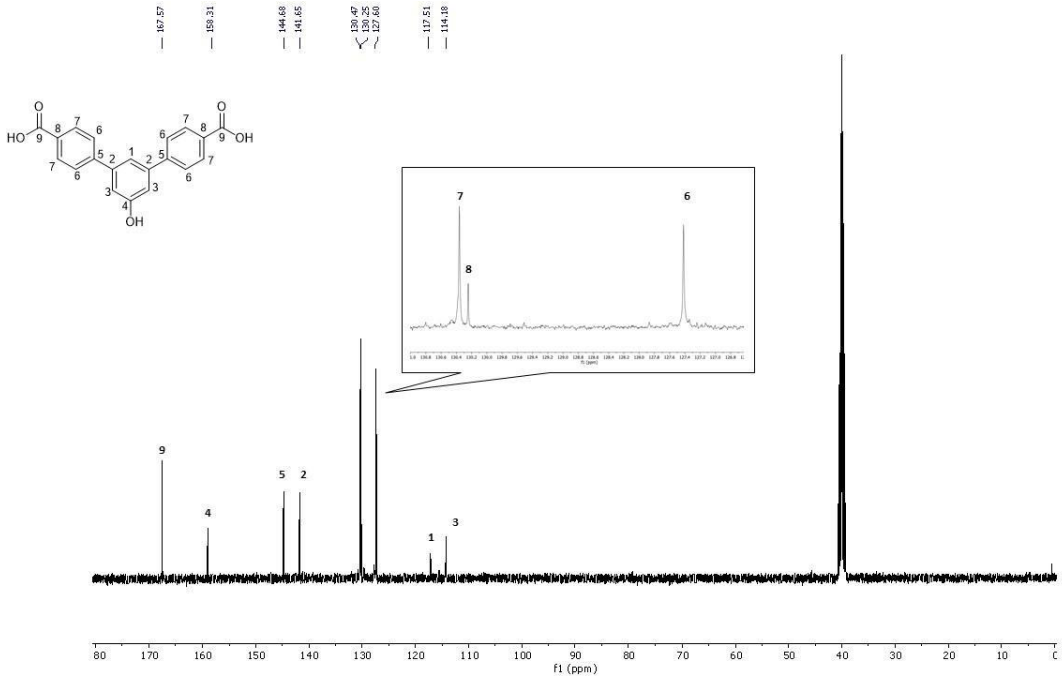

Fig. 2.11: ^{13}C-NMR spectrum of **7**.

ATR-FTIR spectra of neat 7 (cm^{-1}): 3398 (ν O-H alcol, m), 3196 (ν O-H acid, m), 2984 (ν C-H aliphatic, w), 1676 (ν C(O)OH, s), 1285 (ν C-O acid, s), 1181 (ν C-O alcol, s), 839 (δ C-H aromatic), 767 (δ C-H aromatic).

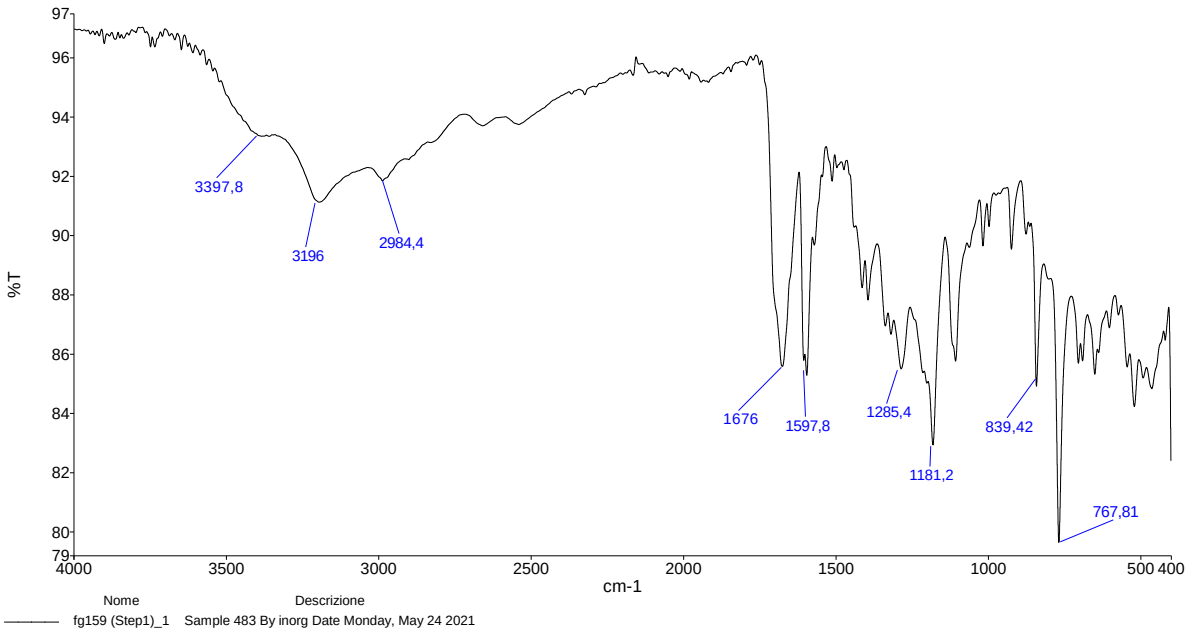

Fig. 2.12: IR-ATR spectrum of **7**.

2.2.2.2 Synthesis of dimethyl 5'-hydroxy-[1,1':3',1''-terphenyl]-4,4''-dicarboxylate (8)

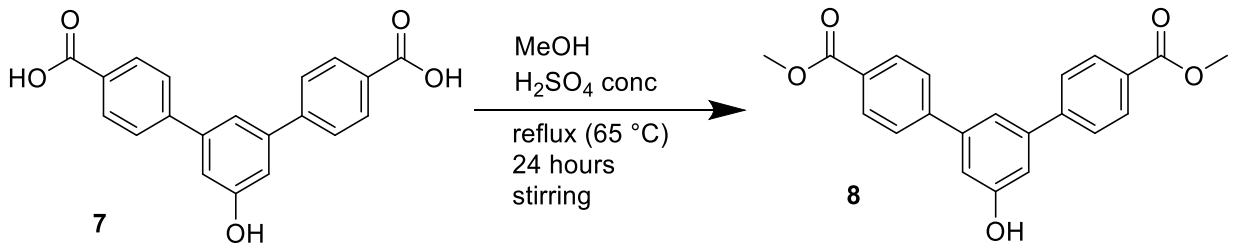

Scheme 2.5: synthesis of **8**.

A solution of **7** (0.779 g, 2.33 mmol) in methanol (80 mL) is prepared. Concentrated H_2SO_4 (1.30 mL, 23.6 mmol, ~10 eq) is added while keeping the solution stirred. The system is stirred for 24 hours at reflux temperature (65 °C). The solution is then cooled down to 0 °C, and 200 mL of DI water are slowly added. The formation of a pink-orange precipitate is observed. The solution is filtered and the solid is dried in the oven overnight. The final product is a pink solid (0.668 g, 2.06 mmol, 88% yield).

Rf (in Petroleum Ether/ Ethyl Ether 1:2): 0.32.

ESI-MS(-) (MeOH, m/z): 361(100) $[C_{22}H_{17}O_5]^-$.

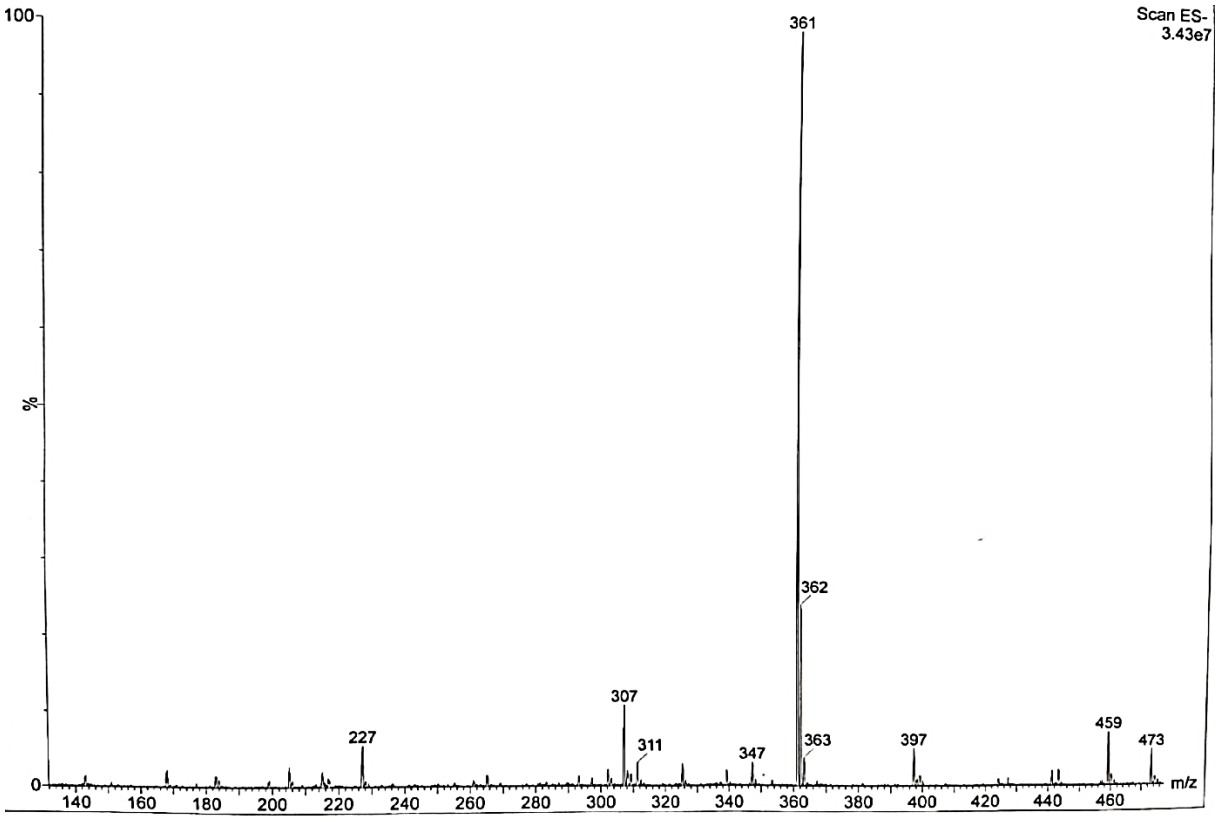

Fig. 2.13: ESI-MS(-) spectrum of **8**.

^{1}H-NMR (300 MHz, DMSO): δ= 9.92 (s, 1 H, -O*H*^{6}); 8.03 (d, ^{3}J=9.00, 4H; Ar-*H*^{2}); 7.89 (d, ^{3}J=9.00, 4H; Ar-*H*^{3}); 7.48 (t, ^{4}J=1.50, 1H; Ar-*H*^{4}); 7.16 (d; ^{4}J=1.50, 2H; Ar-*H*^{5}); 3.88 (s; 6H; O-C*H*$_{3}$^{1}).

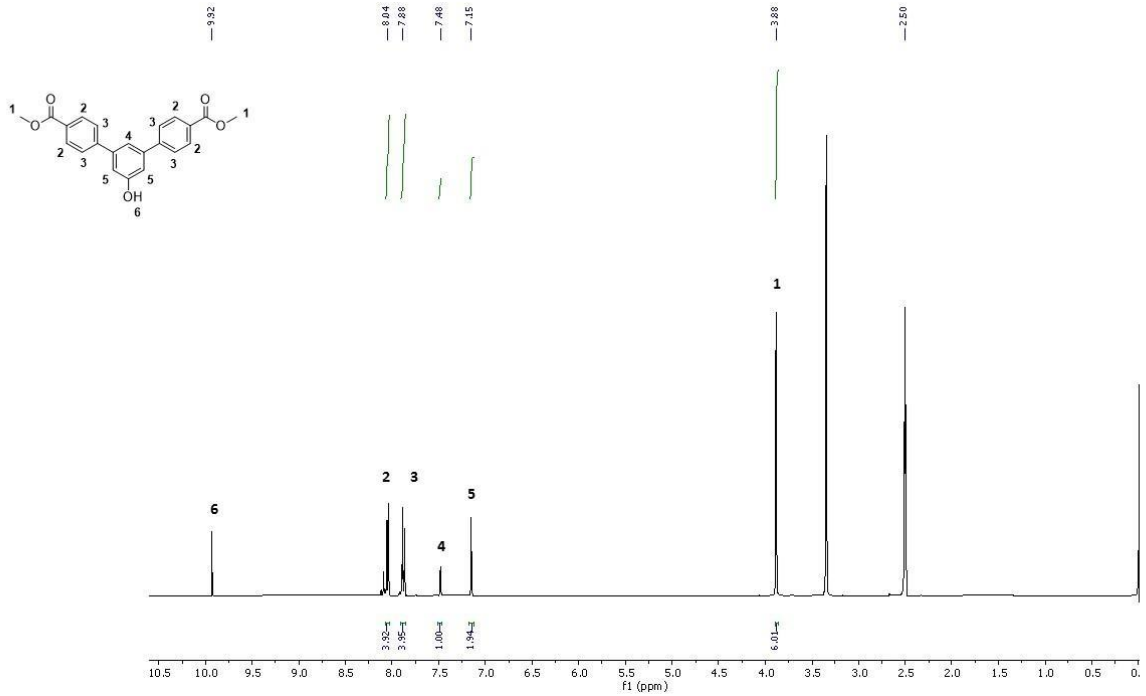

Fig. 2.14: ^{1}H-NMR spectrum of **8**.

^{13}C-NMR (DMSO, 100.6 MHz): δ= 166.51 (Cq; C^{9}(O)OH); 158.98 (Cq; Ar-C^{4}-OH); 144.54 (Cq; Ar-C^{5}-Ar); 140.02 (Cq; Ar-C^{2}-Ar); 130.23 (Cq; Ar-C^{8}-C(O)OCH$_3$); 129.10 (Ar-C^{6}H); 127.60 (Ar-C^{7}H); 117.15 (Ar-C^{1}H); 114.31 (Ar-C^{3}H); 52.62 (O-C^{10}H$_3$).

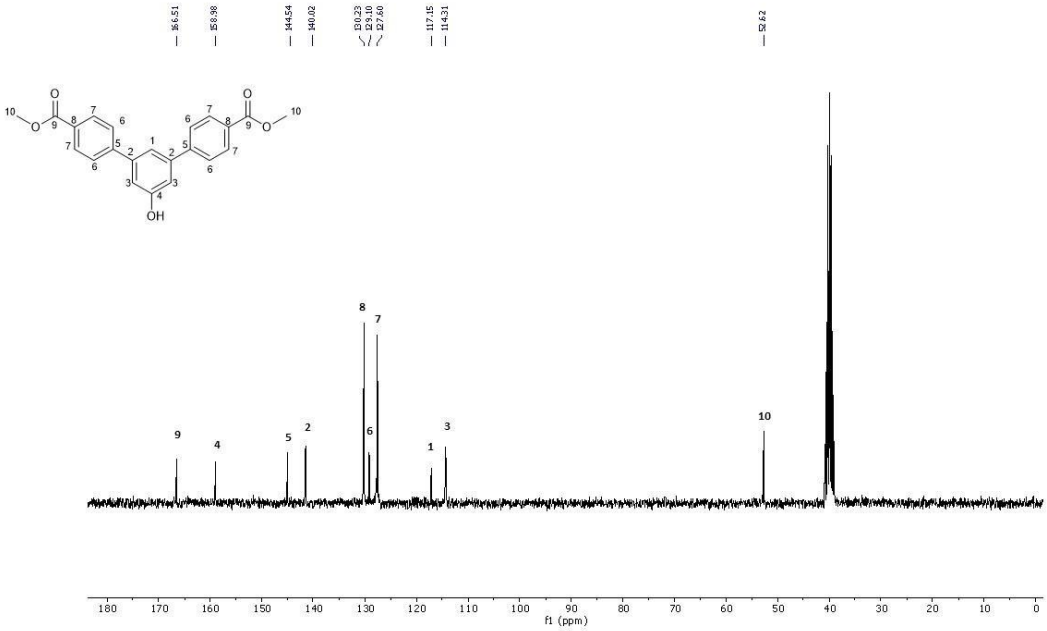

Fig. 2.15: ^{13}C-NMR spectrum of **8**.

ATR-FTIR spectra of neat 8 (cm^{-1}): 3361 (ν O-H alcol, m), 1696 (ν C(O)OH, s), 1276 (ν C-O acid, s), 1192 (ν C-O alcol, s), 845 (δ C-H aromatic), 766 (δ C-H aromatic).

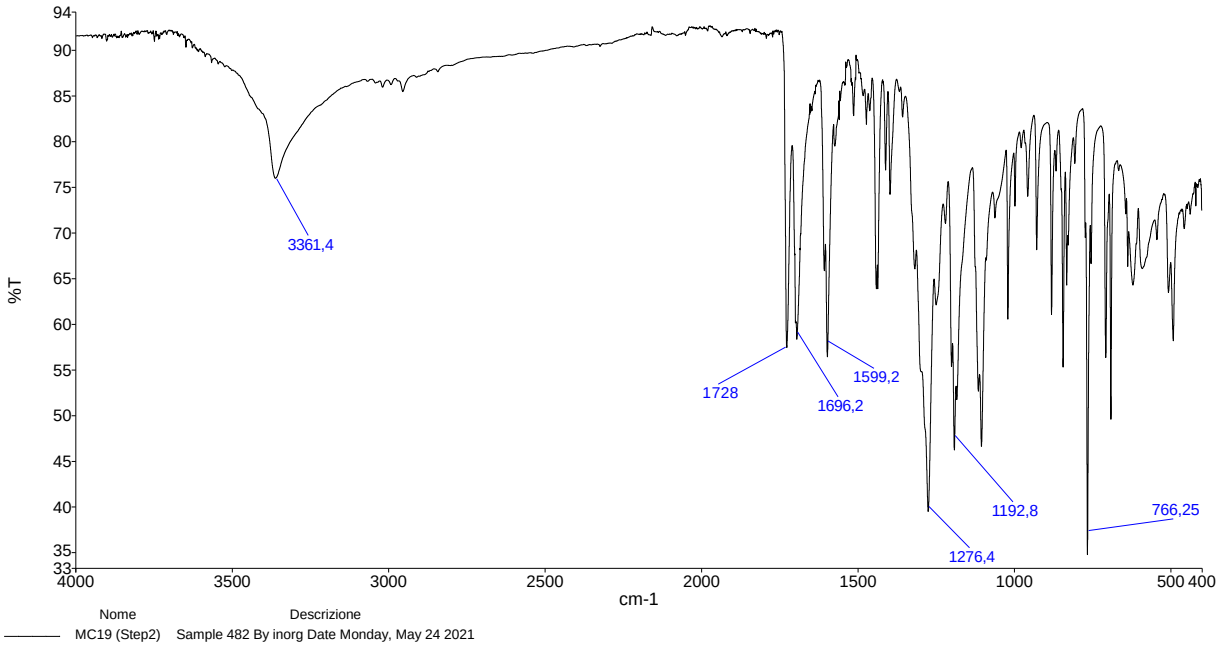

Fig. 2.16: IR-ATR spectrum of **8**.

2.2.2.3 Synthesis of dimethyl 5'-(2-(((prop-2-yn-1-yloxy)carbonyl)amino)ethoxy)-[1,1':3',1''-terphenyl]-4,4''-dicarboxylate (9)

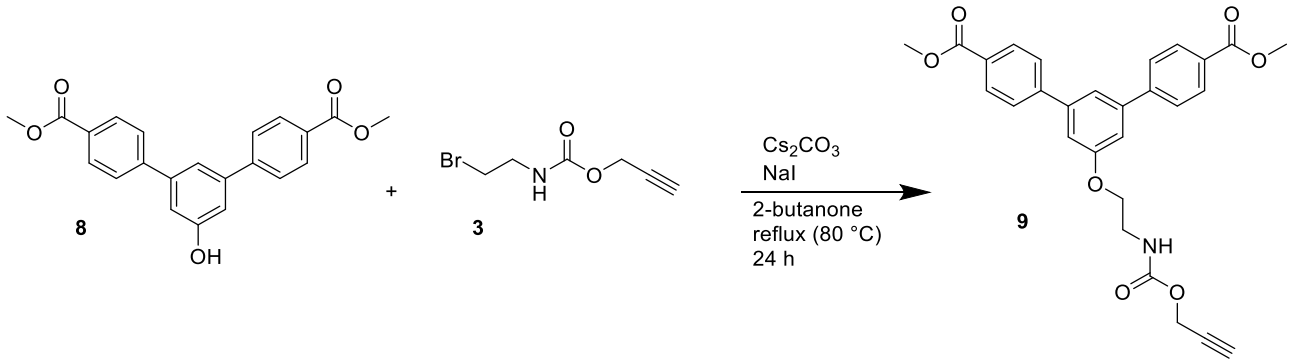

Scheme 2.6: synthesis of **(10)**.

A solution of **8** (1.208 g, 3.3 mmol, 1.5 eq) and **3** 0.451 g, 2.2 mmol) in 2-butanone (30 mL) is treated with Cs_2CO_3 (1.075 g, 3.3 mmol, 1.5 eq) and NaI (0.494 g, 3.3 mmol, 1.5 eq). The solution is stirred at reflux temperature (80 °C) for 24 hours. The solution is then cooled down at room temperature, concentrated in vacuum and diluted with CH_2Cl_2 (25 mL) and NaOH 10% w/w (25 mL). With a separating funnel the aqueous layer and the organic layer are divided. The aqueous layer is washed with CH_2Cl_2 (3 x 20 mL) and the washings are added to the organic phase. The organic layer is washed with NaOH 10% w/w (3 x 20 mL), then dried with Mg_2SO_4,

filtered, and dried under vacuum overnight. The final product is a light-brown sticky solid (0.86 g, 1.76 mmol, 80% yield). Rf (in Petroleum Ether/ Ethyl Ether 1:2): 0.32.

ESI-MS(-) (MeOH, m/z): 510 (100) $[C_{28}H_{25}NO_7+Na]^+$.

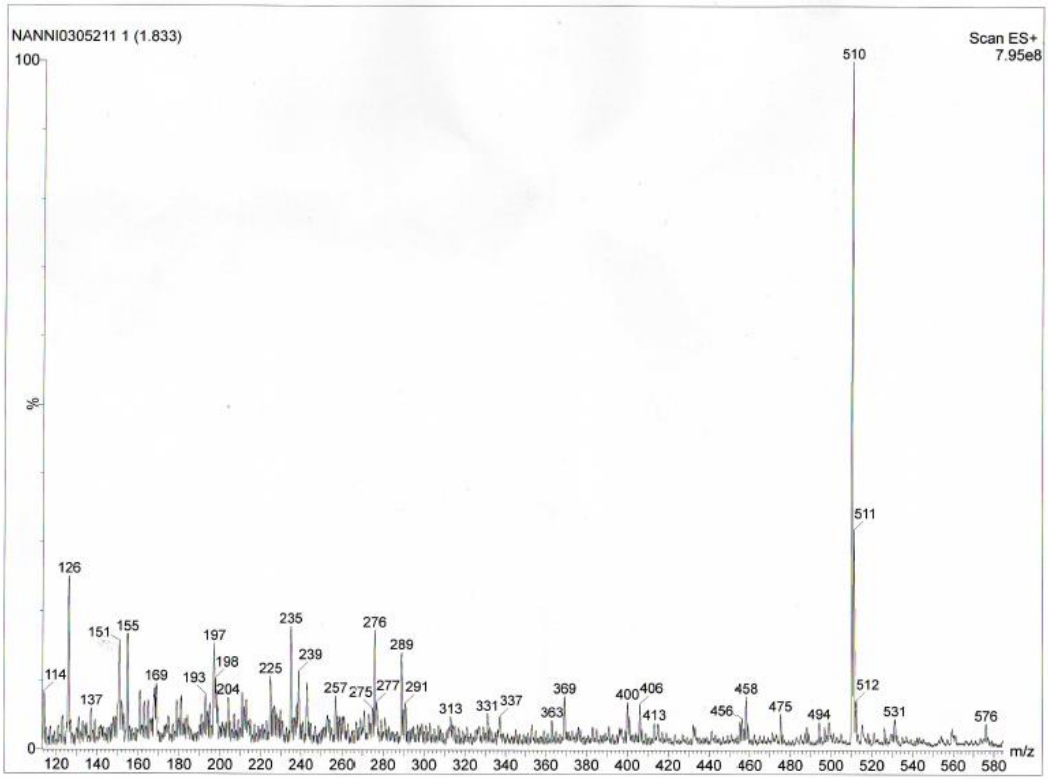

Fig. 2.17: ESI-MS(+) spectrum of **9**.

^{1}H-NMR (300 MHz, DMSO): δ= 8.04 (d, ^{3}J=8.55, 4H; Ar-*H*^{4});7.93 (d, ^{3}J=8.55, 4H; Ar-*H*^{3}); 7.63 (t, ^{4}J=1.50, 1H; Ar-*H*^{1}); 7.32 (d; ^{4}J=1.50, 2H; Ar-*H*^{2}); 4.62 (d; ^{4}J=2.4; 2H; O-*C*H$_2^{9}$); 4.16 (t; ^{3}J=5.4, 2H; O-*C*H$_2^{6}$); 3.89 (s; 6H; O-C*H*$_3^{5}$) 3.46 (t, ^{4}J=2.4; 1H, C≡C*H*^{10}); 3.42 (t, ^{3}J=5.4, 2H; NH-C*H*$_2^{7}$)

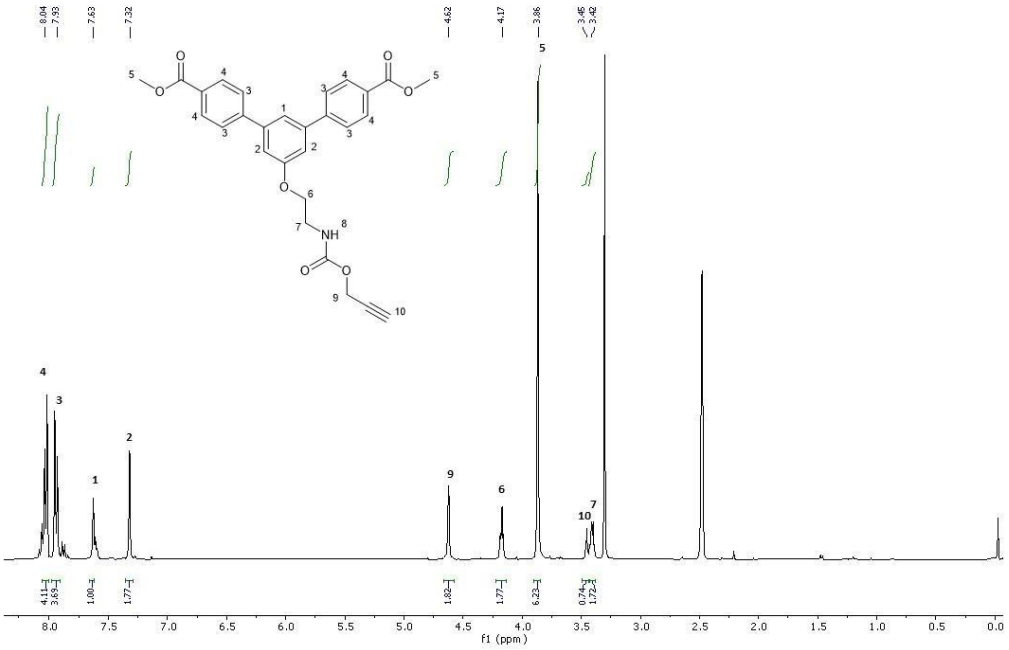

Fig. 2.18: ^{1}H-NMR spectrum of **9**.

^{13}C-NMR (DMSO, 100.6 MHz): δ= 166.49 (Cq; *C*^{9}(O)OCH$_3$); 159.93 (Cq; Ar-*C*^{4}-OCH$_2$); 155.94 (Cq; NH-*C*^{13}(O)O); 144.57 (Cq; Ar-*C*^{5}-Ar); 141.51 (Cq; Ar-*C*^{3}-Ar); 130.32 (Cq; Ar-*C*^{6}-C(O)OCH$_3$); 129.22 (Ar-*C*^{8}H); 127.80 (Ar-*C*^{7}H); 118.31 (Ar-*C*^{1}H); 113.67 (Ar-*C*^{2}H); 79.77 (-CH$_2$-*C*^{15}≡CH); 77.58 (-C≡*C*^{16}H); 67.15 (-O-*C*^{11}H$_2$-); 52.63 (-O-*C*^{14}H$_2$-); 52.05 (-O-*C*^{10}H$_3$);

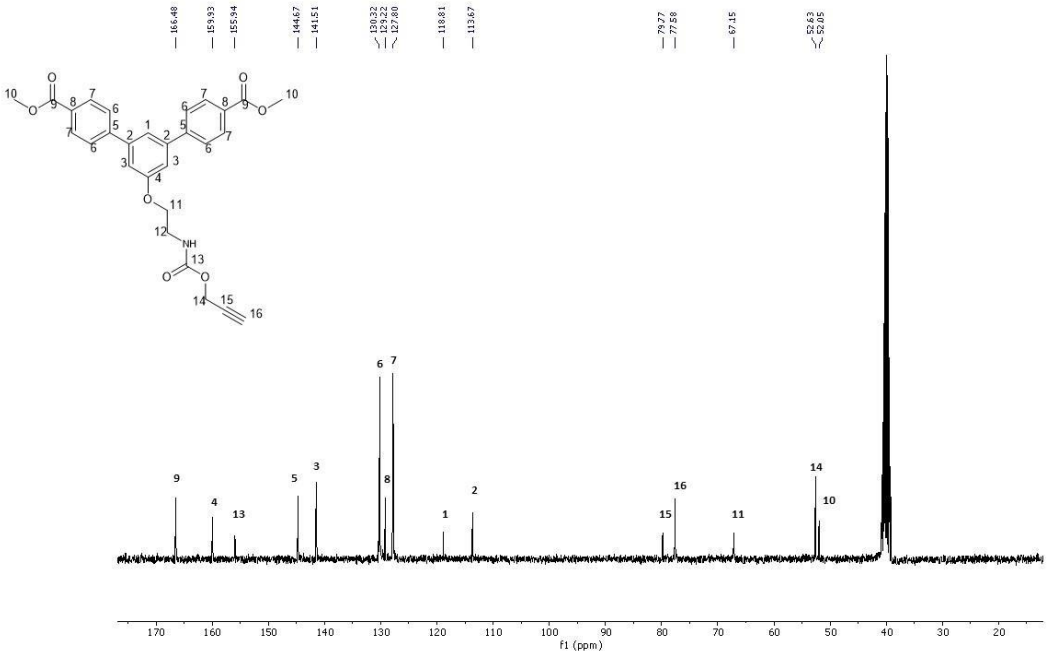

Fig. 2.19: ^{13}C-NMR spectrum of **9**.

ATR-FTIR spectra of neat (10) (cm^{-1}): 3298 (ν ≡C-H), 2958 (ν C-H aliphatic, w), 2130 (ν C≡C), 1713 (ν C(O)OCH_3, s), 1606 (ν C=O, s), 1535 (ν N-H, s), 1281(ν -C(O)O-), 808 (δ bending), 767 (δ bending).

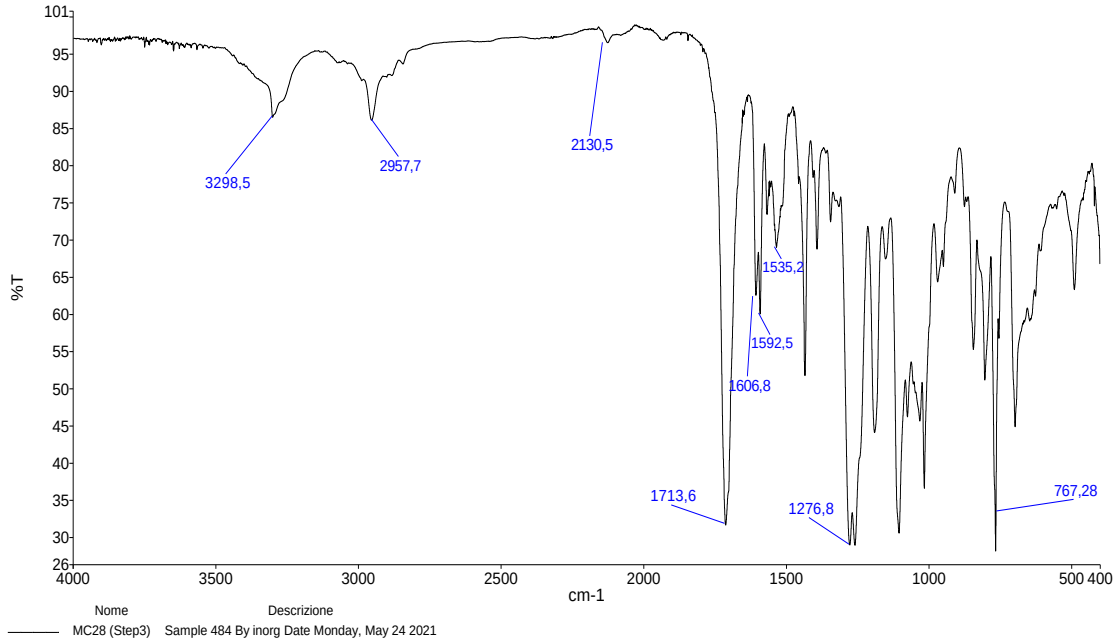

Fig. 2.20: IR-ATR spectrum of **9**.

2.2.2.4 Synthesis of 5'-(2-(((prop-2-yn-1-yloxy)carbonyl)amino)ethoxy)-[1,1':3',1''-terphenyl]-4,4''-dicarboxylic acid (10, H_2YL80)

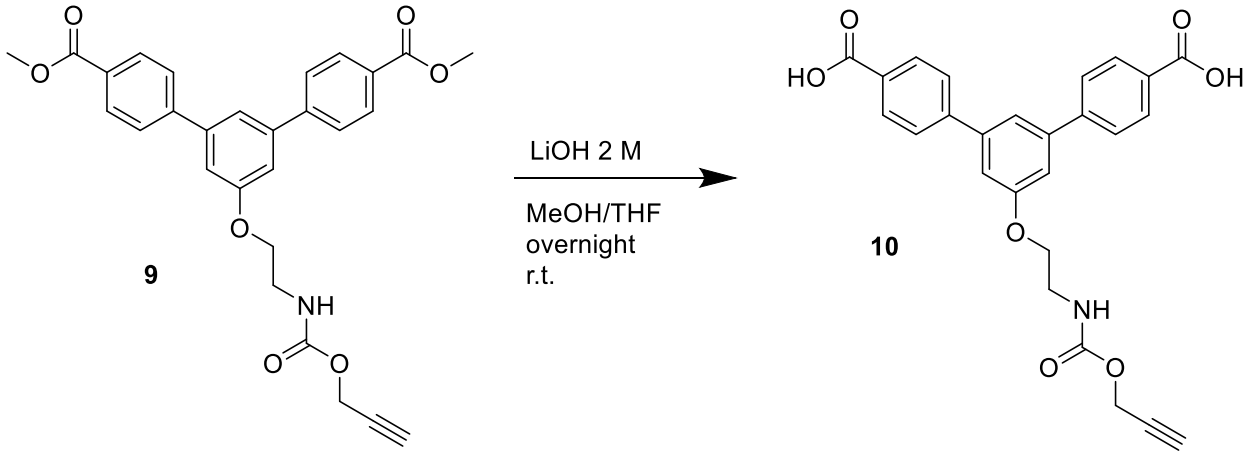

Scheme 2.7: synthesis of **10**.

A solution of **9** (0.82 g, 1.68 mmol) is prepared using a mixture of Methanol/THF 1:1 (20 mL). The system is put under magnetic stirring, and a solution of LiOH 2 M is added (4.2 mL, 8.4 mmol, 5 eq). The solution is stirred overnight at room temperature, then is concentrated under vacuum, and diluted with DI water (10 mL). The system is then treated with HCl 1 M (15 x 1 mL) and the formation of a white precipitate is observed. The solution is filtered and the solid

is washed with DI water (50 mL) and dried in the oven overnight. The resulting product is a white solid (0.588 g, 1,28 mmol, 76% yield). Rf (in Petroleum Ether/ Ethyl Ether 1:2): 0.15.

ESI-MS(-) (MeOH, m/z): 482 (100) $[C_{26}H_{21}NO_7 + Na]^+$.

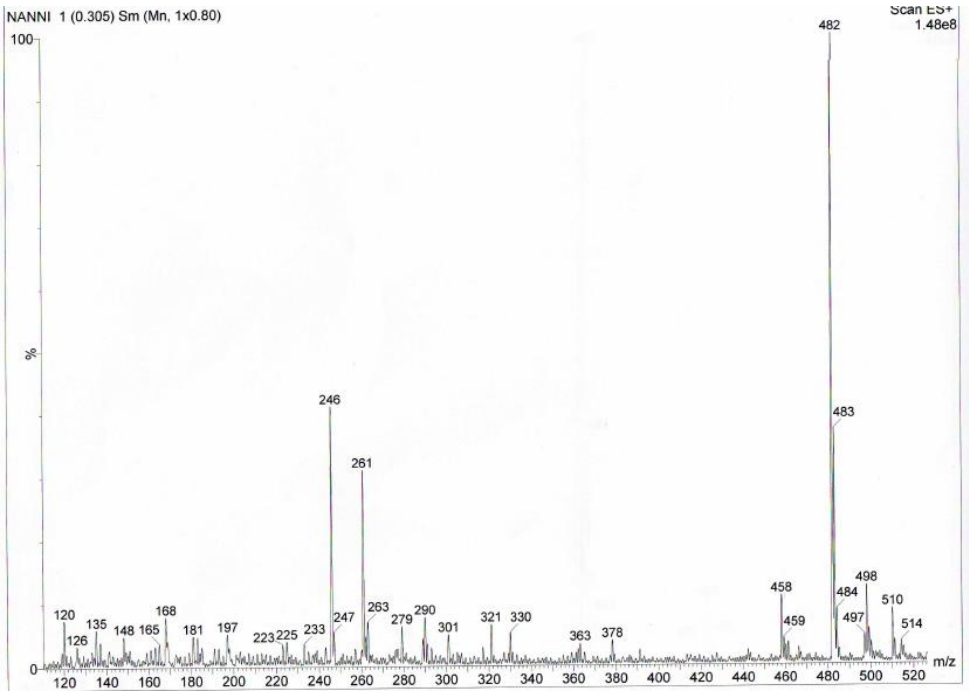

Fig. 2.21: ESI-MS(+) spectrum of **(7)**.

^{1}H-NMR (300 MHz, DMSO): δ= 8.02 (d, ^{3}J=8.55, 4H; Ar-*H*^{4}); 7.92 (d, ^{3}J=8.55, 4H; Ar-*H*^{3}); 7.62 (t, ^{4}J=1.50, 1H; Ar-*H*^{1}); 7.31 (d; ^{4}J=1.50, 2H; Ar-*H*^{2}); 4.62 (d; ^{4}J=2.4; 2H; O-*C*H$_2^9$); 4.18 (t; ^{3}J=5.4, 2H; O-*C*H$_2^6$); 3.48 (t, ^{4}J=2.4; 1H, C≡C*H*^{10}); 3.42 (t, ^{3}J=5.4, 2H; NH-C*H*$_2^7$).

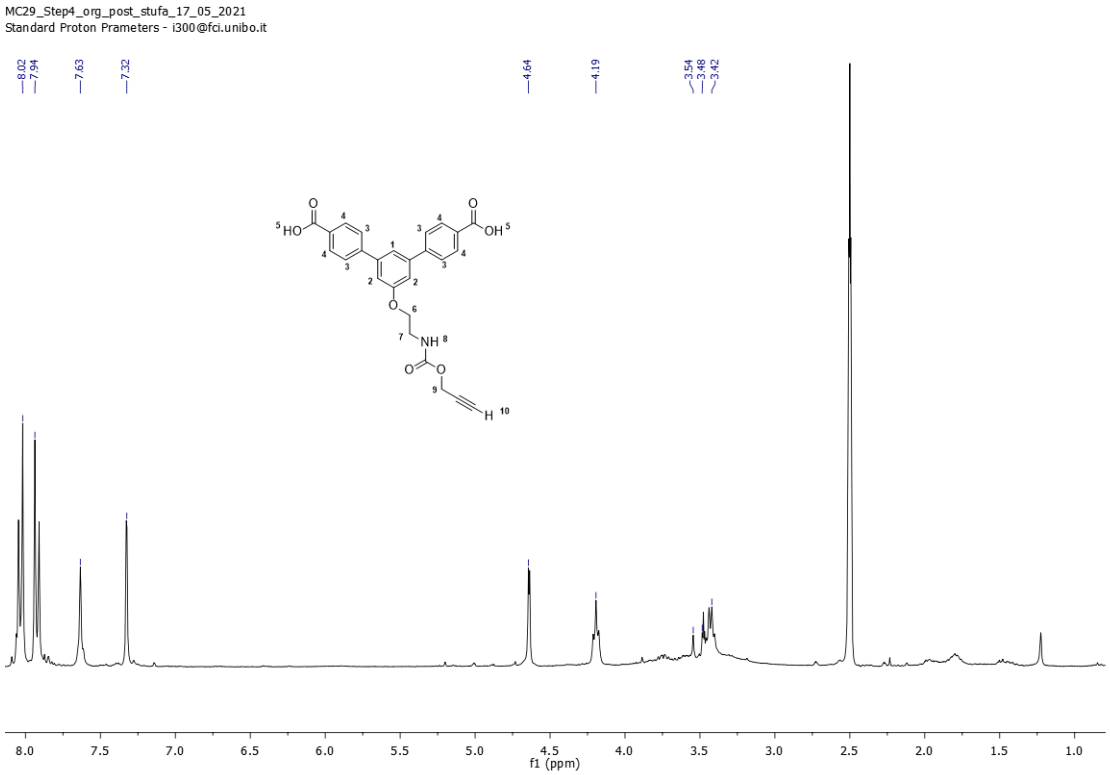

Fig. 2.22: ^{1}H-NMR spectrum of **10** in DMSO.

^{1}H-NMR (300 MHz, MeOH): δ=8.10 (d, ^{3}J=7.80, 4H; Ar-*H*^{4}); 7.82 (d, ^{3}J=7.80, 4H; Ar-*H*^{3}); 7.55 (t, ^{4}J=1.45, 1H; Ar-*H*^{1}); 7.28 (d; ^{4}J=1.50, 2H; Ar-*H*^{2}); 4.67 (d; ^{4}J=2.4; 2H; O-*C*H$_2^{9}$); 4.20 (t; ^{3}J=5.4, 2H; O-*C*H$_2^{6}$); 3.57 (t, ^{3}J=5.4, 2H; NH-C*H*$_2^{7}$) 2.86 (t, ^{4}J=2.4; 1H, C≡C*H*^{10}).

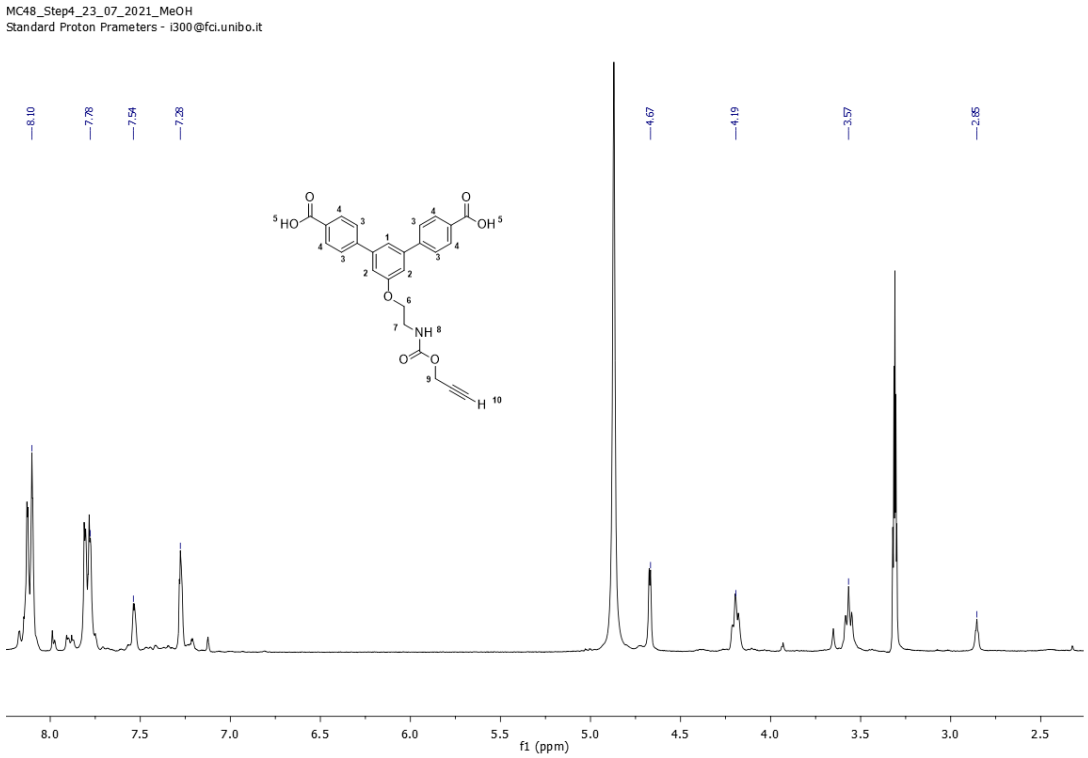

Fig. 2.23: ^{1}H-NMR spectrum of **10** in MeOH.

^{13}C-NMR (DMSO, 100.6 MHz) δ: 167.16 (Cq, *C*^{9}(O)OH); 159.48 (Cq; Ar-*C*^{4}-OCH$_2$); 155.51 (Cq; NH-*C*^{12}(O)O); 143.36 (Cq; Ar-*C*^{5}-Ar); 141.27 (Cq; Ar-*C*^{2}-Ar); 129.88 (Cq; Ar-*C*^{8}-C(O)OCH$_3$); 127.20 (Ar-*C*^{6}H); 122.83 (Ar-*C*^{7}H); 118.37 (Ar-*C*^{1}H); 113.09 (Ar-*C*^{3}H); 79.35 (-CH$_2$-*C*^{14}≡CH); 77.14 (-C≡*C*^{15}H).

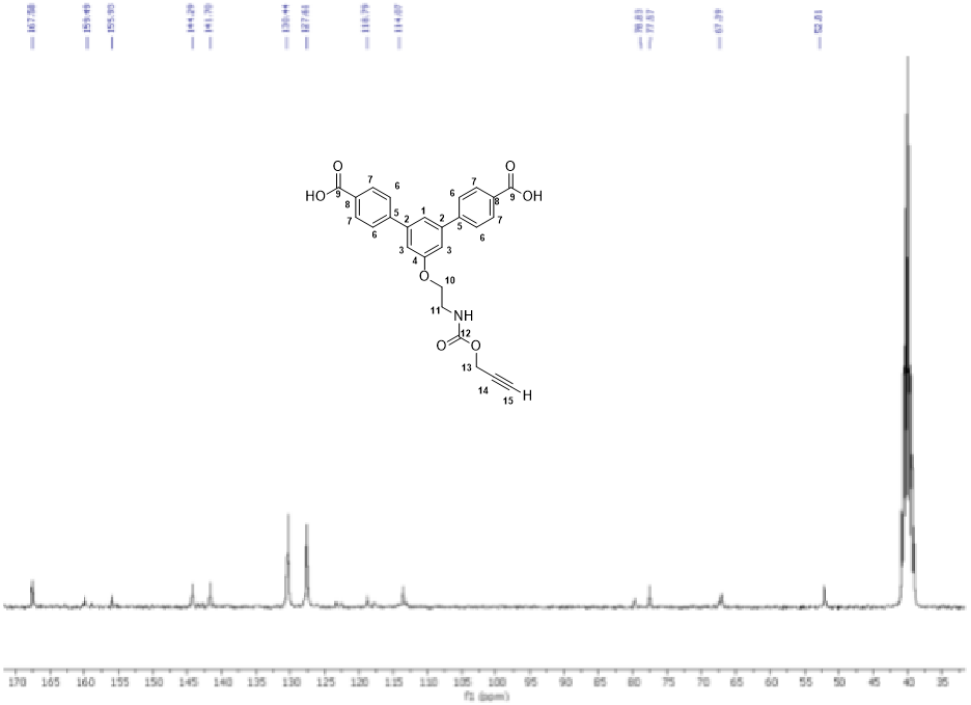

Fig. 2.24: ^{13}C-NMR spectrum of **10**.

ATR-FTIR spectra of neat 10 (cm^{-1}): 3294 (ν O-H), 2960 (ν C-H aliphatic, w), 1687 (ν C(O)OCH$_3$, s), 1606 (ν C=O, s), 1528 (ν N-H, s), 1292 (ν -C(O)O-), 768 (δ bending).

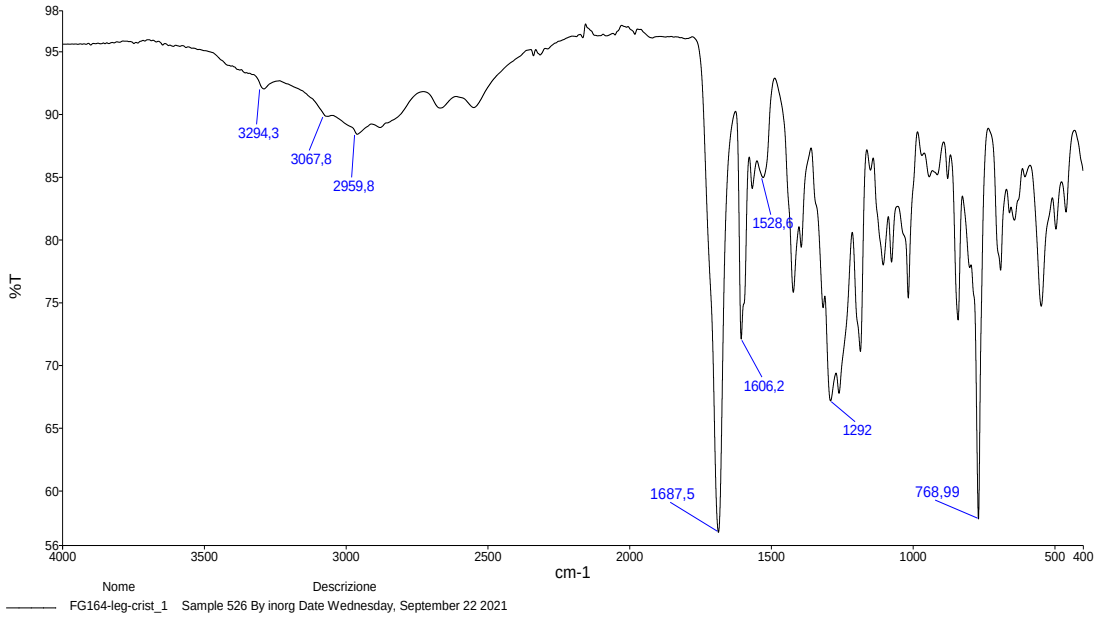

Fig. 2.25: ATR-IR spectrum of **10**.

2.3 Crystallisation of H_2YL80

H_2YL80 (0.414 g, 0.9 mmol) is put in 20 mL of ethanol. At room temperature it appears mostly insoluble in this solvent. The solvent is heated to its boiling point (78 °C) and most of H_2YL80 dissolves. After 5 minutes, the solution is cooled down to 0 °C and the flask is left in an ice bath for 30 minutes. No precipitation is observed, so the solution is put at -18 °C overnight. The following day, seeing that no precipitate has still formed, the flask is put again in the ice bath and DI water (4 x 10 mL) is added, causing the formation of a white precipitate. The precipitate is filtered and washed with DI water. Keeping the mother solution in the ice bath, additional DI water (4 x 10 mL) is added, and further precipitation of a white solid is observed. This new precipitated is also filtered and washed with DI water. The process is repeated two other times, with the additional precaution of filtering the boiling ethanol solution to remove the insoluble residuals.

2.4 Synthesis of the new Cu-MOF

2.4.1 Synthesis in 2-propanol (MC35)

A solution of H_2YL80 (0.176 g, 0.390 mmol) and $Cu(NO_3)_2 \cdot 2.5H_2O$ (0.163 g, 0.701 mmol, 1.8 eq) is prepared in 2-propanol (15 mL). The reaction is carried at reflux temperature (85 °C), under magnetic stirring (300 rpm). The formation of a light-green solid is observed soon at the beginning of the reaction. After 24 h the reaction is cooled at room temperature, and the product is filtered and washed with 2-propanol (Fig 2.26). The product is dried in the oven overnight. The final product is a light green solid, weighting 0.143 g. Assuming that Cu atoms and the ligand are present in 1:1 stoichiometric rate, we can calculate a 70% yield for the reaction.

Fig. 2.26: The product of the MOF synthesis in 2-propanol after the washing with 2-propanol.

2.4.2 Synthesis in DMF/H_2O 3:1 (MC46)

A solution of H_2YL80 (0.057 g, 0.125 mmol) and $Cu(NO_3)_2 \cdot 2.5H_2O$ (0.058 g, 0.250 mmol, 2 eq) is prepared in DMF/H_2O 3:1 (8 mL) in a closed vial. The solution was heated at 50 °C without stirring for a total of 168 h (1 week). After the first 24 h a green-blue solid starts appearing at the interface of the solution. After 48 h on the bottom of the vial a white solid starts forming, while the presence of the green-blue solid increases. At the end of the 168 h the solution is cooled down to room temperature and the product (Fig. 2.27) is filtered, washed with H_2O, and dried in the oven overnight. The final product is a light green solid, mixed with traces of the white solid. The total weight is 0.030 g. Assuming that Cu atoms and the ligand are present in 1:1 stoichiometric rate, we can calculate a 46% yield for the reaction.

Fig. 2.27: Synthesis in DMF/H_2O 3:1 of the new Cu-MOF, after 168 hours, before the work-up.

2.4.3 Synthesis in DMF/H_2O 4:1 under inert atmosphere (MC51)

A solution of H_2YL80 (0.057 g, 0.125 mmol) and $Cu(NO_3)_2 \cdot 2.5H_2O$ (0.058 g, 0.250 mmol, 2 eq) is prepared in DMF/H_2O 4:1 (8 mL) in a closed vial previously put under N_2 atmosphere. The solution is put under magnetic stirring for 10 minutes until the ligand is completely dissolved. The solution is then heated at 50 °C without stirring for a total of 168 h (1 week). After 24 h the formation of a green solid in small quantities at the interface of the solution is observed. After 48 h the green solid starts growing also on the walls and the bottom of the vial. Neither the formation of white solid nor brown oxides is observed during the whole time (Fig. 2.28). After 168 h, the reaction is cooled down at room temperature. The product is put in a Petri capsule, and the solvent is removed by decantation using a Pasteur pipette. The product is washed with DI water directly in the capsule and the washings are removed by decantation using a Pasteur pipette (filtration was avoided to minimise the material loss). The final product (Fig. 2.29) is dried in the oven overnight. The final product is a green solid, weighting 0.046 g. Assuming that Cu atoms and the ligand are present in 1:1 stoichiometric rate, we can calculate a 70% yield for the reaction.

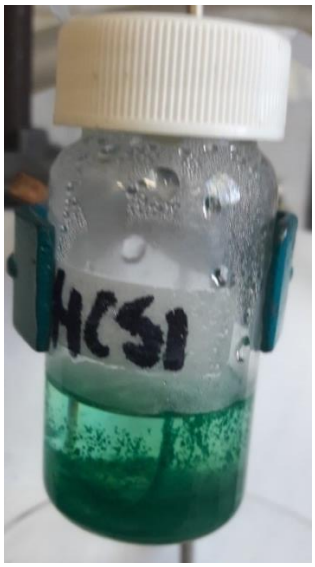

Fig. 2.28: Synthesis in DMF/H_2O 4:1 of the new Cu-MOF after 168 hours, before the work-up.

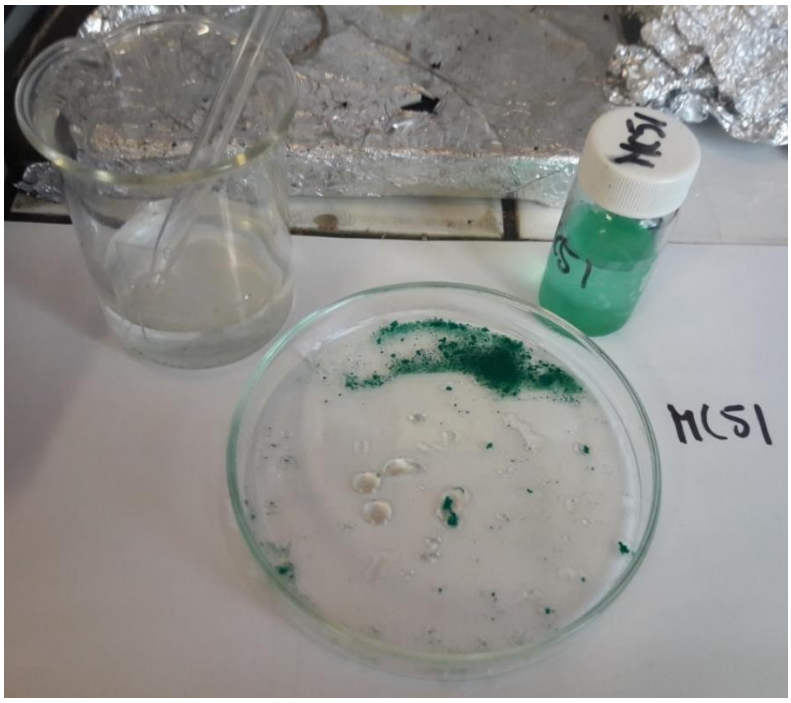

Fig. 2.29: The product of MC51 after the washings in the Petri capsule.

2.4.4 Synthesis in DMF/H_2O/2-propanol 2:1:1 under inert atmosphere (MC52)

A solution of H_2YL80 (0.057 g, 0.125 mmol) and $Cu(NO_3)_2 \cdot 2.5H_2O$ (0.058 g, 0.250 mmol, 2 eq) is prepared in DMF/H_2O/2-propanol 2:1:1 (8 mL) in a closed vial previously put under N_2 atmosphere. The solution is put under magnetic stirring for 10 min until the ligand is completely dissolved. The solution is then heated at 50 °C without stirring for a total of 168 h (1 week). After 48 h on the bottom of the vial begins the formation of a green solid, whose quantity increases slowly during the following days (Fig. 2.30). After 168 h the reaction is cooled down

to room temperature. The product is put in a Petri capsule, and the solvent is removed by decantation using a Pasteur pipette. The product is washed with DI water directly in the capsule and the washings are removed by decantation using a Pasteur pipette (filtration was avoided to minimise the material loss). The final product (Fig. 2.31) is dried in the oven overnight. The final product is a green solid, weighting 0.040 g. Assuming that Cu atoms and the ligand are present in 1:1 stoichiometric rate, we can calculate a 61% yield for the reaction.

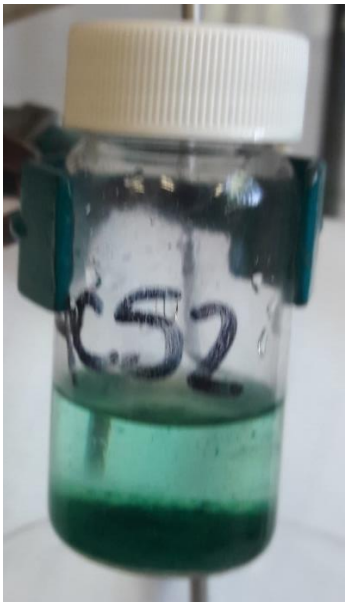

Fig. 2.30: Synthesis in DMF/H_2O/2-propanol 2:1:1 of the new Cu-MOF after 168 h, before the work-up. Notice that the solid is almost all deposited on the bottom of the vial, while in MC51 it also grew on the walls and at the interface of the solution.

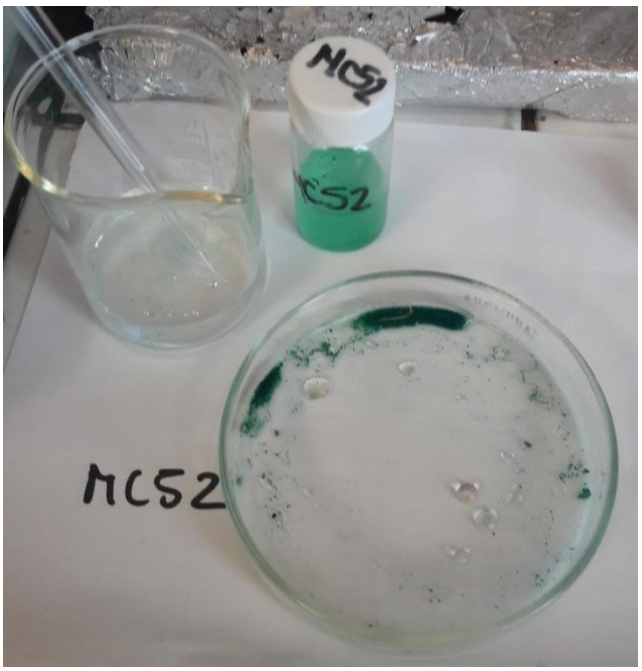

Fig. 2.31: The product of MC52 after the washings in the Petri capsule.

2.4.5 Synthesis in DMF/H_2O 4:1 under inert atmosphere at reduced ligand concentration (MC53)

A solution of H_2YL80 (0.057 g, 0.125 mmol) and $Cu(NO_3)_2 \cdot 2.5H_2O$ (0.058 g, 0.250 mmol, 2 eq) is prepared in DMF/H_2O 4:1 (16 mL) in a closed vial previously put under N_2 atmosphere. The solution is heated at 50 °C without stirring for a total of 168 h. After 24 h no formation of solid is observed. After 96 h the formation of a turquoise-green solid at the interface of the solution is observed, with the precipitation of the heavier crystals to the bottom of the vial (Fig. 2.32).

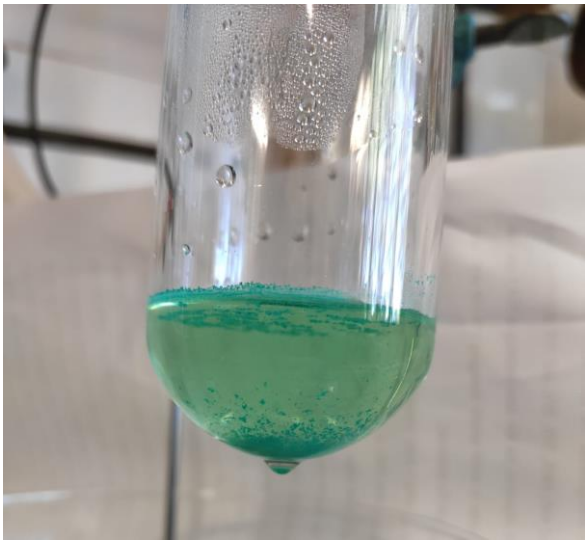

Fig. 2.32: Formation of solid during the synthesis of the new Cu-MOF in DMF/H_2O 4:1 under inert atmosphere at reduced ligand concentration after 96 h.

After 168 h the reaction is cooled down to room temperature and the solvents are separated through decantation. The solid product is washed with DI water (3 x 20 mL). The washings are separated through decantation, and the washings result do be turbid due to the presence of traces of white solid, maybe containing part of the unreacted ligand. The product is then washed with ethanol (20 mL), and this time the washings appear to be clear. The washings are removed through decantation and the resulting solid is dried in the oven for 24 hours. The final product is a green solid, weighting 0.023 g. Assuming that Cu atoms and the ligand are present in 1:1 stoichiometric rate, we can calculate a 35% yield for the reaction.

2.5 Reactivity of [Cu(1,3-YBDC)]·xH_2O towards $HAuCl_4$

2.5.1 MeOH, 65 °C, 10 wt% w_{Au}/w_{MOF}

To a suspension of [Cu(1,3-YBDC)]·xH_2O (0.250 g) in MeOH (120 mL), $HAuCl_4x3H_2O$ (0.050 g, 0.127 mmol) was added. The reaction mixture was stirred for 1 h at r.t. and the solid

successively was separated from the supernatant by centrifugation at 5400 rpm for 15 min. After three cycles of washings with MeOH (3x20 mL) and centrifugations the product was divided in two parts: one half was placed in MeOH (30 mL) at 65 °C for 1 h under stirring (FG130a). The second half was placed in MeOH (30 mL) at 65 °C for 24 h under stirring (FG130b). After that, the solid was again separated by centrifugation and washed with MeOH.

2.5.2 Butanol, 118 °C, 10 wt% w_{Au}/w_{MOF}

To a suspension of [Cu(1,3-YBDC)]·xH_2O (0.250 g) in MeOH (120 mL), $HAuCl_4x3H_2O$ (0.050 g, 0.127 mmol) was added. The reaction mixture was stirred for 1 h at r.t. and the solid successively was separated from the supernatant by centrifugation at 5400 rpm for 15 min. After three cycles of washings with MeOH (3x20 mL) and centrifugations the product was divided in two parts: one half was placed in butanol (30 mL) at 118 °C for 1 h under stirring (FG131a). The second half was placed in butanol (30 mL) at 118 °C for 24 h under stirring (FG131b). After that, the solid was again separated by centrifugation and washed with MeOH.

2.6 Determination of Au percentage in the Cu-[YBDC]/Au MOF used for MB adsorption through AAS

The instrument is calibrated using standard solutions at different concentrations (0.1, 0.2, 0.3, 0.5, 1, 2, 3, 4 and 6 ppm) obtained by dilution of a mother solution of Au 110 ppm in HCl 0.5 M. The Absorbance/Concentration relationship obtained is described by the following linear equation (Fig. 2.33):

$$Y = 0.03115X + 0.0045 \quad (14)$$

with R^2=0.9912 (the points at concentration of 1 and 3 ppm were discarded because they were too scattered).

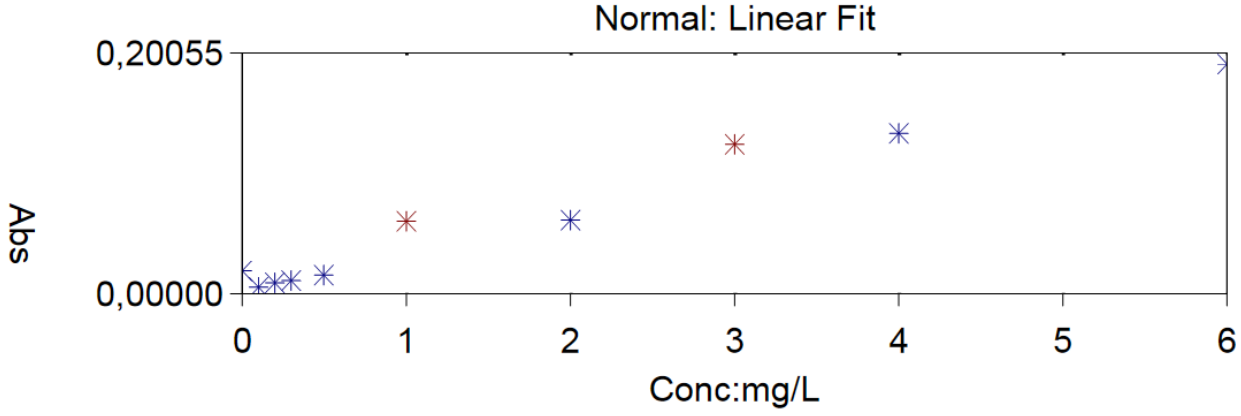

Fig. 2.33: Calibration curve for the AAS measurements.

The MOF sample is prepared by weighting 10.2 mg of Cu-[YBDC]/Au MOF in a 25 mL matrass. The sample is dissolved in hot aqua regia, added dropwise until the solid is completely dissolved, then the matrass is taken to volume with HCl 0.5 M. The absorbance solution is measured, and the resulting value is 0.113, corresponding to a concentration of 3.48 ppm. Considering the volume of the sample, we can calculate that the mass of Au present in the solution is 0.087 mg, corresponding to a percentage of Au in the Cu-[YBDC]/Au MOF sample of 0.85%.

2.7 Adsorption kinetics of Methylene Blue (MB) over [Cu(1,3-YBDC)]·xH_2O

All the experiments were carried by following the same general set-up:

- 150 mL of a standard solution of MB are put in a flask under magnetic stirring;
- A weighted quantity of the MOF is added to the solution. At the same time, a chronometer is started;
- At fixed time intervals, a 4 mL sample of the suspension is taken, and put under centrifugation at 6000 rpm for 5 min, to separate the MOF from the solution;
- The supernatant is taken, and its absorbance is measured at the UV-Vis spectrophotometer (scan range: 800-320 nm, absorbance peak for MB at 664 nm). In some cases, if the predicted concentration of the sample is too high (outside the interval of linearity for the Absorbance/Concentration relationship), a 1000 μL sample is taken with a micropipette, put in a 10 mL matrass and make up to mark (1:10 dilution).

Most of the experiments were carried by using 50 mg of [Cu(1,3-YBDC)]·xH_2O and varying the initial concentration of MB in the standard solution (4 ppm, 20 ppm and 40 ppm). One additional experiment was carried adding 100 mg of [Cu(1,3-YBDC)]·xH_2O to a 40 ppm solution of MB. Another experiment was performed by adding 50 mg of [Cu(1,3-YBDC)]·xH_2O/Au (0.85% of Au, measured with AAS, see chapter 2.6) to a 40 ppm solution of MB, to see if the presence of gold nanoparticles on the adsorbent material could influence the adsorption. All the experiments were performed at room temperature and pressure. The conditions employed in each experiment are reported in table 2.1.

Table 2.1: Conditions employed for the experimental determination of the adsorption kinetics of MB over [Cu(1,3-YBDC)]·xH_2O.

	MOF type	MOF quantity	MB starting concentration
A)	[Cu(1,3-YBDC)]·xH_2O	50 mg	4 ppm
B)	[Cu(1,3-YBDC)]·xH_2O	50 mg	20 ppm
C)	[Cu(1,3-YBDC)]·xH_2O	50 mg	40 ppm
D)	[Cu(1,3-YBDC)]·xH_2O/Au	50 mg	40 ppm
E)	[Cu(1,3-YBDC)]·xH_2O	100 mg	40 ppm
All the experiments were performed at room temperature and atmospheric pressure, under constant magnetic stirring. The volume of the starting MB solution was 150 mL.			

Chapter 3

3 Results and discussion

In this chapter, the synthesis of a new carboxylate-based ligand with a propargyl-carbamate group and of the corresponding Cu-based MOF is described.

3.1 New ligand synthesis

3.1.1 First synthetic approach

The first synthetic path proposed for the synthesis of the new ligand H_2YL80 is illustrated in Scheme 3.1. It is a three-step synthesis. The first step consists in the condensation of commercially available propargyl-chloroformate **(1)** and bromoethylamine **(2)**, yielding the carbamate **(3)**. The second step is the substitution of the Br atom of **(3)** with the oxygen atom of commercially available 3,5-dibromophenol **(4)** to obtain the substituted carbamate **(5)**. The final step involves a Suzuki reaction between the substrate **(5)** and two equivalents of 4-boronobenzoic acid **(6)**, to obtain the new ligand **(10)**.

The first step was already used in the synthesis of H_2YBDC,[5] so the procedure was already mostly optimized. The only additional precautions that were taken were to stir the mixture during the final concentration under high vacuum (10^{-2} mmHg), to favour the evaporation of ethyl acetate, and to put the store the product under nitrogen at 4 °C.

The second step did not present any particular issue; Cs_2CO_3 was used to deprotonate the -OH group on the 3,5-dibromophenol in order to make it more reactive towards electrophile groups. NaI was used to exchange the bromide on the carbamate with a iodide, which makes a better leaving group.

The third step, unfortunately, represented an insurmountable obstacle to the success of this synthetic route. The main issue is the difference in the solubility of the two reagents involved in this step. To overcome this problem, numerous expedients were used, such as employing different mixtures of solvents (water/toluene, water/acetonitrile…) and the use of additives like CPME to favour the passage of the hydro-soluble boronic acid from the aqueous phase to the organic phase. Despite several attempts under different reaction conditions (an example is reported in the § 2.2.1.3), in most cases the reagents remained segregated in separate layers and did not come in contact with each other. In addition to that, we suspect that the carbamate group present in **5** could have some undesired interaction with the Pd(II) catalyst used for the Suzuki reaction, in particular due to the presence of the terminal alkyne group.[68,69]

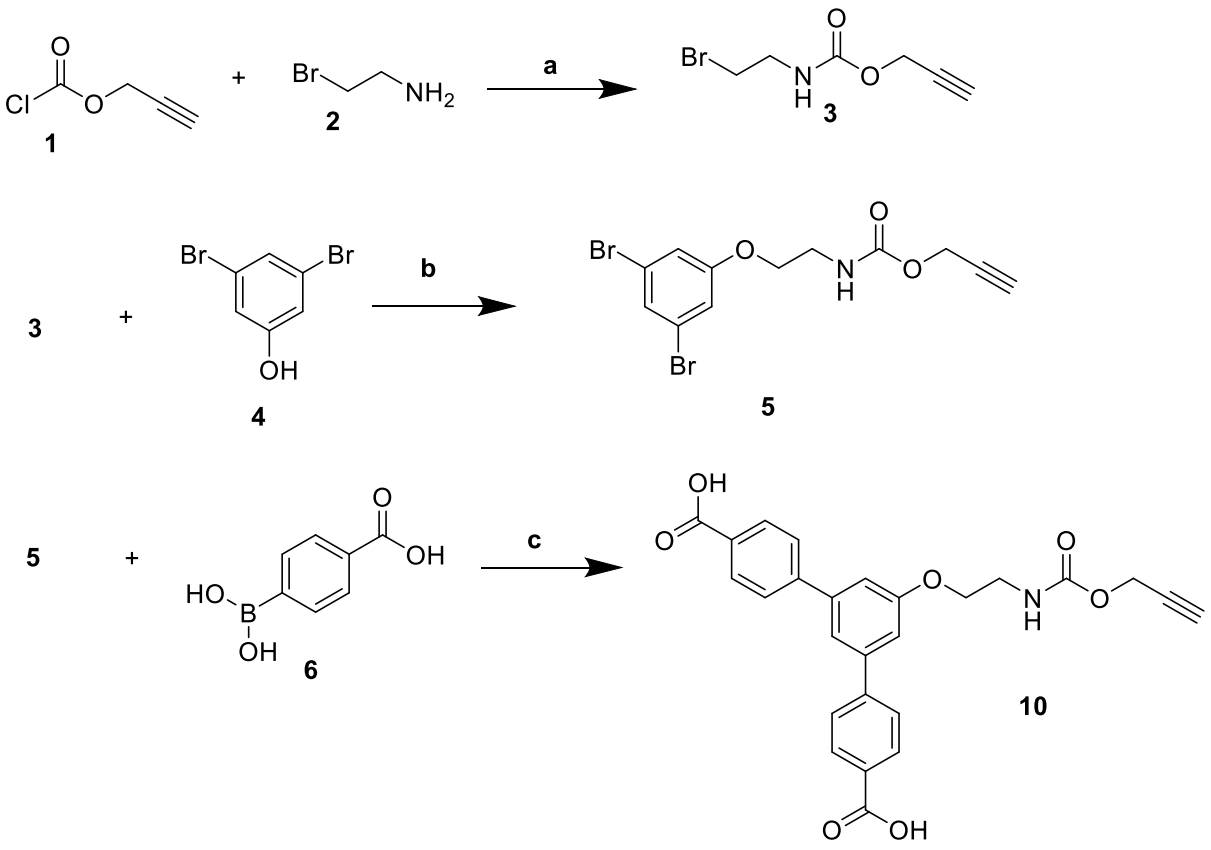

Scheme 3.1: First synthetic route proposed for the new ligand H_2YL80 synthesis. Reagents and conditions: a) $NaHCO_3$ 3 eq, THF/H_2O 1.25:1, overnight; b) Cs_2CO_3 1.5 eq, NaI 1.5 eq, 2-butanone, 80 °C, overnight; c) K_2CO_3 1 M 9.4 eq, Toluene/CPME 19:1, cat. $PdCl_2(PPh_3)_2$, 110 °C, 4 hours.

3.1.2 Second synthetic approach

The second proposed synthetic path for the new ligand synthesis is reported in Scheme 3.2. In this new approach the Suzuki reaction is performed on the unsubstituted 3,5-dibromophenol, and the propargyl-carbamate is added subsequently. This method brings two main benefits. First, it removes the possible interference with the Pd(II) catalyst by the pendant alkyne of the carbamate during the Suzuki reaction. Second, the aromatic rings that undergo the coupling reaction are much more similar to each other compared to the ones involved in the Suzuki reaction of the first approach, therefore their solubility is also similar, and it is easier for the reagents to come into contact.

Nevertheless, also this route also presents a drawback. In fact, due to the presence of the carboxylic acid groups on the diacid **(7)**, the nucleophilic substitution reaction on the bromo-propargyl-carbamate **(3)** cannot be performed without having the carboxylic -OH groups to compete with the phenolic -OH group. Considering that carboxylic acid usually possess a pKa of ~5 and phenols have a pKa of ~10, the acid groups are actually favoured as nucleophiles for the substitution. Therefore, this process requires two additional steps (protection of the

carboxylic acid groups via esterification, and the following deprotection by basic hydrolysis) in order to successfully yield the desired product.

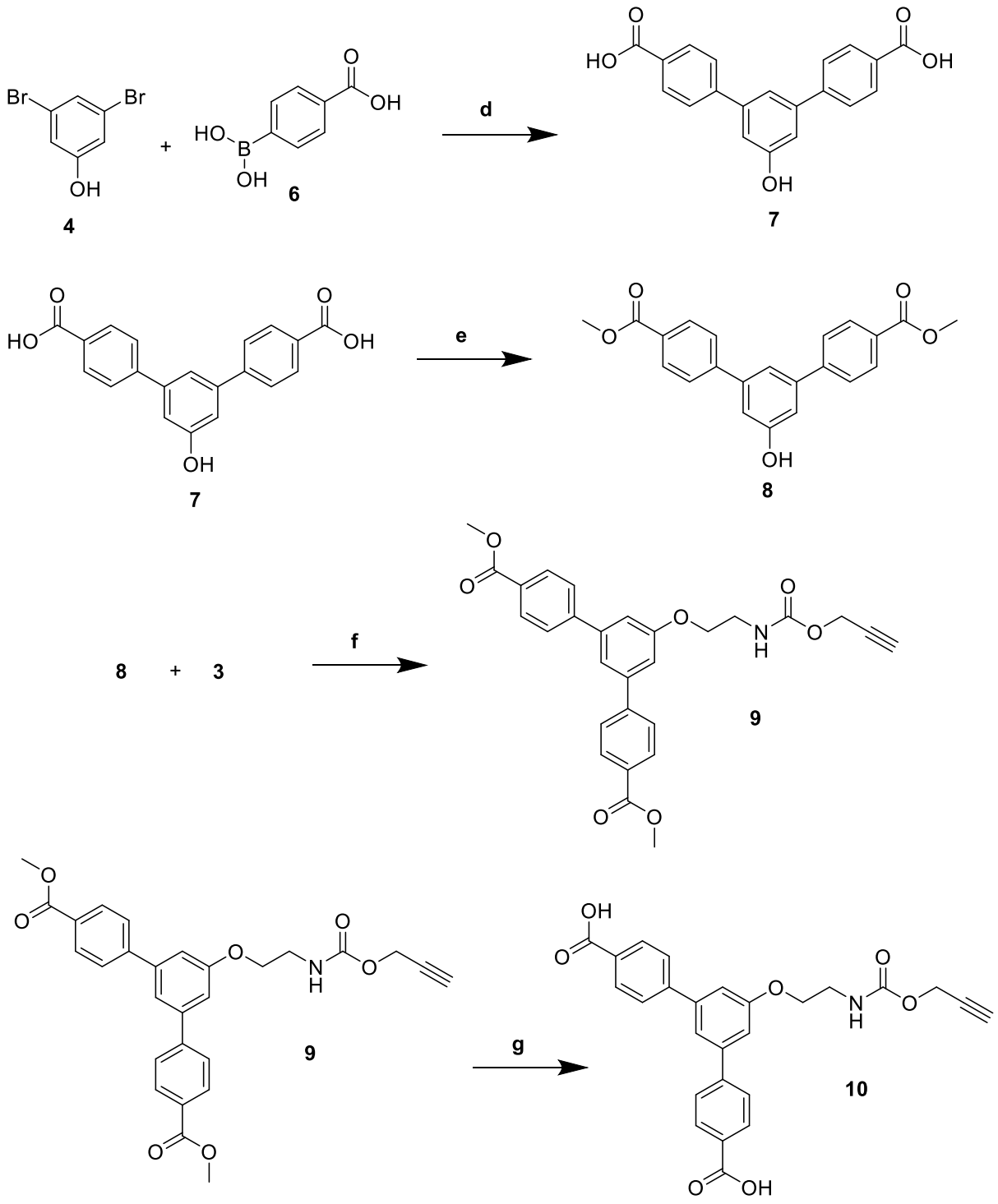

Scheme 3.2: Second synthetic route proposed for the new ligand H_2YL80 synthesis. Reagents and conditions: d) K_2CO_3 1 M 7.4 eq, $PdCl_2(PPh_3)_2$ 0.02 eq, CH_3CN, 100 °C, overnight; e) MeOH, H_2SO_4 conc. 10 eq, 65 °C, 24 hours; f) Cs_2CO_3 1.5 eq, NaI 1.5 eq, 2-butanone, 80 °C, 24 hours; g) LiOH 2 M 5 eq, MeOH/THF 1:1, r.t., overnight.

For the first step we modified a procedure taken from the literature.[70] The original procedure used a 10% catalytic load and a reaction time of 48 hours. After numerous tries we managed to optimise the process, using a 2% catalytic load (smaller catalytic loads result in lower yields) and carrying the reaction overnight.

From the same literary source, we also took the procedure for the second step. In this case, there was no need to further modify the process.

For the third step we based our procedure on the analogue substitution reaction that was used for the synthesis of the ligand H_2YBDC.[5] It required numerous attempts to find the optimal reaction conditions to give the desired product in satisfying yields. Each time, we modified some of the following parameters:

- Solvent: different solvents were tried (DMF, 2-butanone, 2-pentanone). We carried each reaction in reflux conditions, so the different boiling points of the solvent influenced the temperature the reactions were carried at.
- Carbamate/diester ratio: the unreacted carbamate is quite difficult to remove during the work-up, so we opted for the use of an excess of diester. Seeing that the diester is obtained through an expensive procedure, we tried to use the minimum possible excess. The optimal carbamate/diester millimolar ratio was found to be 1:1.5.
- Inorganic salts: as for the second step of the first synthetic approach (see chapter 3.1.1) we used Cs_2CO_3 to deprotonate the phenolic -OH in the diester and NaI to exchange the Br atom of the carbamate with a I atom, which is a better leaving group. The presence of those salts although requires numerous aqueous washings during the work-up, so we tried to use the smaller possible quantity of those reagents. For the definitive procedure we opted for 1.5 equivalents of each salt.

For the final step (base-catalysed hydrolysis), the critical parameter we had to determine was the reaction time. The main issue is that if the reaction is carried on for too long, the carbamate chain hydrolyses as well as the ester groups, and part of the desired product is converted in 5'-(2-aminoethoxy)-[1,1':3',1''-terphenyl]-4,4''-dicarboxylic acid via the hydrolysis of the N-C(O) bond in the carbamate chain resulting in a pendant amine group (Fig. 3.1).

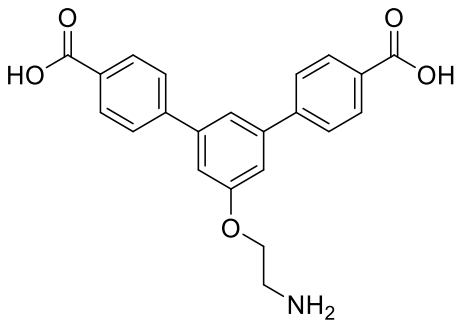

Fig. 3.1: structure of 5'-(2-aminoethoxy)-[1,1':3',1''-terphenyl]-4,4''-dicarboxylic acid.

Indeed, if the reaction is carried for 24 h, after the work-up we found that the aqueous washings contained both the desired product and the amine product. This is particular evident from the ^{1}H-NMR spectra (Fig. 3.2), where is clearly visible the presence of two distinct sets of signals in the aromatic phase. The nature of the by-product is confirmed by the ESI-MR spectrum (Fig. 3.3) where we observe the presence of a signal at 378 *m/z* corresponding to the mass of 5'-(2-aminoethoxy)-[1,1':3',1''-terphenyl]-4,4''-dicarboxylic acid. We found that the optimal reaction time to obtain a satisfying yield and to keep the amine formation at minimum was around 12 hours (generally the reaction was carried overnight).

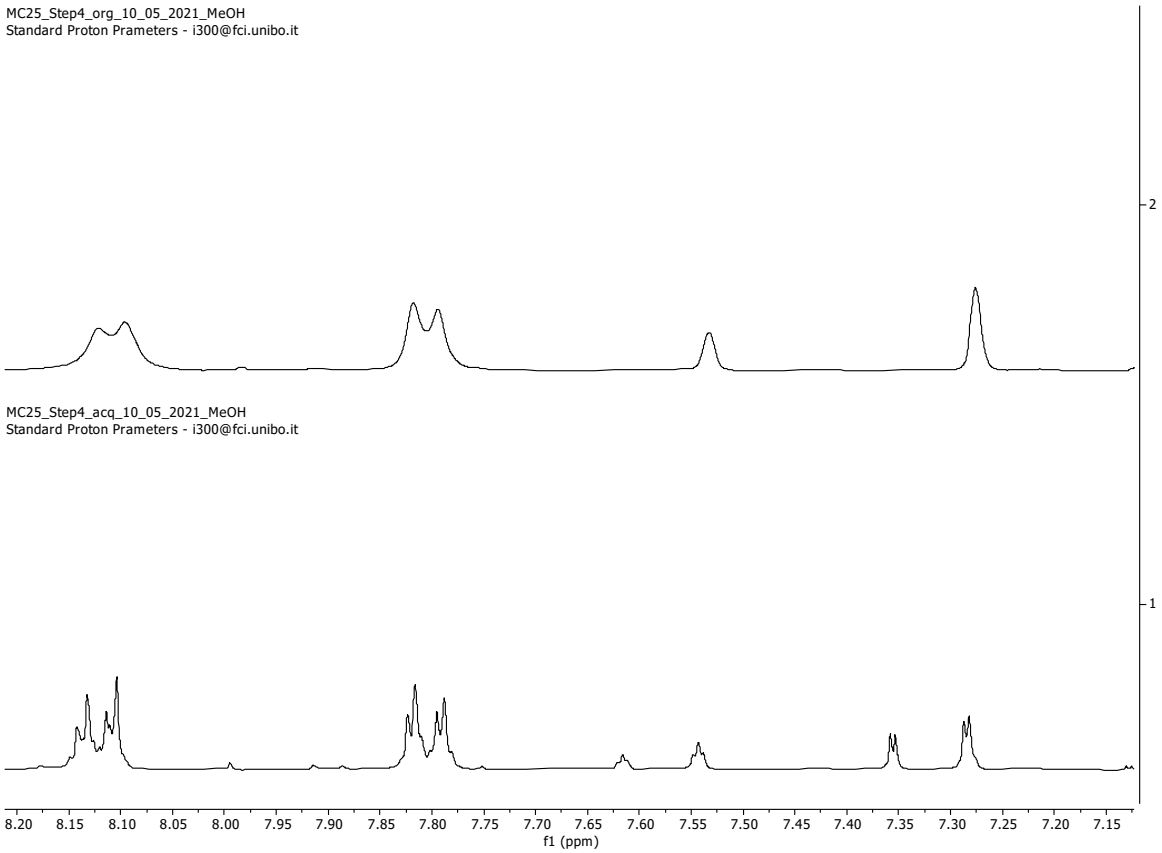

Fig. 3.2: ^{1}H-NMR spectra of the organic phase (top) and the aqueous phase (bottom) after the work-up of the final step carried for 24 hours. The zoom on the aromatic zone of the spectrum shows that in the aqueous phase there are two distinct sets of signals, belonging to the desired product and the amine product.

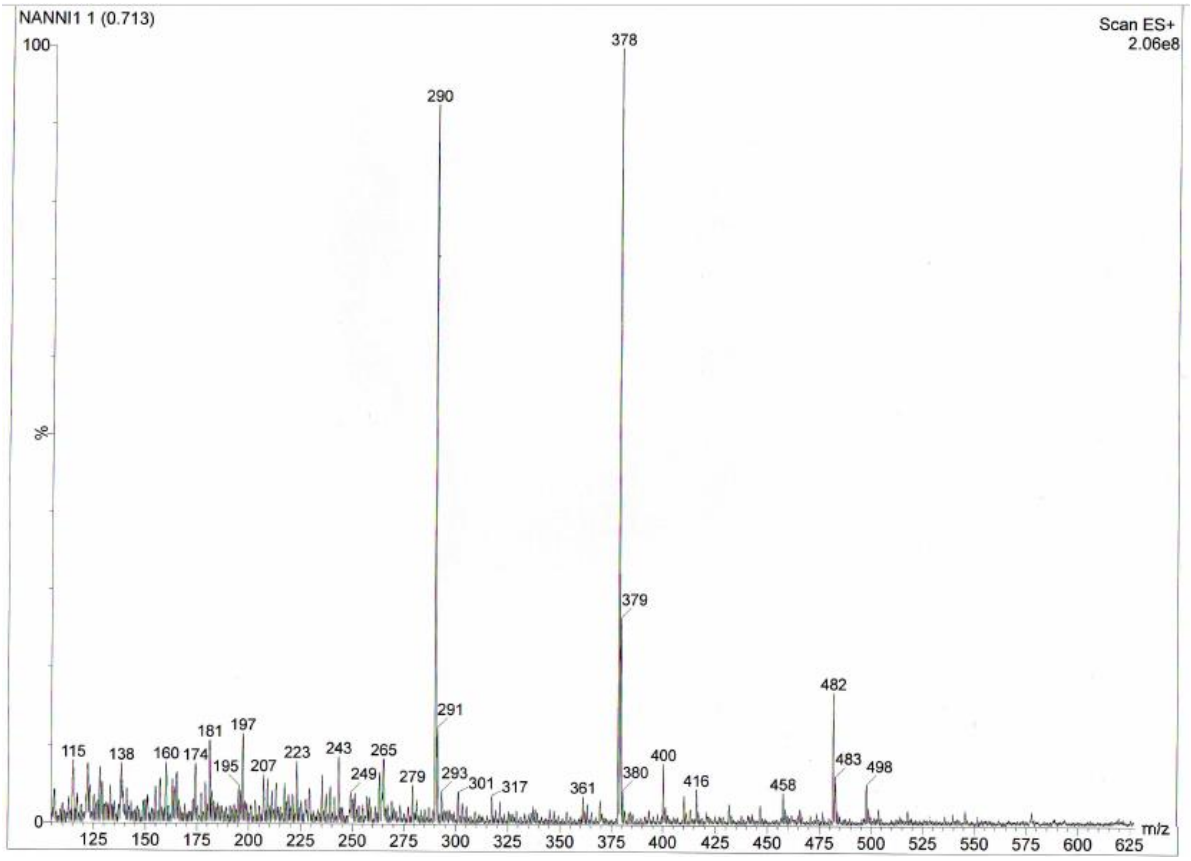

Fig. 3.3: ESI-MS(+) of the aqueous phase (bottom) after the work-up of the final step carried for 24 hours. Both the signal of the desired product (482 *m/z*, $C_{26}H_{21}NO_7Na^+$) and the amine product (378 *m/z*, $C_{22}H_{20}NO_6^+$).

The TGA analysis of the ligand (Fig. 3.4) shows four weight losses. The first three are attributed to the decomposition of the propargyl-carbamate groups (obs. 32.45% (7.322+12.077+13.051), calc. for $C_6H_8NO_3$, mw 142,13 g mol^{-1}, 30.94%). At 800 °C there is a 5% residual, probably consisting in LiCl from the last reaction step.

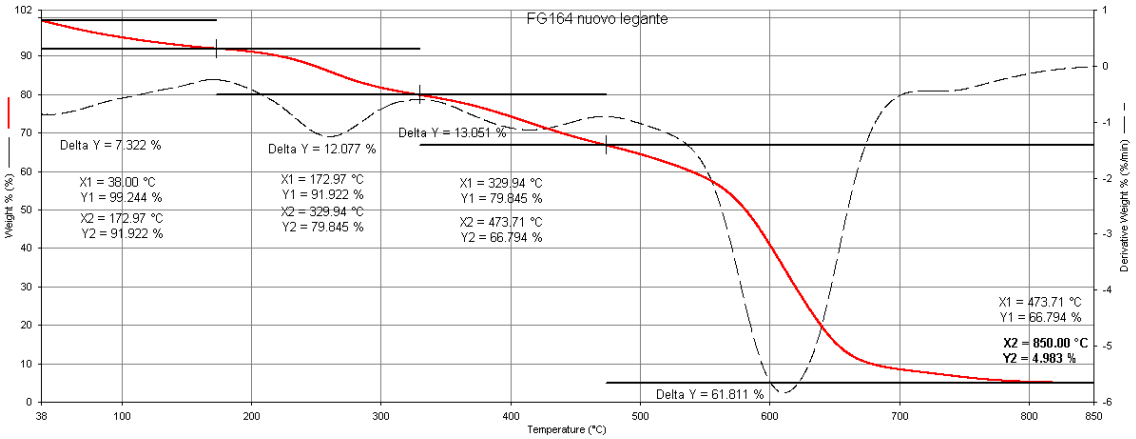

1st loss (%)	2nd loss (%)	3rd loss (%)	4th loss (%)	Residual 800°C (%)
7.3	12.1	13.1	61.8	5.0

Fig. 3.4: TGA curve (continuous red line) and first derivative (dashed line) of the weight loss of H_2YL80.

The presence of LiCl in the ligand could lead to the formation of $Cu(OH)_2$ and/or $CuCl_2$ during the synthesis of the new MOF, therefore we tried to purify the ligand through crystallisation (see chapter 2.3 for the procedure). In Table 3.1 we reported the yields for every crystallisation cycle and the solid residual at 800 °C checked with TGA analysis.

Table 3.1: Yields (%) and inorganic residual at 800 °C of the purified H_2L80

Crystallisation	**Yield (%)**	**Residual at 800 °C (%)**
1st	84	4.3
2nd	22	3.9

The results show that the first crystallisation, although having high yields, only reduces the inorganic residuals of 0.7 percentage points (Fig. 3.5). Considering that the instrument uncertainty is about 1% it is a negligible result.

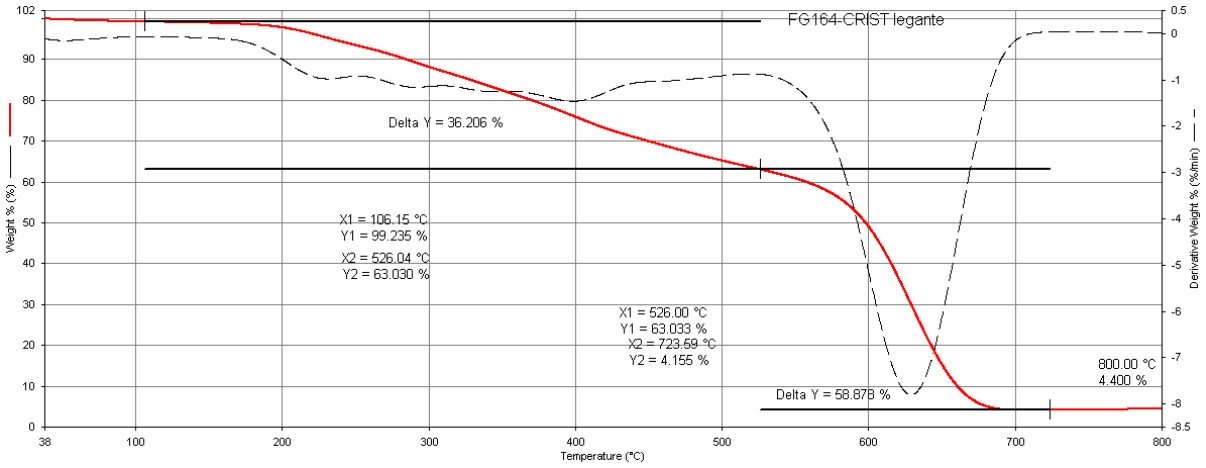

1st loss (%)	2nd loss (%)	Residual 800°C (%)
36.2	58.88	4.4

Fig. 3.5: TGA curve (continuous red line) and first derivative (dashed line) of the weight loss of H_2YL80 after the first crystallisation.

The second crystallisation gives slightly better results in terms of inorganic residual at 800 °C, reducing it at 3.9% (Fig. 3.6), but the yield is decreased by almost four times (22%).

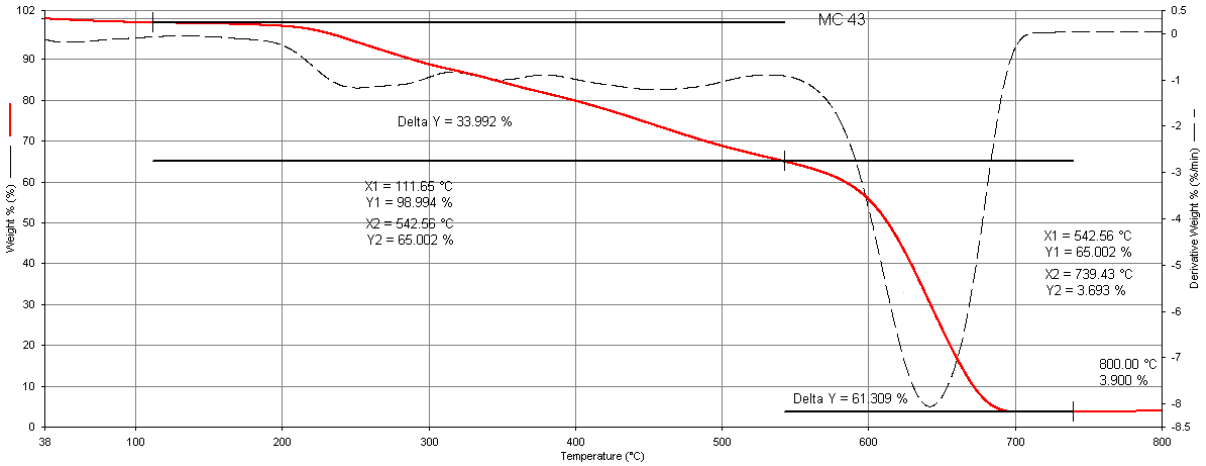

1st loss (%)	2nd loss (%)	Residual 800°C (%)
34.0	61.31	3.0

Fig. 3.6: TGA curve (continuous red line) and first derivative (dashed line) of the weight loss of H_2YL80 after the second crystallisation.

Those results brought to the conclusion that, seeing the long and complex process needed to synthesise H_2YL80, the material loss caused by the purification process is too high compared to the small removal of inorganic impurities. Therefore, for the synthesis of the new MOF, the ligand was used without any purification.

3.2 New Cu-MOF Synthesis

The new organic ligand H_2YL80 was used to attempt the synthesis of a new Cu-based MOF. As for the synthesis of [Cu(1,3-YBDC)]·$x$$H_2O$, the copper salt the organic ligand is reacted with $Cu(NO_3)_2 \cdot 2.5H_2O$. Ideally, this new MOF should be structurally similar to [Cu(1,3-YBDC)]·$x$$H_2O$, but hopefully, the larger organic moiety of the organic ligand will prevent the extra coordination of the carbonylic oxygen of the propargyl-carbamate chain to the apical positions of the paddlewheel unit (see chapter 1.1). The characterisation of MOFs is typically accomplished through X-ray spectroscopy techniques. In order to successfully perform those measurements, it is necessary to obtain the material in a crystalline form. It follows that the reaction conditions have to be carefully chosen, so we attempted numerous synthesis processes, each modifying different reaction parameters (Metal:Ligand ratio, reagents concentration, solvents, temperature, stirring, atmosphere, reaction time). In table 3.2 are reported the reaction conditions used in the different attempts.

Table 3.2: Reaction conditions for the different attempts for the new MOF synthesis.

Reaction	M:L; Ligand concentration	DMF:H_2O: 2-propanol	T/°C	Stirring	Atm.	Time /h	Results
MC35	1.8:1 0.026 M	0:0:1	85	Yes	Air	24	Amorphous solid (green). 70% yield.
MC44	2:1 0.016 M	3:1:0	80	Yes	Air	24	Amorphous solid (green), presence of Cu-oxides. 78.4% yield.
MC45	2:1 0.016 M	3:1:0	r.t (starting) 50 (after 24 h)	Yes	Air	48	At r.t the reaction does not happen, so the temperature is increased after 24 hours. The final product is an amorphous green solid; when washed with water the precipitation of a white inorganic residue is observed (contains traces of the ligand).
MC46	2:1 0.016 M	3:1:0	50	No	Air	168	Green solid mixed with traces of white solid; higher crystallinity compared to MC44 (polycrystalline). 46% yield.
MC49	2:1 0.016 M	1:9:0 (starting) *After 48 hours DMF is added, the new rate becomes* 1:1:0	50 (starting) 80 (after 48 h)	No	N_2	168	With the starting solvent composition, the ligand is not completely soluble. After 120 h at 80°C the product is decomposed (mostly brown Cu-oxides).
MC50	2:1 0.016 M	1:0:0	50 (starting) 80 (after 48 h)	No	N_2	168	After 48 h at 50 °C no solid is formed. After 120 h at 80°C the product is decomposed (mostly brown Cu-oxides).

Reaction	M:L; Ligand concentration	DMF:H_2O: 2-propanol	T/°C	Stirring	Atm.	Time /h	Results
MC51	2:1 0.016 M	4:1:0	50	No	N_2	168	Polycrystalline green solid. 70% yield.
MC52	2:1 0.016 M	2:1:1	50	No	N_2	168	Polycrystalline green solid. 61% yield.
MC53	2:1 0.008 M	4:1:0	50	No	N_2	168	Polycrystalline green solid. 30.5% yield.

The choice of the solvents is one of the most delicate points. The combination of solvents in different ratios not only determines the solubility of the reagents, but it also influences the rate of the various reaction mechanisms, and therefore the characteristics of the final product (Fig. 3.7). For example, if the organic ligand has a low solubility in water, the use of a high rate of water in the solvent combination leads to a slow ligand dissolution, making it the rate-determining step in the crystallisation process.[71] It is often observed that the use of high ratios of water and/or alcohols leads to the formation of larger crystals but with generally low yields, while on the other hand the use of organic solvents such as DMF increases the solubility of the organic ligands and consequentially the nucleation rate.[72]

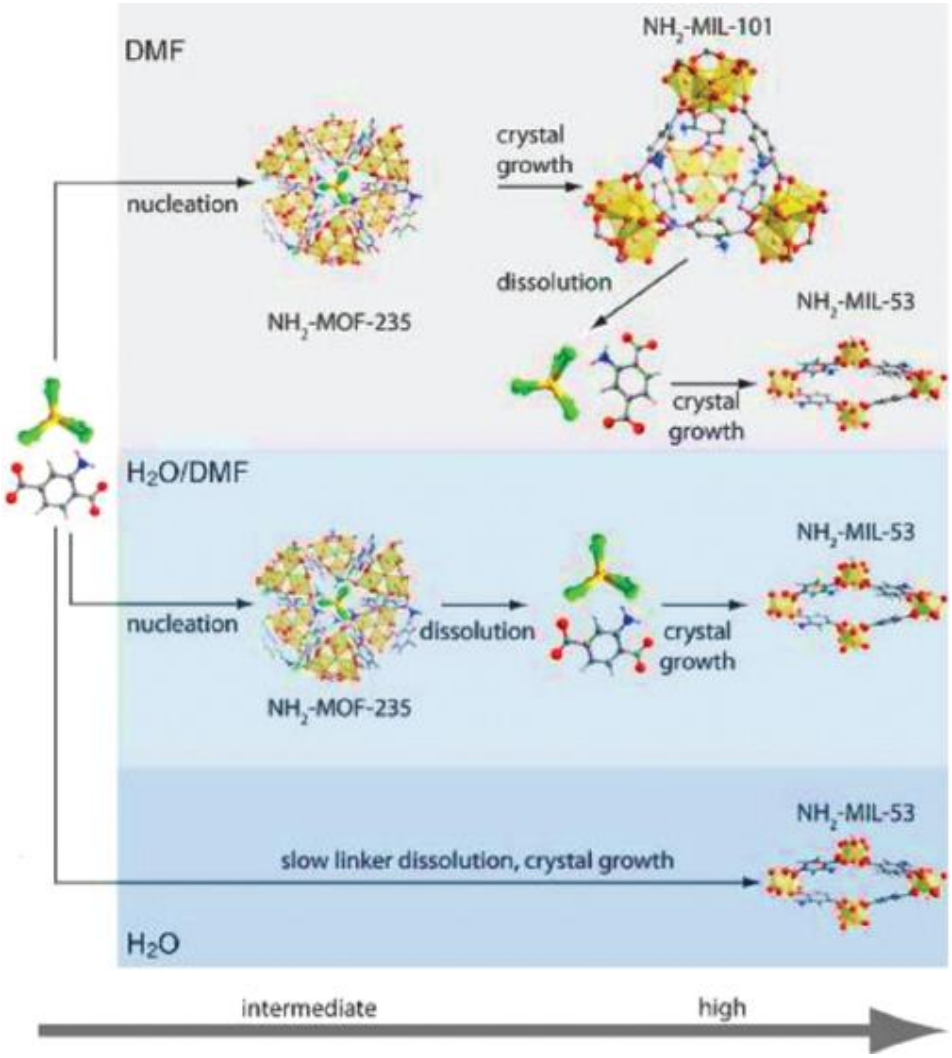

Fig. 3.7: Sequence of events taking place during the NH_2-MIL-53(Al) and NH_2-MIL-101(Al) crystallization processes under different synthesis conditions. C: grey, H: white, N: blue, O: red, Al: yellow, Cl: green.[71]

Due to the similarity of the reagents used, in the first attempt of the synthesis of the new Cu-MOF the we employed the same conditions of the synthesis of [Cu(1,3-YBDC)]·$x$$H_2O$[5] (see MC35 in Table 3.2). In these conditions the reagents reacted fast, yielding a light-green solid, but the XRD analysis on the product showed that the solid was almost completely amorphous (Fig 3.8).

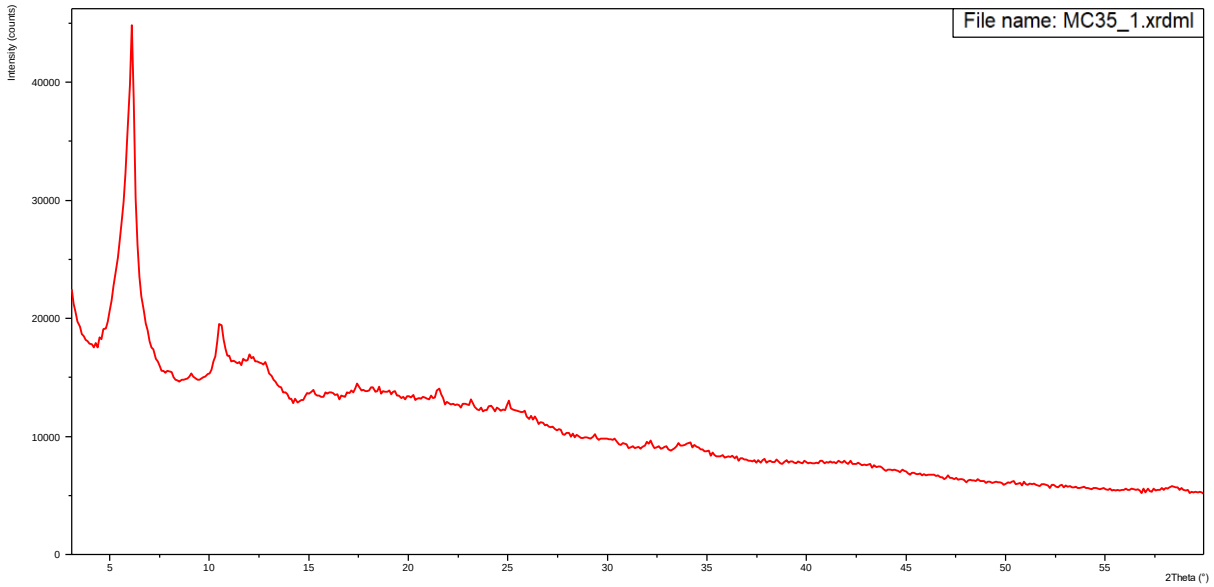

Fig. 3.8: XRD analysis of the product of MC35, showing the almost completely amorphous nature of the material.

The FTIR spectrum of the product was compared to the one of the neat ligand (Fig 3.9). The comparison highlighted the loss of the carboxylic acid protons of the ligand. This, together with some other difference in the spectrum area below 2000 cm^{-1}, showed that H_2YL80 effectively coordinated the Cu ions. Having verified that the ligand and the copper salt react successfully with each other, the successive attempts were aimed to the research of the optimal conditions to increase the crystallinity of the final product.

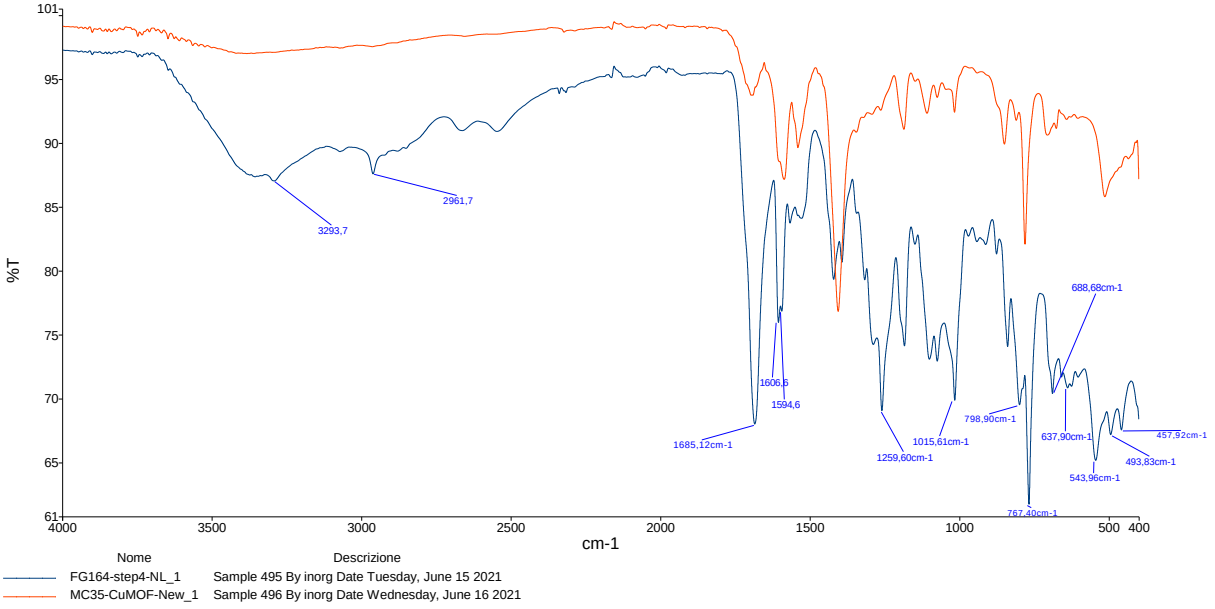

Fig. 3.9: Comparison between the FTIR spectra of H_2YL80 (blue line) and the product of MC35 (red line), showing the disappearance of the carboxylic O-H peaks at 3294 cm^{-1}. The differences in the region below 2000 cm^{-1} could be attributed to the formation of Cu-O bonds.

Different solvent compositions were tried, modifying the DMF:H_2O:2-propanol ratio. 2-propanol was chosen instead of the more common ethanol[72] because during the synthesis of [Cu(1,3-YBDC)]·$x$$H_2O$ it was found that the presence of ethanol could lead to the esterification of the ligand.[5] The experiments led to the conclusion that for the new Cu-MOF synthesis, the presence of at least a 50% of DMF in the solvent composition is necessary to dissolute effectively the organic ligand, but also that the presence of H_2O and/or 2-propanol is mandatory to have the correct precipitation of the final product (see MC50 in Table 3.2).

The choice of the temperature was made in order to avoid the decomposition of the reagents and the formation of copper oxides. The optimal temperature was found to be 50 °C. Higher temperatures led to the formation of Cu-oxides in almost all cases, while at room temperature the reaction does not take place (see MC45 in table 3.2). By keeping the temperature at 50 °C we were able to avoid the decomposition even for long reaction times (one week), and, at the same time, to have acceptable reaction rates (formation of the first crystals within the first 24-30 hours).

The first four syntheses (MC35, MC44, MC45 and MC46 in table 3.2) were carried in air atmosphere, then for the following ones we switched to N_2 atmosphere, hoping that it could prevent the decomposition of the reagents and the consequent formation of copper oxides. Unfortunately, it appears that even with the inert atmosphere, at high temperatures (80 °C) the decomposition occurs anyway (see MC49 and MC50 in table 3.2). On the other hand, none of the reactions carried in N_2 showed the formation of the white inorganic residue that has been observed in MC45 and MC46 (see Table 3.2), but it is not clear if this phenomenon is related to the atmosphere.

The first three syntheses (MC35, MC44, and MC45 in table 3.2) were carried under magnetic stirring. After those unsuccessful attempts, the magnetic stirring was not employed for the following reactions, to see if keeping the system still could help to slow down the nucleation and give a more crystalline product. Apparently, this precaution seems effective, seeing that the products that were obtained without magnetic stirring showed higher crystallinity (polycrystalline materials) compared to the previous ones (see MC46, MC51 and MC52 in Table 3.2 and the relative XRD spectra in Fig. 3.10).

The last parameter that was taken into account is the concentration of the reagents. For the first reaction (MC35), a concentration of 0.026 M for the ligand and 0.046 M for the copper salt were employed. For the following reactions up to MC52, the concentration of the ligand was lowered to 0.016 M and to 0.031 M for the copper salt. After the encouraging results obtained with the reaction MC51, we decided to repeat the reaction in the same conditions but

halving the concentration of the reagents (see MC53 in table 3.2). This way, we hoped to slow down the nucleation process, allowing an easier crystallisation of the product. We confirmed that the formation of the solid was actually slower compared to MC51 (the first formation of the solid was only observed after 96 hours). Unfortunately, the product of MC53 was also polycrystalline (Fig. 3.11), plus the yield was exactly half compared to MC51, so it is far from a satisfying result.

Comparing the XRD spectra of the products of MC51, MC52 and MC53 (Fig. 3.12), it appears that the crystalline phases are slightly different in each case. In MC51 we observe the presence of two main crystalline phases, one predominant at $2\theta = 5.25°$ and the other at $2\theta = 5.58°$. In MC52 we observe the same two phases but this time they are present in an almost equal proportion. In MC53 we have the disappearance of the phase at $2\theta = 5.25°$, but a new phase at $2\theta = 6.40°$ appears, in lower proportion compared to the one at $2\theta = 5.58°$.

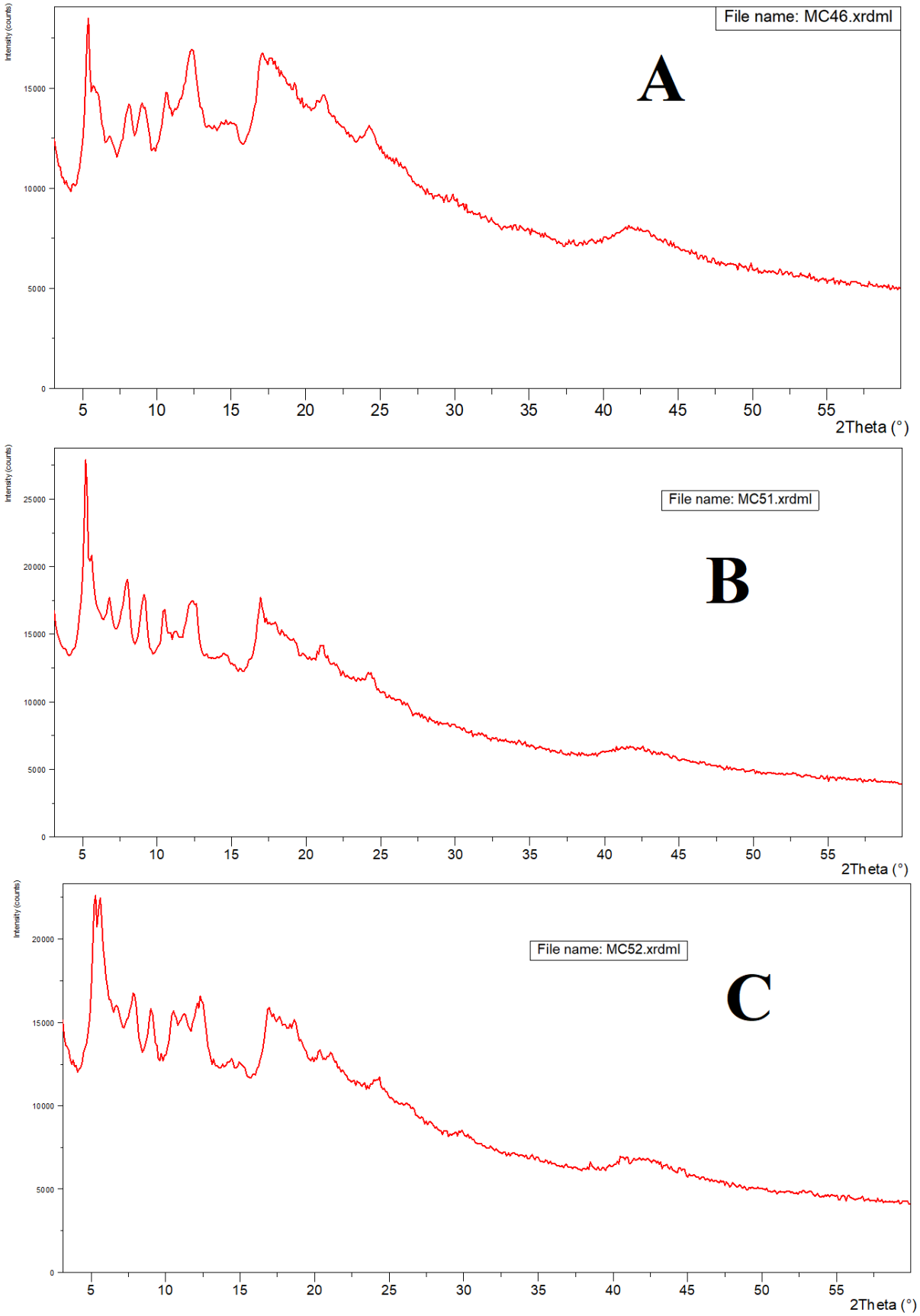

Fig. 3.10: XRD spectra of the products of the reactions MC46 (panel A), MC51 (panel B) and MC51 (panel C). The materials show higher crystallinities compared to MC35 (see Fig. 3.8).

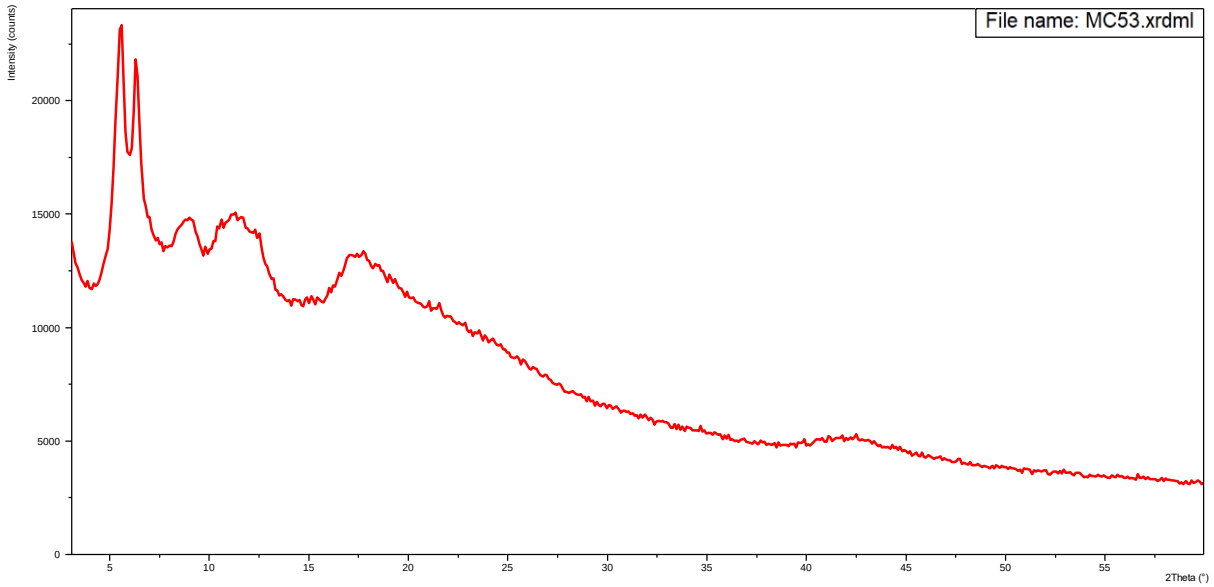

Fig. 3.11: XRD spectrum of the product of the reaction MC53.

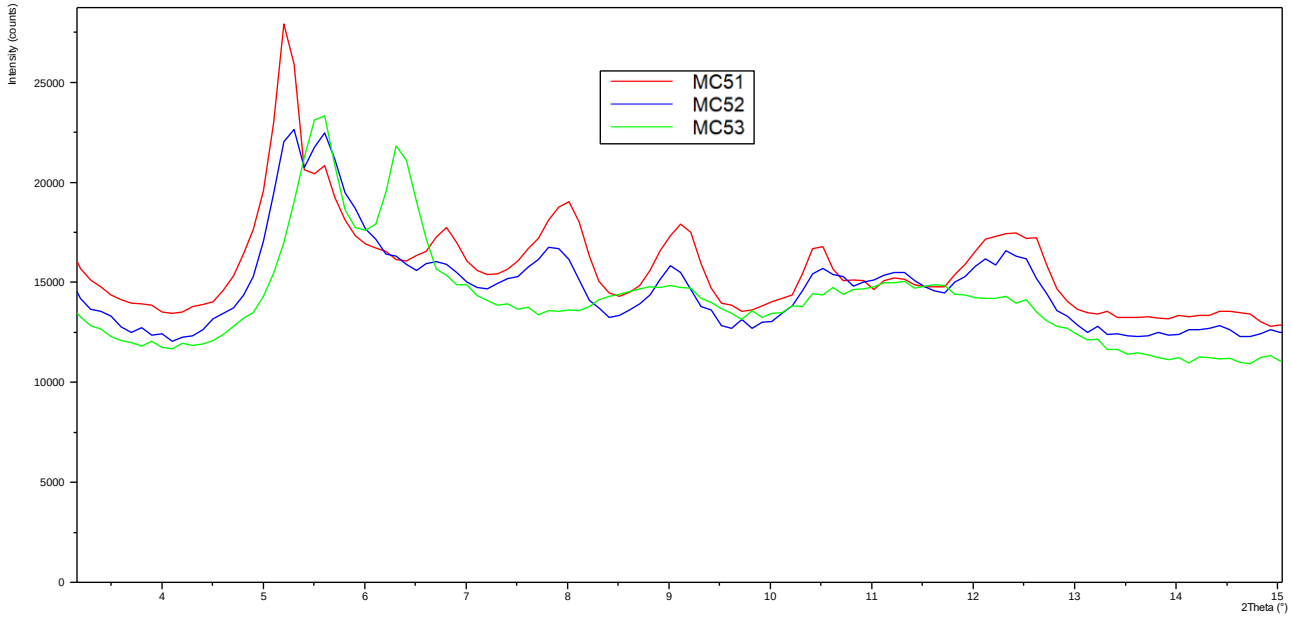

Fig. 3.12: Comparison of the XRD spectra of the products of reactions MC52 (red line), MC52 (blue line) and MC53 (green line).

Chapter 4

4 Reactivity of [Cu(1,3-YBDC)]·xH$_2$O towards HAuCl$_4$

[Cu(1,3-YBDC)]·*x*H$_2$O, hereafter simply termed Cu-YBDC, was first stirred in a 1.0 mM solution of HAuCl$_4$ at room temperature for 1 h in methanol under N$_2$, then the not adsorbed HAuCl$_4$ was separated by centrifugation and the MOF thoroughly washed with methanol. Afterwards, the resulting material was placed in a solvent under reflux to promote the reduction of the adsorbed Au(III). In this way only the Au(III) truly adsorbed inside the MOF is reduced (Scheme 4.1).

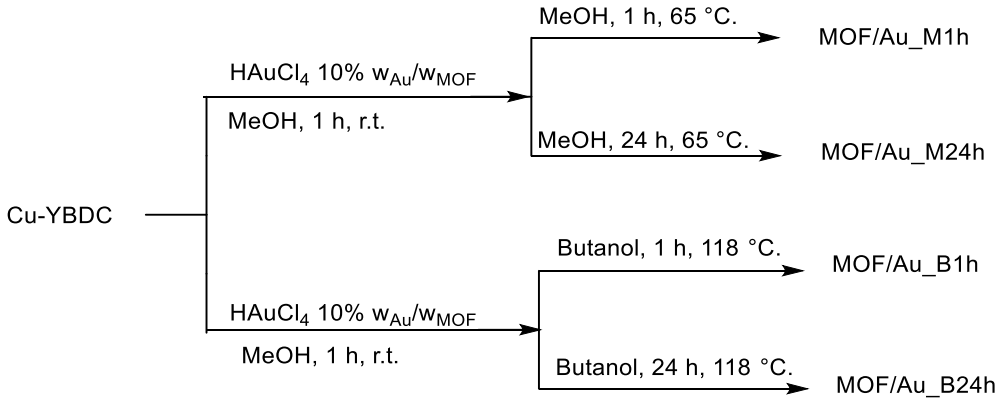

Scheme 4.1: [Cu(1,3-YBDC)]·xH$_2$O reactions with HAuCl$_4$.

The samples labelled MOF/Au_M1h (FG130a) and MOF/Au_M24h (FG130b), MOF/Au_B1h (FG131a), MOF/Au_B24h (FG131b), were analysed by AAS to determine the total amount of gold (Table 4.1).

Table 4.1: Gold content in samples MOF/Au_M1h, MOF/Au_M24h, MOF/Au_B1h, MOF/Au_B24h.

Sample	Weight of the sample (mg)	Abs	Au concentration (ppm)	%Au w/w
MOF/Au_M1h	10.5	0.018	0.62	0.29
MOF/Au_M24h	10.0	0.019	0.65	0.33
MOF/Au_B1h	9.9	0.011	0.35	0.18
MOF/Au_B24h	9.9	0.011	0.35	0.18

There is no significant distinction between the amount of gold in MOF/Au_M1h and MOF/Au_M24h. The same is also true for MOF/Au_B1h and MOF/Au_B24h. This means that the gold retained by the MOF does not leach out in 24 hours, indicating a strong interaction between the MOF surface and gold.

XPS studies were carried out on the four samples in order to gather information on the elemental composition and oxidation states characterizing the elements present on the surface of the investigated materials.

All the four samples (*i.e.*, **FG130a**, **FG130b**, **FG131a**, and **FG131b**) revealed the presence of C, N, O, Cu, and Au atoms on their surface, in agreement with the composition expected for the Au-supported MOF compounds (Fig. 4.1).

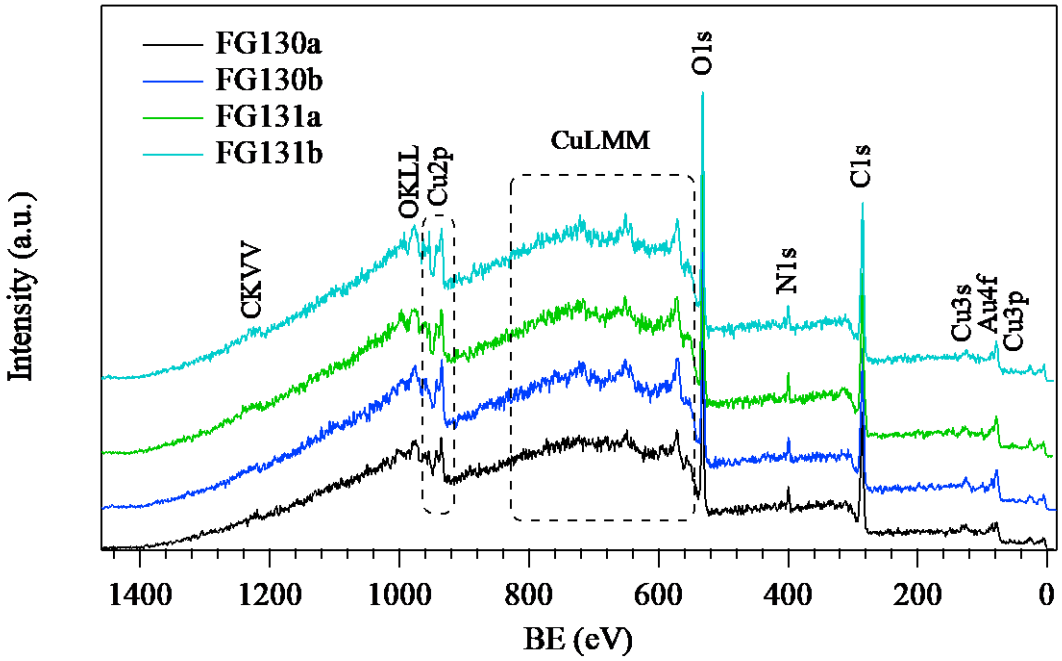

Fig. 4.1: Surface XPS wide-scan spectra for all the target specimens.

Results of the surface quantification are summarized in Table 4.2. All the samples exhibit a similar C, N and O content. In the case of metals, **FG130a** and **FG130b** samples revealed a Cu content of *ca.* 2.0 at.%, whereas for **FG131a** and **FG131b** compounds it is *ca.* 1.4 at.%. On the other hand, the Au concentration, which is comprised between 0.12 and 0.06 at.%, decreases in the order **FG130a** > **FG130b** = **FG131a** > **FG131b**.

Table 4.2: Relative composition of the target specimen analyzed by XPS.

sample	at.% values					
	C	**N**	**O**	**Cu**	**Au**	**Au/Cu**
FG130a	62.76	4.14	31.00	1.97	0.12	0.06
FG130b	62.25	4.72	30.81	2.15	0.08	0.04
FG131a	66.42	3.86	28.27	1.36	0.08	0.06
FG131b	66.57	3.28	28.69	1.41	0.06	0.03

High-resolution spectra of C1s signal reveal the presence of four different components (see Fig. 4.2 a), which concurrently contribute to this peak and which can be assigned to the MOF scaffold. In detail, C1s signal is the result of the following features: (**I**) BE = 284.8 eV (relative abundance ≈ 42 % of the total C signal), attributed to both adventitious carbon contaminations and to C-C species; (**II**) BE = 286.0 eV (relative abundance ≈ 30 % of the total C), assigned to C-N and C-O bonds in the ligand skeleton; (**III**) BE = 287.8 eV (relative abundance ≈ 20 % of the total C signal), related to the -COOH functionalities bonded to the aromatic ring; and (**IV**) BE = 289.8 eV (relative abundance ≈ 8 % of the total C signal), assigned to -NCOO- groups present in the ligand lateral chain.[73–75] Three different peaks are concurring to the overall intensity of the O1s signal (see Fig. 4.2 b), which are: (**V**) BE = 529.8 eV (relative abundance ≈ 7 % of the total O signal), associated to ligand oxygen atoms bonded to copper[73] and/or O in copper oxides[76,77] (**VI**) BE = 531.5 eV (relative abundance ≈ 45 % of the total O signal), ascribed to C-O single bonds and chemisorbed OH hydroxyl groups;[74,78,79] and (**VII**) BE = 533.2 eV (relative abundance ≈ 48 % of the total O signal), attributed to the presence of C=O groups in carboxylate functionalities and/or adsorbed water molecules.[74,75] A single peak signal is determined in the N1s spectra (see Fig. 4.2 c), centered at BE = 400.6 eV. This binding energy value indicates that a strong ligand coordination is present between nitrogen atoms and Cu(II) metal centers in the investigated materials.[80]

Important information on the Cu chemical state can be gained by means of a careful evaluation of the copper signals (see Fig. 4.2 d-e). Indeed, the calculation of the Auger parameter, which is defined as α_{Cu} = BE(Cu2p$_{3/2}$) + KE(CuLMM)[66] (where KE = kinetic energy = 1486.6 - BE), is a useful tool in order to determine the presence of Cu(I) and/or Cu(II) into the investigated materials. In our case, α_{Cu} = 1850.8±0.2 eV, close to the value obtained for pure CuO,[76,77] thus witnessing that the majority of copper species are in their divalent oxidation state. Indeed, the signal of both Cu2p$_{3/2}$ and Cu2p$_{1/2}$ peaks can be fitted with just one

component. In particular, values of BE = 934.6 and 954.3 eV for $Cu2p_{3/2}$ and $Cu2p_{1/2}$ spin-orbit components, respectively, are obtained. These BEs are in agreement with the presence of Cu(II) species into the copper-containing metal-organic framework.[73,79,81] A further confirmation of this attribution is given by the presence of intense *shake-up* satellites peaking at BE values ≈ 9.5 eV higher than the main spin-orbit components, which are a finger-print for the predominant presence of d^9 copper (II) centers.[77,82,83] When only Cu(I) species (d^{10}, a closed-shell system) are present, such satellites are not detected.

A low intensity and broad Au4f signal is detected at its typical BE values (see Fig. 4.2 f). The broadening of the peak suggests the presence of Au species with different oxidation states. In particular, it is possible to recognize the presence of: (**VIII**) BE($Au4f_{7/2}$) = 84.0 eV and BE($Au4f_{5/2}$) = 87.8 eV (relative abundance ≈ 23 % of the total Au4f signal), ascribed to Au(0) species; and (**IX**) BE($Au4f_{7/2}$) = 85.8 eV and BE($Au4f_{5/2}$) = 89.6 eV (relative abundance ≈ 77 % of the total Au4f signal), attributed to oxidized Au(I) species.[66,74,75] In particular, the most oxidized gold species are found, in order, in: (i) **FG131b** (81.4 at.% of Au(I)); (ii) **FG131a** (78.7 at.% of Au(I)); (iii) **FG130b** (75.8 at.% of Au(I)); and (iv) **FG130a** (71.9 at.% of Au(I)). In these samples, the Au4f BEs characterizing metallic gold (*i.e.*, peak **VIII**) are in agreement with the typical reference position of Au(0) (*i.e.*, 84.0 eV).[74,84]

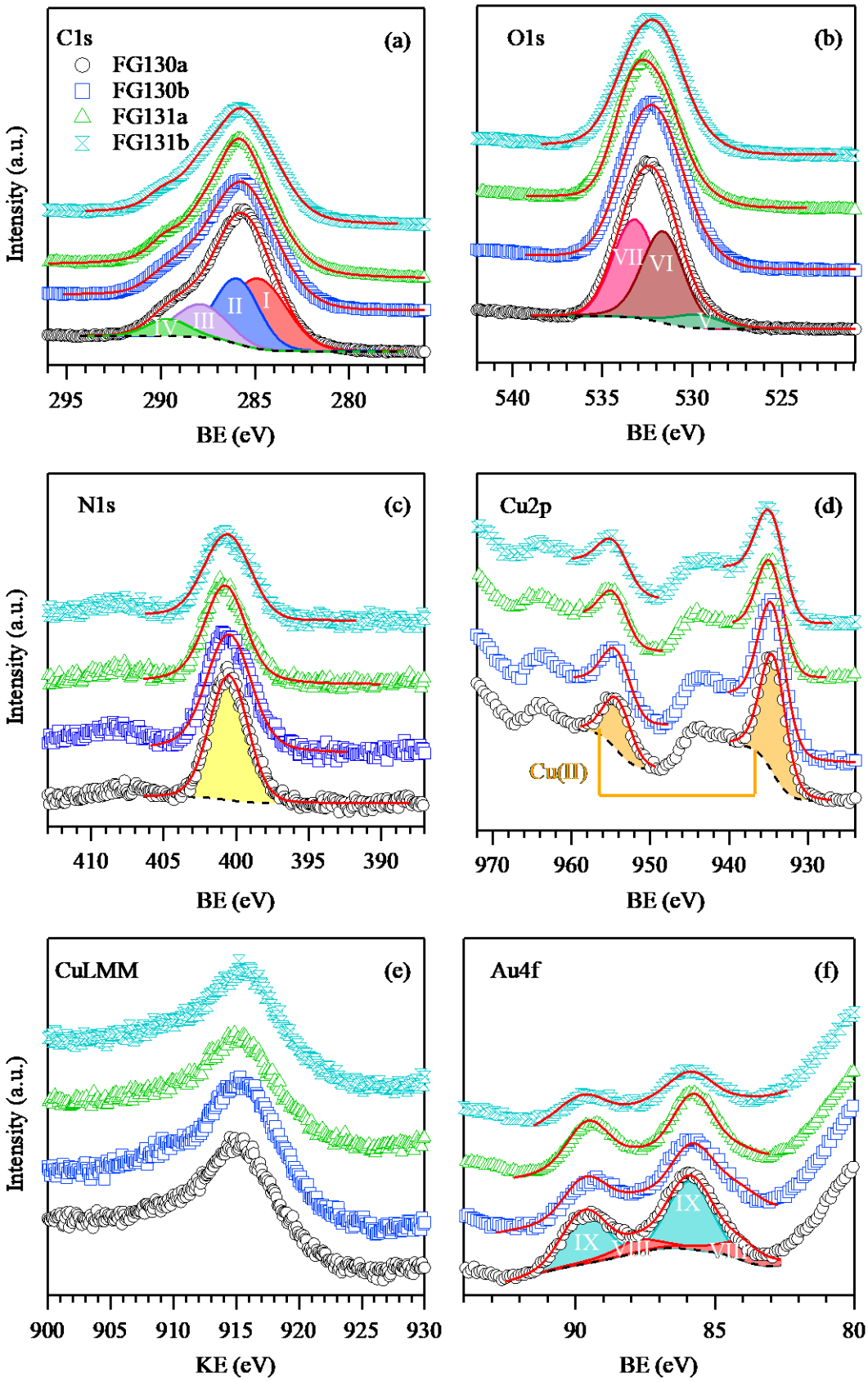

Fig. 4.2: Surface XPS analysis for the target specimen: (a) C1s, (b) O1s, (c) N1s, (d) Cu2p, (e) CuLMM, (f) Au4f. The red curve represents the fitting results.

In view of the AAS and XPS results discussed above, only the sample FG130a (MeOH, 1h, 65°C) was further fully characterized and the resulting data compared with the starting Cu-YBDC. In Fig. 4.3 the TGA plot for Cu-YBDC (of $C_{14}H_{11}CuNO_7$ formula, mw 368.79 g mol^{-1}) shows two decomposition steps in the 200-450 °C range (attributed to the progressive loss of the propargyl fragments $C_6H_8NO_3$ residue, obs. 38.2%, calc. 38.5%), terminating at a temperature ca. 150 °C lower than in the pristine organic ligand.[5] Such lower thermal stability of the organic skeleton within the MOF is tentatively attributed to assistance, during decomposition, of redox process(es) catalyzed by Cu(II) ions. Furthermore, a residue of ≈ 26 wt% is present at 400 °C, with no significant variation up to 800 °C, which is presumably due to residual CuO. As a residual 21.6% only is calculated if the starting material were pure, the excess residue at high T speaks for the presence of carbonaceous residuals and only marginally to Cu-rich contaminants.

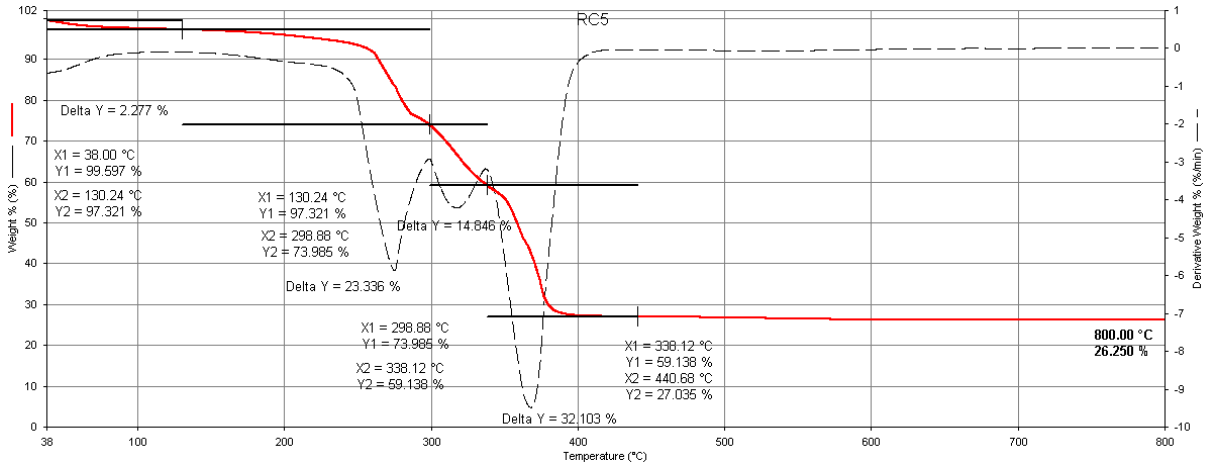

Fig. 4.3: TGA curve (continuous red lines) and their first derivatives (dashed lines) for Cu-YBDC.

In Fig. 4.4 the TGA plot for the Au(I)-containing Cu-MOF (FG130a, MeOH 1h, 65 °C) is shown. Also in this case the two decomposition steps occur in the range 200-450 °C range with a final residue of ≈ 30 wt% i.e. a 4 wt% higher than in the absence of gold.

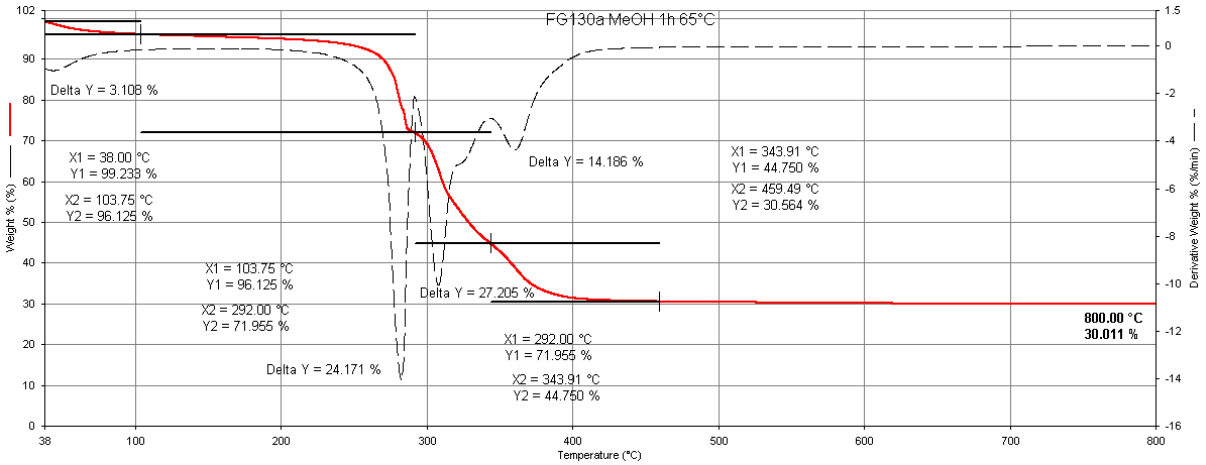

Fig. 4.4: TGA curve (continuous red lines) and their first derivatives (dashed lines) for the Au(I) containing Cu-MOF FG130a (MeOH 1h, 65 °C).

The XRD patterns of Cu-YBDC (RC5) and Cu-MOF/Au(I) (FG130a, MeOH 1h, 65 °C) are compared in Fig. 4.5. The two patterns are identical except for the fact that in Cu-MOF/Au(I) the peak at 12.82° (indicated by the green arrow), attributed to the $Cu_2(OH)_3(NO_3)$ contaminant species, is more intense.

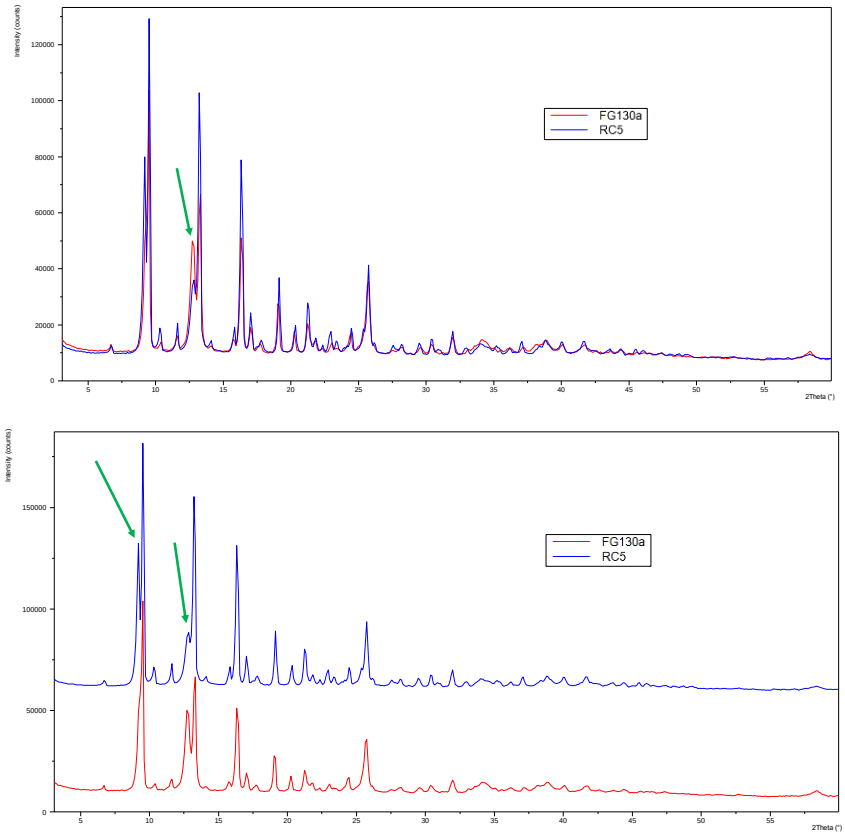

Fig. 4.5: Full plot of diffraction for samples [Cu(1,3-YBDC)]·xH$_2$O (RC5) and Cu-MOF/Au(I) (FG130a, MeOH 1h, 65 °C).

In Figure 4.6 the ATR-IR spectra of Cu-YBDC (FG74, red line) and Cu-MOF/Au(I) (FG130a, MeOH 1h, 65 °C, black line) are shown.

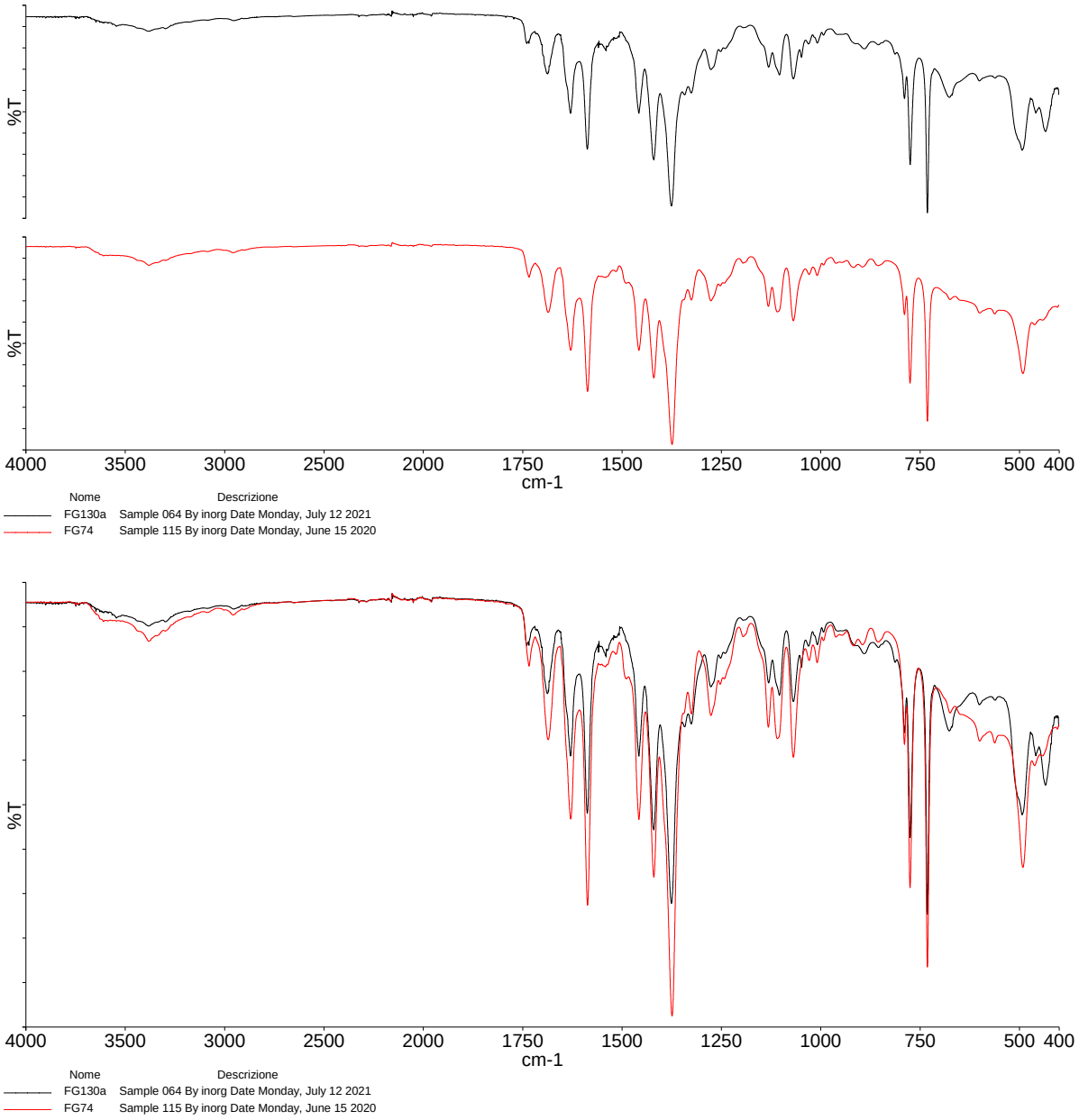

Fig. 4.6: IR-ATR spectrum of Cu-YBDC (FG74, red line) and Cu-MOF/Au(I) (FG130a, MeOH 1h, 65 °C, black line).

The morphology of the powder was imaged by means of FE-SEM. In Fig. 4.7 SEM images of Cu-YBDC deposited on an electrode surface[58] after sonication in ethanol and Cu-YBDC/Au(I) are reported. The micrograph for Cu-YBDC (Figure 4.7A) revealed the predominant presence of large prismatic crystals with sub-micrometric dimensions while the

micrograph for Cu-YBDC/Au(I) (Figure 4.7B) still showed the predominant presence of prisms although less defined and smaller of those observed with the sample not treated with $HAuCl_4$.

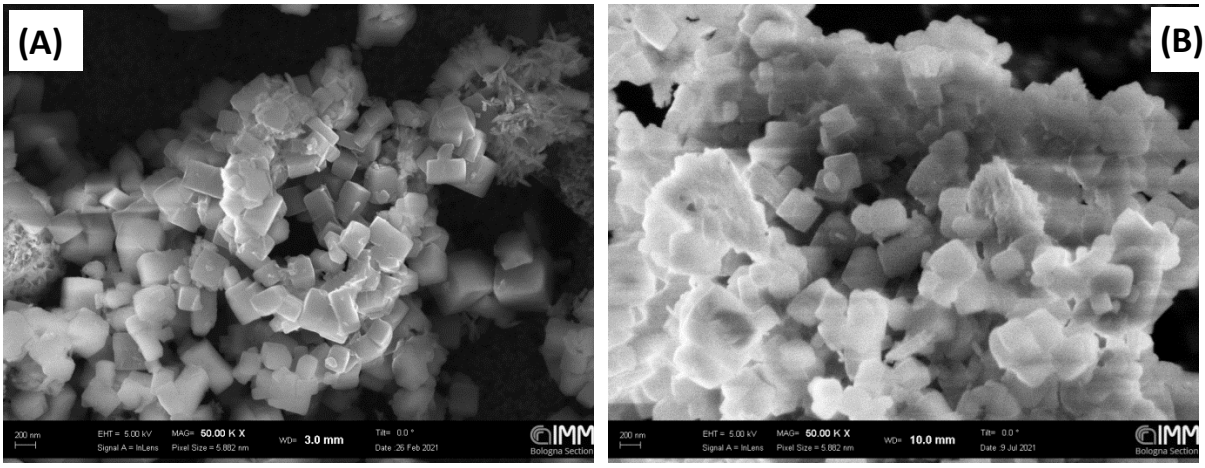

Fig. 4.7 Representative FE-SEM images of Cu-YBDC (A) and Cu-YBDC/Au(I) (FG130a, B).

In conclusion, the thermal treatment in alcohol of Cu-YBDC impregnated with $HAuCl_4$ leads to the reduction of Au(III) to Au(0) and to Au(I), with the latter oxidation state as the predominant oxidation state leaving the morphology of the starting Cu-MOF substantially unchanged.

Chapter 5

5 Cu-YBDC as an adsorbent for Methylene Blue

5.1 Introduction

As stated in Chapter 1.2, one of the objectives of this work is to study the possible uses of the Cu-YBDC MOF as an adsorbent material for dyes. For that purpose, we tested its performances for the adsorption of Methylene Blue (MB). The low porosity and specific surface area of the tested material surely represent a disadvantage when it comes to adsorption efficacy, due to the difficulty that the dye molecules will face entering the pores. In fact, according to the literature, the molecule of MB can be regarded as a rectangular volume of dimensions 17.0 x 6.7 x 3.3 Å,[85] corresponding to a volume of 426.36 $Å^3$ and to an area of 129.2 $Å^2$ (if we discard the thickness and treat the molecule as planar). Considering that the size of the cavities of [Cu(1,3-YBDC)] is only 141 $Å^3$, it is clear that all the adsorption phenomena must take place on the external surface of the MOF. On the other hand, in literature there are already reported cases of MOFs with low surface area and porosity which showed nevertheless high adsorption capacities.[36] The different functional groups present upon the external surface of [Cu(1,3-YBDC)]·$x$$H_2O$ could provide an interesting substrate due to the large amount of different adsorption mechanisms that can take place (hydrogen bonds between the dyes and the -NH- or the C=O group of the carbamate, π-π interactions between the dyes and the aromatic rings, π-π interactions between the dyes and the propargyl group…), so it is worth the try.[31,33]

5.2 State of the art for Methylene Blue (MB) adsorption over MOFs

Methylene Blue (MB) is one of the most used dyes for adsorption studies over MOFs. MB is a cationic dye, extensively used in the dying of cotton, silk and wood,[86] but can also be found in other fields such as pharmaceutical chemistry.[87] It is also considered a hazardous molecule, because of its toxic, carcinogenic and mutagenic effect on human health.[41] For these reasons, there is an increasing interest towards the technologies for the abatement of MB, since some countries are even starting to implement legal limits for the concentration of this pollutant in discharged industrial wastewaters (for example, in China the maximum concentration allowed is 0.2 mg/L).[88] Even in absence of specific legislations for Methylene Blue, the abatement of this molecule and/or of other organic dyes can contribute to contain numerous environmental parameters such as BOD and COD for the waste-waters under the legal values (for example see D. Lgs 152/06, Part Three, Attachment 5, Table 3 for Italian legislation).[89]

Due to its molecular structure (Fig. 5.1), there are many different mechanisms that can take part in the adsorption of MB Over MOFs. First, its cationic nature enhances the electrostatic interactions with anionic and/or electron rich surfaces. The aromatic rings of MB can also interact via π-π stacking, if there are aromatic functional groups or multiple bonds on the surface of the MOF (quite common occurrence). Lastly, the presence of electron lone-pairs upon the N atoms of MB allows the formation of hydrogen bonds with some surfaces.[45]

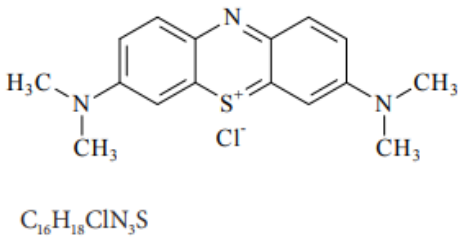

Fig. 5.1: Structure and brute formula of Methylene Blue.[87]

In Table 5.1, we collected a wide range of examples taken from the literature of MOFs used for MB adsorption. For each of them, the performances were studied in terms of adsorption capacity with different kinetic models, specifically the Pseudo-Second Order (PSO), the Pseudo-First Order (PFO), and the Intraparticle Diffusion model (IPD). It is notable that in every example, the PSO model has been found to be the best fit for the experimental data. This collection will be used to compare the performance of the MOF [Cu(1,3-YBDC)] as an adsorbent material for MB.

Table 5.1: Literature kinetic data for Methylene Blue (MB) adsorption over MOFs according to the following adsorption models: Pseudo-Second Order (PSO), Pseudo-First Order (PFO) and Intraparticle Diffusion (IPD).

MOF	PSO	PFO	IPD	Conditions
MOF-1[38] (Cd-MOF)	k_2=0.01379 g/mg·min q_e=39.573 mg/g R^2=0.99466	k_1=0.670 min^{-1} q_e=47.55104 mg/g R^2=0.97673	k_d=10.9904 mg/g·$min^{0.5}$ C=0 R^2=0.92411	MOF: 30 mg MB: 30 mL, 10^{-5} M
MOF-Fe[45]	k_2=0.006482 g/mg·min $q_{e,Exp}$=65.311 mg/g $q_{e,Cal}$=69.4444 mg/g R^2=0.9934	k_1=0.135 min^{-1} $q_{e,Exp}$=65.311 mg/g $q_{e,Cal}$=37.870 mg/g R^2=0.9521	Non-zero intercepts	MOF: 0.2 g/L MB: 1000 ppm pH=9
Amine-MOF-Fe[45]	k_2=0.013080 g/mg·min $q_{e,Exp}$=102.925 mg/g $q_{e,Cal}$=105.2632 mg/g R^2=0.9990	k_1=0.1778 min^{-1} $q_{e,Exp}$=102.925 mg/g $q_{e,Cal}$=30.718 mg/g R^2=0.9647	Non-zero intercepts	MOF: 0.2 g/L MB: 1000 ppm pH=9

MOF	PSO	PFO	IPD	Conditions
NH_2- MIL-125 (Ti)[90]	k_2=0.0005 g/mg·min $q_{e,Exp}$=397 mg/g $q_{e,Cal}$=455 mg/g R^2=0.9912	k_1=0.09 min^{-1} $q_{e,Exp}$=397 mg/g $q_{e,Cal}$=480 mg/g R^2=0.9602	k_d=45 mg/g·$min^{0.5}$ C=166 R^2=0.9122	MOF: 0.0050 g MB: N.A.
Amino-MIL-101(Al)[91]	k_2=2.6±1.3 g/mg·min q_e=762±12 mg/g R^2=0.999	k_1=(7±3) ·10^{-2} min^{-1} q_e=762±12 mg/g R^2=0.9		MOF: 5 mg MB: 100 mL, 40 ppm
MIL-100(Fe)[92]	k_2=0.409 g/mg·h $q_{e,Exp}$=22.9 mg/g $q_{e,Cal}$=22.9 mg/g R^2=0.9999	k_1=0.355 h^{-1} $q_{e,Exp}$=22.9 mg/g $q_{e,Cal}$=4.0 mg/g R^2=0.9273		MOF: 5 mg MB: 4 mL, 60 ppm
CuMOF-1[36]	k_2=0.0756 g/mg·min $q_{e,Exp}$=76.35 mg/g $q_{e,Cal}$=38.62 mg/g R^2=0.9906	k_1=0.0614 min^{-1} $q_{e,Exp}$=76.35 mg/g $q_{e,Cal}$=23.19 mg/g R^2=0.8467	k_d=15.4325 mg/g·$min^{0.5}$ C=0 R^2=0.9631	MOF: 30 mg MB: 30 mL, 10^{-5} M
CuMOF-2[36]	k_2=0.0396 g/mg·min $q_{e,Exp}$=82.15 mg/g $q_{e,Cal}$=74.51 mg/g R^2=0.99635	k_1=0.28478 min^{-1} $q_{e,Exp}$=82.15 mg/g $q_{e,Cal}$=64.36 mg/g R^2=0.96943	k_d=19.4563 mg/g·$min^{0.5}$ C=0 R^2=0.91559	MOF: 30 mg MB: 30 mL, 10^{-5} M
CP-1[39] (Cu-based)	k_2=0.019 g/mg·min $q_{e,Exp}$=30.30mg/g $q_{e,Cal}$=29.73 mg/g R^2=0.999	k_1=0.9384 min^{-1} $q_{e,Exp}$=5.195 mg/g $q_{e,Cal}$=29.73 mg/g R^2=0.985	k_d=1.54 mg/g·$min^{0.5}$ C=34.37 R^2=0.749	MOF: 25 mg MB: 75 mL, 10 ppm
SCNU-Z2[93] (Co-based)	k_2=0.0017 g/mg·min $q_{e,Exp}$=455.6mg/g $q_{e,Cal}$=55.01 mg/g R^2=0.9974	k_1=0.0319 min^{-1} $q_{e,Exp}$=455.6mg/g $q_{e,Cal}$=34.57 mg/g R^2=0.9759		MOF: 10 mg MB: 30 mL, 20 ppm
MIL-100(Fe)[94]	k_2=5.613·10^{-4} g/mg·h $q_{e,Exp}$=662.3 mg/g $q_{e,Cal}$=666.7 mg/g R^2=0.995			MOF: 10 mg MB: 50 mL, 400 ppm
MIL-100(Cr)[94]	k_2=0.001028 g/mg·h $q_{e,Exp}$=496.9 mg/g $q_{e,Cal}$=499.6 mg/g R^2=0.997			MOF: 10 mg MB: 50 mL, 400 ppm
5%GO/MIL-100(Fe)[95]	k_2=0.0008 g/mg·h $q_{e,Exp}$=1231 mg/g $q_{e,calc}$=1000 mg/g R^2=0.9949	k_1=0.1161 h^{-1} $q_{e,Exp}$=1231 mg/g $q_{e,calc}$=243.1 mg/g R^2=0.6143		MOF: 5 mg MB: 10 mL, C_0 N.A.

MOF	PSO	PFO	IPD	Conditions
PCN-222[96] (Zr-based)	k_2=1.072·10^{-3} g/mg·min $q_{e,Exp}$≈850 mg/g $q_{e,Cal}$=241.5 mg/g R^2=0.99996	k_1=0.1060 min^{-1} $q_{e,Exp}$≈850 mg/g $q_{e,Cal}$=892.9 mg/g R^2=0.94409		MOF: 5 mg MB: 5 mL, 1000 ppm
ZJU-71[97] (Cu-based)	k_2=0.00982 g/mg·min $q_{e,Exp}$=9.52 mg/g $q_{e,Cal}$=9.71 mg/g R^2=0.999			MOF: 5 mg MB: 10 mL, 5 ppm
Zn-MOF[98]	k_2=1.288·10^{-2} g/mg·min $q_{e,Exp}$=6.394 mg/g $q_{e,Cal}$=6.420 mg/g R^2=0.9998	k_1=4.864·10^{-3} min^{-1} $q_{e,Exp}$=6.394 mg/g $q_{e,Cal}$=2.697 mg/g R^2=0.6970		MOF: 2.6 mg MB: 2 mL, 10 ppm

.

5.3 Results and discussion

The adsorption of MB over Cu-YBDC was studied with a series of experiments described in chapter 2.5. All the experiments showed a similar trend in the variation of the absorbance (and therefore the concentration) over time, exemplified by the following graph (Fig. 5.2, experiment with 50 mg of Cu-YBDC in a starting solution of MB 40 ppm).

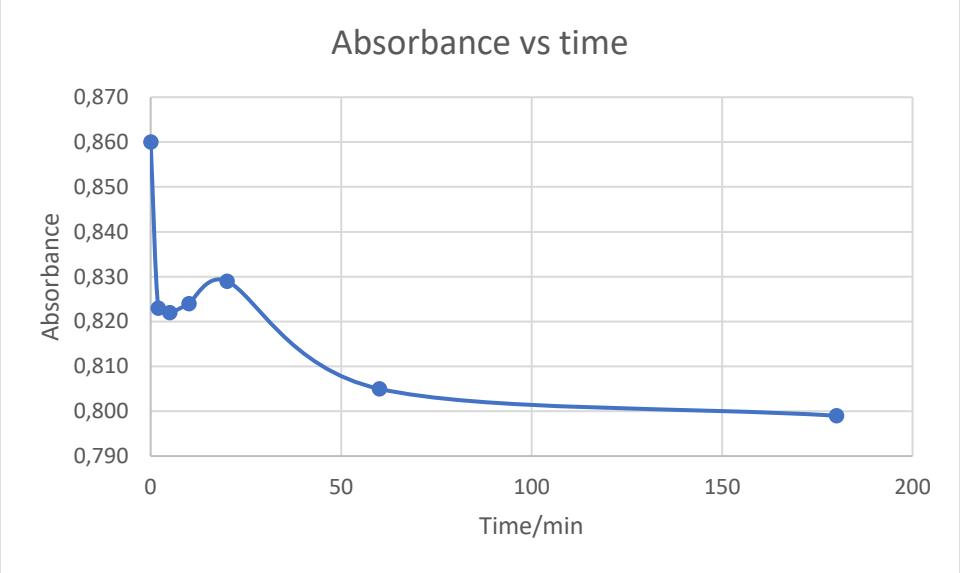

Fig. 5.2: Absorbance vs time graph of a 40 ppm Methylene Blue solution put in contact with 50 mg of Cu-MOF.

It is clearly visible that in the first minutes a fast decreasing in the absorbance occurs, followed by a small resurgence usually around 10 or 20 minutes. Finally, the absorbance settles down to a plateau, that fluctuates around the 90% of the starting value.

The graphs in Fig. 5.3 show the variation of q_t over time for the five experiments, obtained with the equation (1) (see chapter 1.5.6).

$$q_e = \frac{(C_0 - C_e)}{m} V \quad (1)$$

The trend seems to be the same seen for the Absorbance/Time graphs, with a fast adsorption in the first minutes, a small drop around the 10-20 minutes mark, and then a second increasing, which sometimes ends in a plateau (Fig. 3, panels A and C), and sometimes follows more irregular routes. Such unexpected results can be due to several reasons that are listed below.

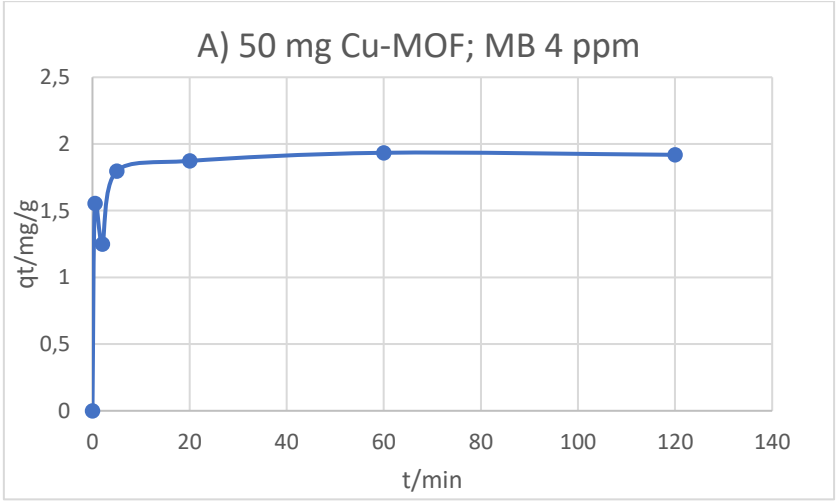

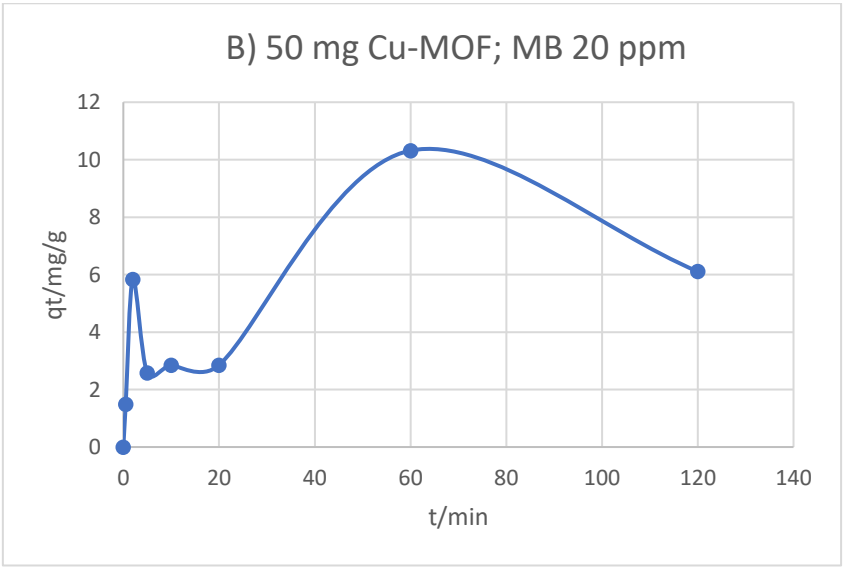

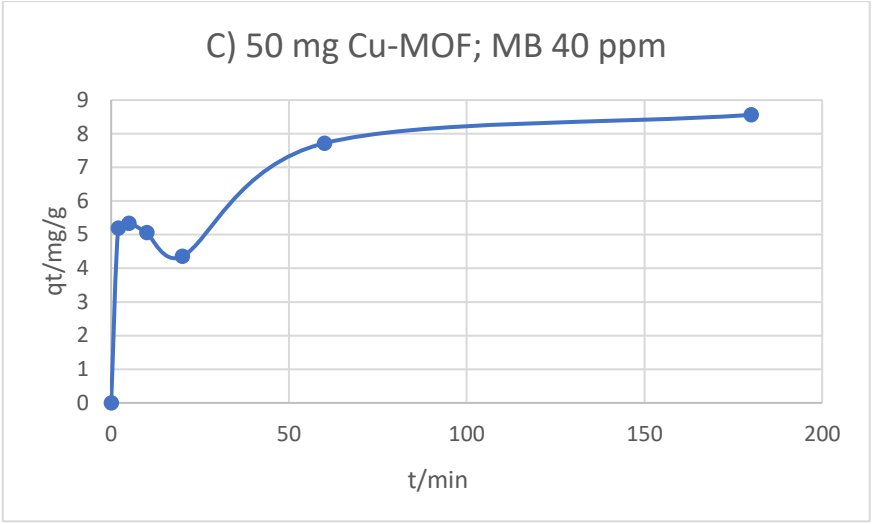

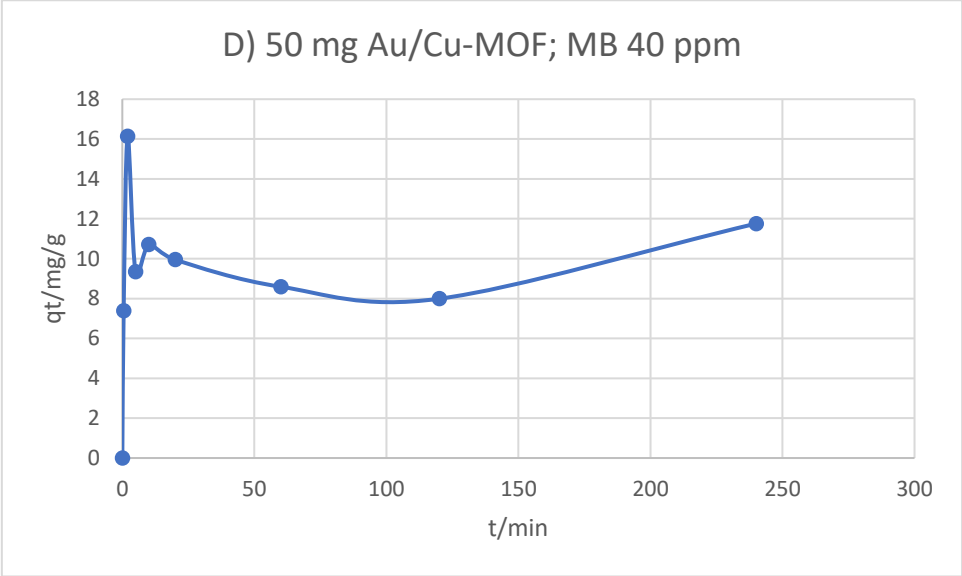

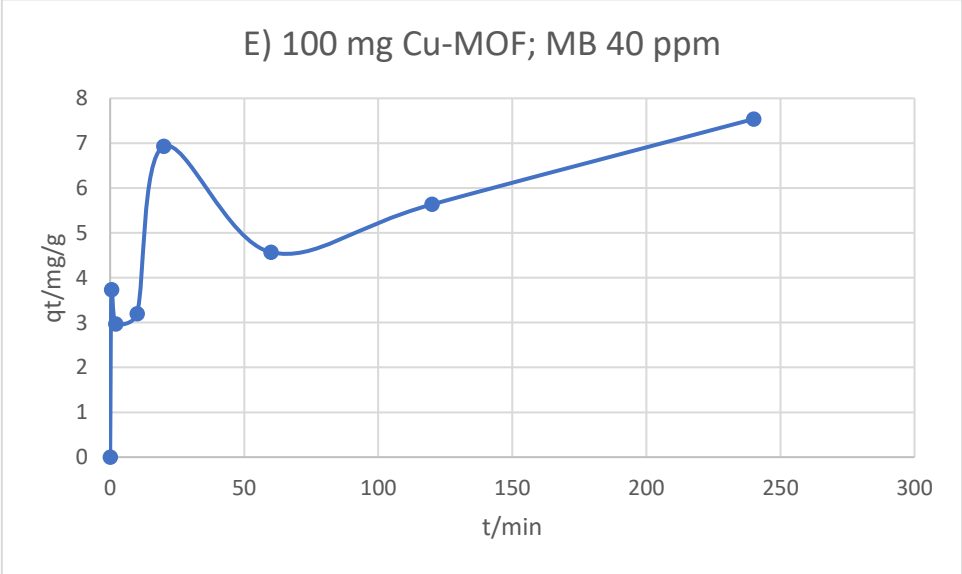

Fig. 5.3: Trends of q_t over time for the adsorption of MB in different conditions.

The first possibility is that the methodology employed for the experiments contains some biases. The use of equation (1) to calculate the values of q_t could be the first issue. Seeing that the adsorption capacity of the material is low, the value of (C_0-C_t) represents a small percentage of the initial C_0 value (especially for short time intervals), therefore even if the uncertainties on the measures of C_t and C_0 is small, the propagation of the uncertainties makes the value of (C_0-C_t) susceptible of greater errors. This hypothesis could explain the peculiar data obtained, especially the drop in the adsorption capacity observed in the first 10-20 minutes. To verify this hypothesis, each experiment should be repeated numerous times, in order to ascertain if any significant changes are present in the average curve. Other biases in the methodology could reside in the sample collection step. Even if we overlook the fact that it is quite difficult to collect samples with a homogeneous composition, due to the heterogeneity of the system, there is still the need to centrifugate the samples before analysing them, which requires a non-negligible time consumption. Due to the fast nature of the phenomena involved in the adsorption process, this time lapse could alter the results of the measurements, which could be no more representative of the actual characteristics of the system at the time of the extraction of the sample. This issue could be avoided by employing a different set-up for the experiment, which should allow to measure the absorbance of the solution *in situ*, for example by using an optical fibre spectrometer.

Another way to avoid the centrifugation step would be to separate the MOF from the solution through filtration. This method would be undeniably faster, but the drawback is that most of the commonly available filters tend to adsorb high quantities of MB, which leads to significant alteration of the measured absorbance values. Different recovery tests were performed with diverse types of filters (common filter paper, cellulose acetate filters with 0.45 μm pore size, polyamides filters with 0.45 μm pore size, polypropylene filters with 0.45 μm pore size, PES filters with 0.45 μm pore size), but all of them retained high quantities of MB (from the 15% to the 78% of the starting concentration) (an example of a recovery test is reported in Fig. 5.4). Should we find a different filter with more suitable properties, it could be a valid alternative to the centrifugation. In alternative, the possibility to saturate the filters with MB before the filtering of the samples, in order to eliminate the recovery could be taken into account.

Fig. 5.4: A 4 ppm solution of MB (cuvette on the left) was filtered with (from left to right): PES filter (green), Nylon (polyamide) filter (blue) and Polypropylene filter (white). The recovery values are respectively 78%, 14% and 55%.

Finally, the tests should be repeated with different stirring speeds, to verify if this parameter influences the adsorption performance.

Should these experiments confirm that the trend observed is representative of the adsorption mechanism (second scenario), we have to explain the peculiar shape of the graphs. The most unsettling aspect is the drop in the adsorption capacity that occurs after the first 10-20 minutes, and the following increasing that takes place after, that seems to indicate the presence of two or more subsequential adsorption phenomena. Considering that all the adsorption phenomena must take place on the external surface of the MOF, we can hypothesise the following sequence of events:

- In the first minutes, MB is adsorbed on the active sites of the external surface, and the system rapidly gets to the equilibrium;
- The adsorption causes some kind of modification of the nature of the active sites, therefore changing the equilibrium criteria, causing the temporary expulsion of part of the adsorbed MB;
- The new active sites begin to adsorb MB with different mechanisms and/or kinetics.

In this hypothetical model, the uncommon shape of the graphs could be explained by describing it as the combination of two or more curves, corresponding to the number of different adsorption mechanisms that take place. The changes in the equilibrium criteria that ideally happen during the switching from an adsorption mechanism to another, eventually causing the expulsion of

part of the adsorbed MB could explain the decreasing in the adsorption capacity that happens after 10-20.

To verify the validity of this model, the key point is to characterise the surface of the material after the various steps of the adsorption process (after the 10-20 minutes mark and after the final equilibrium) and check if there is any difference between them and the surface of the material before the adsorption. Considering the complexity of the surface of the MOF, it is not unlikely to imagine that the adsorption of MB could cause some structural changes on it. Different hypothesises have been proposed about the nature of those modifications, among which there are the conformational rearrangement of the propargyl-carbamate chain and a redox reaction between the carbamate group and the molecules of Methylene Blue.

5.4 Comparison with the literature

Due to the uncertainties concerning the experimental data, it is pointless to try any kind of curve-fitting with the kinetic models seen in chapter 1.5.7, therefore the only possible comparison with the literature data is the experimental adsorption capacity at equilibrium ($q_{e,Exp}$). In fact, the values of $q_{e,Exp}$ are the most reliable data, because they are the ones which are less touched by the possible methodological biases. In conditions of equilibrium, the difference between C_0 and C_t is larger, so the statistical error induced by the propagation of the uncertainties is less relevant compared to the measures taken at shorter time intervals. Also, in conditions of equilibrium the time lapse between the collection of the sample and the analysis should not significantly alter the results, because the adsorption process in the sample should not advance further compared to the bulk solution. In Table 5.2 we reported the values of $q_{e,Exp}$ obtained for the five experiments.

Table 5.2: Values of $q_{e,Exp}$ obtained for the adsorption of MB over Cu-[YBDC] in different conditions.

Experiment	$q_{e,Exp}$/mg·g^{-1}
A) 50 mg of Cu-MOF; 4 ppm MB solution	1.919
B) 50 mg of Cu-MOF; 20 ppm MB solution	6.109
C) 50 mg of Cu-MOF; 40 ppm MB solution	8.560
D) 50 mg of Au/Cu-MOF; 40 ppm MB solution	11.759
E) 100 mg of Cu-MOF; 40 ppm MB solution	7.538

The performances of [Cu(1,3-YBDC)]·xH$_2$O in the adsorption of MB are quite low, compared to the examples from the literature collected in Table 3.5. The best results in terms of $q_{e,Exp}$ were obtained in experiment C, where we had $q_{e,Exp}$=8.560 mg/g. This value is surpassed by almost every MOF in Table 3.5 except for Zn-MOF.[98] The $q_{e,Exp}$ increases a bit with the encapsulation of AuNPs (Experiment D). In this case we obtained $q_{e,Exp}$=11.759 mg/g, surpassing also ZJU-71.[97] This value is still not exceptional, considering that most of the other MOFs in the list possess $q_{e,Exp}$ values of two or three orders of magnitude higher. Those results are coherent with the starting observation that the pores of the material cannot participate in the adsorption process. Apparently, the functionalities that characterise the external surface of the MOF compensate only partially the lack of availability of the cavities of the material. Nevertheless, considering the problematics highlighted in the previous paragraph, further investigation is necessary.

Chapter 6

6 Conclusions and future work

6.1 Conclusions

The main results described in this thesis are summarised below.

- ✓ The new organic ligand 5'-(2-(((prop-2-yn-1-yloxy)carbonyl)amino)ethoxy)-[1,1':3',1''-terphenyl]-4,4''-dicarboxylic acid, abbreviated as H_2YL80 (Fig. 4.1), was designed, synthesised and fully characterised;

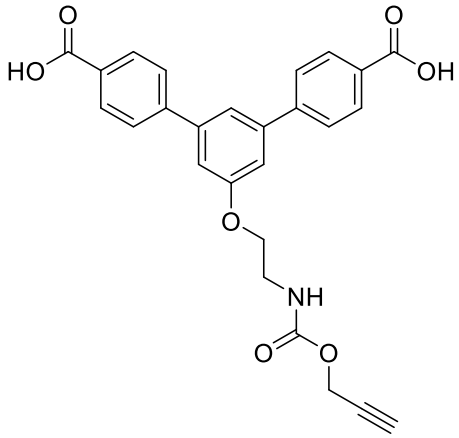

Fig. 6.1: Structure of the new H_2YL80 ligand.

- ✓ The new ligand was reacted with $Cu(NO_3)_2 \cdot 2.5H_2O$, in order to obtain a new Cu-based MOF. Having verified that the ligand and the Cu-salt react effectively with each other, different reaction conditions have been studied in order to obtain the desired product in satisfying yield and crystallinity. Currently, the best result obtained was a polycrystalline solid with a 70% yield;
- ✓ In parallel to those activities, the reactivity towards $HAuCl_4$ of the MOF [Cu-(1,3-YBDC)]$\cdot x H_2O$ was tested. It was demonstrated that the thermal treatment in alcohol of Cu-(1,3-YBDC)]$\cdot x H_2O$ impregnated with $HAuCl_4$ leads to the reduction of Au(III) to Au(0) and to Au(I), with the latter oxidation state as the predominant oxidation state leaving the morphology of the starting Cu-MOF substantially unchanged;
- ✓ Cu-(1,3-YBDC)]$\cdot x H_2O$ was also tested as an adsorbent material for the adsorption of Methylene Blue (MB) in different conditions. The preliminary data suggest that the adsorption performances of the MOF are limited, most likely due to the low porosity and surface area of the material, but they also highlight numerous potential issues with the experimental procedure.

6.2 Future work

Based on the results summarised in the previous paragraph, the future work will focus on the following issues:

- Study of new reaction conditions to obtain a new MOF from the new ligand and $Cu(NO_3)_2 \cdot 2.5H_2O$ in high yield and crystallinity, and fully characterise the new material;
- Test the new material for possible applications, including the ones studied for Cu-(1,3-YBDC)]$\cdot x H_2O$ (support of AuNPs and adsorption of MB);
- Improve the experimental procedure for the study of the adsorption of MB with Cu-(1,3-YBDC)]$\cdot x H_2O$.

BIBLIOGRAPHY

1. Parise C, Ballarin B, Barreca D, et al. Gold nanoparticles supported on functionalized silica as catalysts for alkyne hydroamination: A chemico-physical insight. *Appl Surf Sci*. 2019;492(March):45-54. doi:10.1016/j.apsusc.2019.05.192
2. Giorgetti M, Aquilanti G, Ballarin B, et al. Speciation of gold nanoparticles by Ex situ extended X-ray absorption fine structure and X-ray absorption near edge structure. *Anal Chem*. 2016;88(13):6873-6880. doi:10.1021/acs.analchem.6b01524
3. Fazzini S, Cassani MC, Ballarin B, et al. Novel synthesis of gold nanoparticles supported on alkyne-functionalized nanosilica. *J Phys Chem C*. 2014;118(42):24538-24547. doi:10.1021/jp507637m
4. Köberl M, Cokoja M, Herrmann WA, Kühn FE. From molecules to materials: Molecular paddle-wheel synthons of macromolecules, cage compounds and metal-organic frameworks. *Dalt Trans*. 2011;40(26):6834-6859. doi:10.1039/c0dt01722a
5. Cassani MC, Gambassi F, Ballarin B, et al. A Cu(ii)-MOF based on a propargyl carbamate-functionalized isophthalate ligand . *RSC Adv*. 2021;11(33):20429-20438. doi:10.1039/d1ra02686k
6. Lee YR, Kim J, Ahn WS. Synthesis of metal-organic frameworks: A mini review. *Korean J Chem Eng*. 2013;30(9):1667-1680. doi:10.1007/s11814-013-0140-6
7. Ghasempour H, Wang KY, Powell JA, et al. Metal–organic frameworks based on multicarboxylate linkers. *Coord Chem Rev*. 2021;426:213542. doi:10.1016/j.ccr.2020.213542
8. Seth S, Matzger AJ. Metal-Organic Frameworks: Examples, Counterexamples, and an Actionable Definition. *Cryst Growth Des*. 2017;17(8):4043-4048. doi:10.1021/acs.cgd.7b00808
9. Hoskin, BF; Robson R. Design and Construction of a New Class of Scaffolding-like Materials Comprising Infinite Polymeric Frameworks of 3D-Linked Molecular Rods. A Reappraisal of the Zn(CN)2 and Cd(CN)2 Structures and the Synthesis and Structure of the Diamond-Related Framework. *J Am Chem Soc*. 1990;112:1546-1554.
10. Yaghi OM, Li G, Li Hailian. Yaghi-Selective binding and removal of guests in a imcroporous metal-organic framework-Nature 1985. *Nature*. 1995;378(December):703-706.
11. Rungtaweevoranit B, Diercks CS, Kalmutzki MJ, Yaghi OM. Spiers Memorial Lecture:: Progress and prospects of reticular chemistry. *Faraday Discuss*. 2017;201:9-45. doi:10.1039/c7fd00160f

12. Yaghi OM, Kalmutzki MJ, Diercks CS. *Introduction to Reticular Chemistry*.; 2019. doi:10.1002/9783527821099
13. Stock N, Biswas S. Synthesis of metal-organic frameworks (MOFs): Routes to various MOF topologies, morphologies, and composites. *Chem Rev*. 2012;112(2):933-969. doi:10.1021/cr200304e
14. Robin AY, Fromm KM. Coordination polymer networks with O- and N-donors: What they are, why and how they are made. *Coord Chem Rev*. 2006;250(15-16):2127-2157. doi:10.1016/j.ccr.2006.02.013
15. Chen Z, Wasson MC, Drout RJ, et al. The state of the field: From inception to commercialization of metal-organic frameworks. *Faraday Discuss*. 2021;225:9-69. doi:10.1039/d0fd00103a
16. Mondloch JE, Karagiaridi O, Farha OK, Hupp JT. Activation of metal-organic framework materials. *CrystEngComm*. 2013;15(45):9258-9264. doi:10.1039/c3ce41232f
17. Howarth AJ, Peters AW, Vermeulen NA, Wang TC, Hupp JT, Farha OK. Best practices for the synthesis, activation, and characterization of metal−organic frameworks. *Chem Mater*. 2017;29(1):26-39. doi:10.1021/acs.chemmater.6b02626
18. Zhang X, Chen Z, Liu X, et al. A historical overview of the activation and porosity of metal-organic frameworks. *Chem Soc Rev*. 2020;49(20):7406-7427. doi:10.1039/d0cs00997k
19. Ma S, Zhou HC. Gas storage in porous metal-organic frameworks for clean energy applications. *Chem Commun*. 2010;46(1):44-53. doi:10.1039/b916295j
20. Kapelewski MT, Runčevski T, Tarver JD, et al. Record High Hydrogen Storage Capacity in the Metal-Organic Framework Ni2(m-dobdc) at Near-Ambient Temperatures. *Chem Mater*. 2018;30(22):8179-8189. doi:10.1021/acs.chemmater.8b03276
21. Shahnawaz Khan M, Khalid M, Shahid M. What triggers dye adsorption by metal organic frameworks? The current perspectives. *Mater Adv*. 2020;1(6):1575-1601. doi:10.1039/d0ma00291g
22. Millward AR, Yaghi OM. Metal-organic frameworks with exceptionally high capacity for storage of carbon dioxide at room temperature. *J Am Chem Soc*. 2005;127(51):17998-17999. doi:10.1021/ja0570032
23. Rieth AJ, Dinca M. Controlled Gas Uptake in Metal-Organic Frameworks with Record Ammonia Sorption. *J Am Chem Soc*. 2018;140(9):3461-3466. doi:10.1021/jacs.8b00313
24. Adil K, Belmabkhout Y, Pillai RS, et al. Gas/vapour separation using ultra-microporous

metal-organic frameworks: Insights into the structure/separation relationship. *Chem Soc Rev*. 2017;46(11):3402-3430. doi:10.1039/c7cs00153c

25. Duan X, Song R, Yu J, et al. A new microporous metal-organic framework with open metal sites and exposed carboxylic acid groups for selective separation of CO2/CH 4 and C2H2/CH4. *RSC Adv*. 2014;4(69):36419-36424. doi:10.1039/c4ra07246d
26. Copéret C, Comas-Vives A, Conley MP, et al. Surface Organometallic and Coordination Chemistry toward Single-Site Heterogeneous Catalysts: Strategies, Methods, Structures, and Activities. *Chem Rev*. 2016;116(2):323-421. doi:10.1021/acs.chemrev.5b00373
27. Otake KI, Cui Y, Buru CT, Li Z, Hupp JT, Farha OK. Single-Atom-Based Vanadium Oxide Catalysts Supported on Metal-Organic Frameworks: Selective Alcohol Oxidation and Structure-Activity Relationship. *J Am Chem Soc*. 2018;140(28):8652-8656. doi:10.1021/jacs.8b05107
28. García-García P, Müller M, Corma A. MOF catalysis in relation to their homogeneous counterparts and conventional solid catalysts. *Chem Sci*. 2014;5(8):2979-3007. doi:10.1039/c4sc00265b
29. Cordova KE, Yaghi OM. The "folklore" and reality of reticular chemistry. *Mater Chem Front*. 2017;1(7):1304-1309. doi:10.1039/c7qm00144d
30. Online VA. BASF Metal Organic Frameworks (MOFs): Innovative Fuel Systems for Natural Gas Vehicles (NGVs). *Chem Soc Rev*. 2014;43(16):6173-6174. doi:10.1039/c4cs90070g
31. Tchinsa A, Hossain MF, Wang T, Zhou Y. Removal of organic pollutants from aqueous solution using metal organic frameworks (MOFs)-based adsorbents: A review. *Chemosphere*. Published online 2021:131393. doi:10.1016/j.chemosphere.2021.131393
32. Rojas S, Horcajada P. Metal-Organic Frameworks for the Removal of Emerging Organic Contaminants in Water. *Chem Rev*. 2020;120(16):8378-8415. doi:10.1021/acs.chemrev.9b00797
33. Dias EM, Petit C. Towards the use of metal-organic frameworks for water reuse: A review of the recent advances in the field of organic pollutants removal and degradation and the next steps in the field. *J Mater Chem A*. 2015;3(45):22484-22506. doi:10.1039/c5ta05440k
34. Xiao Z, Zhou J, Fan L, et al. Controllable Preparation of Cu-MOF-Coated Carboxyl Filter Paper for Simultaneous Removal of Organic Dye and Metal Ions. *Ind Eng Chem Res*. Published online 2021. doi:10.1021/acs.iecr.1c00140
35. Russo V, Hmoudah M, Broccoli F, Iesce MR, Jung O-S, Di Serio M. Applications of

Metal Organic Frameworks in Wastewater Treatment: A Review on Adsorption and Photodegradation. *Front Chem Eng*. 2020;2(October):1-13. doi:10.3389/fceng.2020.581487

36. Iman K, Shahid M, Khan MS, Ahmad M, Sama F. Topology, magnetism and dye adsorption properties of metal organic frameworks (MOFs) synthesized from bench chemicals. *CrystEngComm*. 2019;21(35):5299-5309. doi:10.1039/c9ce01041f
37. Wang S, Peng Y. Natural zeolites as effective adsorbents in water and wastewater treatment. *Chem Eng J*. 2010;156(1):11-24. doi:10.1016/j.cej.2009.10.029
38. Wu WP, Wu J, Liu JQ, Trivedi M, Kumar A. Fabrication of a new metal-organic framework for sensitive sensing of nitroaromatics and efficient dye adsorption. *RSC Adv*. 2017;7(86):54522-54531. doi:10.1039/c7ra11221a
39. Khan MS, Khalid M, Ahmad MS, Shahid M, Ahmad M. Three-in-one is really better: Exploring the sensing and adsorption properties in a newly designed metal-organic system incorporating a copper(II) ion. *Dalt Trans*. 2019;48(34):12918-12932. doi:10.1039/c9dt02578b
40. Au VKM. Recent Advances in the Use of Metal-Organic Frameworks for Dye Adsorption. *Front Chem*. 2020;8(August):1-7. doi:10.3389/fchem.2020.00708
41. Li L, Liu XL, Geng HY, Hu B, Song GW, Xu ZS. A MOF/graphite oxide hybrid (MOF: HKUST-1) material for the adsorption of methylene blue from aqueous solution. *J Mater Chem A*. 2013;1(35):10292-10299. doi:10.1039/c3ta11478c
42. Lange LE, Obendorf SK. Functionalization of cotton fiber by partial etherification and self-assembly of polyoxometalate encapsulated in Cu3(BTC)2 metal-organic framework. *ACS Appl Mater Interfaces*. 2015;7(7):3974-3980. doi:10.1021/am506510q
43. Denny MS, Kalaj M, Bentz KC, Cohen SM. Multicomponent metal-organic framework membranes for advanced functional composites. *Chem Sci*. 2018;9(47):8842-8849. doi:10.1039/c8sc02356e
44. Ma X, Wang W, Sun C, Li H, Sun J, Liu X. Adsorption performance and kinetic study of hierarchical porous Fe-based MOFs for toluene removal. *Sci Total Environ*. 2021;793(17923):148622. doi:10.1016/j.scitotenv.2021.148622
45. Paiman SH, Rahman MA, Uchikoshi T, et al. Functionalization effect of Fe-type MOF for methylene blue adsorption. *J Saudi Chem Soc*. 2020;24(11):896-905. doi:10.1016/j.jscs.2020.09.006
46. Ersali S, Hadadi V, Moradi O, Fakhri A. Pseudo-second-order kinetic equations for modeling adsorption systems for removal of ammonium ions using multi-walled carbon

nanotube. *Fullerenes, Nanotub Carbon Nanostructures*. Published online 2013:150527104639002. doi:10.1080/1536383x.2013.787610

47. Xiao Y, Azaiez J, Hill JM. Erroneous Application of Pseudo-Second-Order Adsorption Kinetics Model: Ignored Assumptions and Spurious Correlations. *Ind Eng Chem Res*. 2018;57(7):2705-2709. doi:10.1021/acs.iecr.7b04724
48. Hubbe, M.A.; Azizian, S., Douven S. Implications of Apparent Pseudo-Second-Order Adsorption Kinetics onto Cellulosic Materials: A Review. *BioResources*. Published online 2019:7582-7626. https://ojs.cnr.ncsu.edu/index.php/BioRes/article/view/BioRes_14_3_Hubbe_Review_Apparent_Pseudo_Second_Order_Adsorption
49. Lin J, Wang L. Comparison between linear and non-linear forms of pseudo-first-order and pseudo-second-order adsorption kinetic models for the removal of methylene blue by activated carbon. *Front Environ Sci Eng China*. 2009;3(3):320-324. doi:10.1007/s11783-009-0030-7
50. Wu FC, Tseng RL, Huang SC, Juang RS. Characteristics of pseudo-second-order kinetic model for liquid-phase adsorption: A mini-review. *Chem Eng J*. 2009;151(1-3):1-9. doi:10.1016/j.cej.2009.02.024
51. Canzano S, Iovino P, Leone V, Salvestrini S, Capasso S. Use and misuse of sorption kinetic data: A common mistake that should be avoided. *Adsorpt Sci Technol*. 2012;30(3):217-225. doi:10.1260/0263-6174.30.3.217
52. Simonin JP. On the comparison of pseudo-first order and pseudo-second order rate laws in the modeling of adsorption kinetics. *Chem Eng J*. 2016;300:254-263. doi:10.1016/j.cej.2016.04.079
53. Ho YS, Mckay G, Hong T, Bay W, Kong H, Hong T. Separation & Purification Reviews Kinetics of Pollutant Sorption by Biosorbents : Review. *Sep Purif Rev*. 2000;29(2):189-232.
54. Wu FC, Tseng RL, Juang RS. Initial behavior of intraparticle diffusion model used in the description of adsorption kinetics. *Chem Eng J*. 2009;153(1-3):1-8. doi:10.1016/j.cej.2009.04.042
55. Low KS, Lee CK, Tan KK. Biosorption of basic dyes by water hyacinth roots. *Bioresour Technol*. 1995;52(1):79-83. doi:10.1016/0960-8524(95)00007-2
56. Ali RM, Hamad HA, Hussein MM, Malash GF. Potential of using green adsorbent of heavy metal removal from aqueous solutions: Adsorption kinetics, isotherm, thermodynamic, mechanism and economic analysis. *Ecol Eng*. 2016;91:317-332.

doi:10.1016/j.ecoleng.2016.03.015

57. Liu Y, Kang Y, Mu B, Wang A. Attapulgite/bentonite interactions for methylene blue adsorption characteristics from aqueous solution. *Chem Eng J*. 2014;237:403-410. doi:10.1016/j.cej.2013.10.048
58. Cassani MC, Castagnoli R, Gambassi F, et al. A cu(Ii)-mof based on a propargyl carbamate-functionalized isophthalate ligand as nitrite electrochemical sensor. *Sensors*. 2021;21(14):1-15. doi:10.3390/s21144922
59. Zhang YM, Yang LZ, Lin Q, Wei TB. Preparation and crystal structure of a new Cu(II) complex of the N-ethoxycarbonyl-O-ethyl-N′-(2,4,6-trichlorophenyl)-isourea. *Transit Met Chem*. 2005;30(8):944-947. doi:10.1007/s11243-005-6245-y
60. Abourahma H, Bodwell GJ, Lu J, et al. Coordination polymers from calixarene-like [Cu 2(dicarboxylate)2]4 building blocks: Structural diversity via atropisomerism. *Cryst Growth Des*. 2003;3(4):513-519. doi:10.1021/cg0340345
61. Sakata Y, Furukawa S, Kondo M, et al. Shape-memory nanopores induced in coordination frameworks by crystal downsizing. *Science (80-)*. 2013;339(6116):193-196. doi:10.1126/science.1231451
62. Düren T, Millange F, Férey G, Walton KS, Snurr RQ. Calculating geometric surface areas as a characterization tool for metal - Organic frameworks. *J Phys Chem C*. 2007;111(42):15350-15356. doi:10.1021/jp074723h
63. Yuan B, Zhang J, Zhang R, et al. Cu-based metal-organic framework as a novel sensing platform for the enhanced electro-oxidation of nitrite. *Sensors Actuators, B Chem*. 2016;222:632-637. doi:10.1016/j.snb.2015.08.100
64. Mani V, Periasamy AP, Chen SM. Highly selective amperometric nitrite sensor based on chemically reduced graphene oxide modified electrode. *Electrochem commun*. 2012;17(1):75-78. doi:10.1016/j.elecom.2012.02.009
65. WHO. Nitrate and nitrite in drinking water: background document for development of WHO guidelines for drinking water quality. *Geneva World Heal Organ*. Published online 2016:31. http://www.who.int/publications/guidelines/%0Ahttp://www.who.int/water_sanitation_health/dwq/chemicals/nitratenitrite2ndadd.pdf
66. Briggs D, Wiley J. Practical Surface Analysis By Auger and X-Ray Photoelectron Spectroscopy. *Pr Surf Anal by Auger X-ray Photoelectron Spectrosc*. 1983;1:1-8. doi:10.1016/0368-2048(84)80044-4
67. Shirley DA. High-resolution x-ray photoemission spectrum of the valence bands of gold.

Phys Rev B. 1972;5(12):4709-4714. doi:10.1103/PhysRevB.5.4709

68. L'Hermite N, Peyrat JF, Alami M, Brion JD. Synthesis and characterization of low generation halogenated linear poly(arylpropargyl)ether (PAPE) branches via selective palladium catalyzed coupling reactions. *Tetrahedron Lett*. 2005;46(52):8987-8991. doi:10.1016/j.tetlet.2005.10.110
69. Ruengsangtongkul S, Chaisan N, Thongsornkleeb C, Tummatorn J, Ruchirawat S. Rate Enhancement in CAN-Promoted Pd(PPh 3) 2 Cl 2 -Catalyzed Oxidative Cyclization: Synthesis of 2-Ketofuran-4-carboxylate Esters. *Org Lett*. 2019;21(8):2514-2517. doi:10.1021/acs.orglett.9b00053
70. Chen Z, Weseliński ŁJ, Adil K, et al. Applying the Power of Reticular Chemistry to Finding the Missing alb-MOF Platform Based on the (6,12)-Coordinated Edge-Transitive Net. *J Am Chem Soc*. 2017;139(8):3265-3274. doi:10.1021/jacs.7b00219
71. Rivera-Torrente M, Mandemaker LDB, Filez M, et al. Spectroscopy, microscopy, diffraction and scattering of archetypal MOFs: Formation, metal sites in catalysis and thin films. *Chem Soc Rev*. 2020;49(18):6694-6732. doi:10.1039/d0cs00635a
72. Campbell J, Tokay B. Controlling the size and shape of Mg-MOF-74 crystals to optimise film synthesis on alumina substrates. *Microporous Mesoporous Mater*. 2017;251:190-199. doi:10.1016/j.micromeso.2017.05.058
73. Azhar MR, Hussain G, Tade MO, Silvester DS, Wang S. Electrodeposited Metal Organic Framework toward Excellent Hydrogen Sensing in an Ionic Liquid. *ACS Appl Nano Mater*. 2020;3(5):4376-4385. doi:10.1021/acsanm.0c00503
74. J.F. Moulder, W.F. Stickle, P.E. Sobol KDB. *Handbook of X-Ray Photoelectron Spectroscopy (XPS)*. (Eden Prairie, MN U, ed.). Perkin Elmer Corporation; 1992.
75. https://srdata.nist.gov/xps/.
76. Barreca D, Gasparotto A, Tondello E. CVD Cu2O and CuO nanosystems characterized by XPS. *Surf Sci Spectra*. 2007;14. doi:10.1116/11.20080701
77. Barreca D, Gasparotto A, Maccato C, Tondello E, Lebedev OI, Tendeloo G Van. CVD of copper oxides from a β-diketonate diamine precursor: Tailoring the nano-organization. *Cryst Growth Des*. 2009;9(5):2470-2480. doi:10.1021/cg801378x
78. Li X, Wan J, Ma Y, Zhao JR, Wang Y. Mesopores octahedron GCNOX/Cu2O@C inhibited photo-corrosion as an efficient visible-light catalyst derived from oxidized g-C3N4/HKUST-1 composite structure. *Appl Surf Sci*. 2020;510(August 2019):145459. doi:10.1016/j.apsusc.2020.145459
79. Zhao X, Wu W, Jing G, Zhou Z. Activation of sulfite autoxidation with CuFe2O4

prepared by MOF-templated method for abatement of organic contaminants. *Environ Pollut*. 2020;260:114038. doi:10.1016/j.envpol.2020.114038

80. Taher A, Kim DW, Lee IM. Highly efficient metal organic framework (MOF)-based copper catalysts for the base-free aerobic oxidation of various alcohols. *RSC Adv*. 2017;7(29):17806-17812. doi:10.1039/c6ra28743c
81. Senthil Kumar R, Senthil Kumar S, Anbu Kulandainathan M. Efficient electrosynthesis of highly active Cu3(BTC) 2-MOF and its catalytic application to chemical reduction. *Microporous Mesoporous Mater*. 2013;168:57-64. doi:10.1016/j.micromeso.2012.09.028
82. Barreca D, Carraro G, Gasparotto A. CuxO - TiO2 Composites (x=1, 2) Studied by X-ray Photoelectron Spectroscopy. *Surf Sci Spectra*. 2009;16(1):1-12. doi:10.1116/11.20110101
83. Chen C, Wu T, Yang D, et al. Catalysis of photooxidation reactions through transformation between Cu2+ and Cu+ in TiO2-Cu-MOF composites. *Chem Commun*. 2018;54(47):5984-5987. doi:10.1039/c8cc03505a
84. Ballarin B, Barreca D, Boanini E, et al. Supported Gold Nanoparticles for Alcohols Oxidation in Continuous-Flow Heterogeneous Systems. *ACS Sustain Chem Eng*. 2017;5(6):4746-4756. doi:10.1021/acssuschemeng.7b00133
85. Rubinos DA, Soto B. Effect of Mineral-Organic-Microorganism Interactions on Soil and Freshwater Environments. *Eff Miner Interact Soil Freshw Environ*. 1999;(January). doi:10.1007/978-1-4615-4683-2
86. Rafatullah M, Sulaiman O, Hashim R, Ahmad A. Adsorption of methylene blue on low-cost adsorbents: A review. *J Hazard Mater*. 2010;177(1-3):70-80. doi:10.1016/j.jhazmat.2009.12.047
87. Koch R. Some Drugs and Herbal Products. *IARC Monogr Eval Carcinog risks to humans*. 2016;108:7-419.
88. Mengting Z, Kurniawan TA, Fei S, et al. Applicability of BaTiO3/graphene oxide (GO) composite for enhanced photodegradation of methylene blue (MB) in synthetic wastewater under UV–vis irradiation. *Environ Pollut*. 2019;255. doi:10.1016/j.envpol.2019.113182
89. Italian Official Gazette n. 88 del 14 April 2006 - suppl. ord. n. 96. D. Lgs 152/06 (Parte terza, Allegato 5, Tabella 3.) - Valori limiti di emissioni in acque superficiali e in fognatura. 2006;(02):1-3.
90. Oveisi M, Asli MA, Mahmoodi NM. MIL-Ti metal-organic frameworks (MOFs)

nanomaterials as superior adsorbents: Synthesis and ultrasound-aided dye adsorption from multicomponent wastewater systems. *J Hazard Mater*. 2018;347:123-140. doi:10.1016/j.jhazmat.2017.12.057

91. Haque E, Lo V, Minett AI, Harris AT, Church TL. Dichotomous adsorption behaviour of dyes on an amino-functionalised metal-organic framework, amino-MIL-101(Al). *J Mater Chem A*. 2014;2(1):193-203. doi:10.1039/c3ta13589f
92. Jia Y, Jin Q, Li Y, Sun Y, Huo J, Zhao X. Investigation of the adsorption behaviour of different types of dyes on MIL-100(Fe) and their removal from natural water. *Anal Methods*. 2015;7(4):1463-1470. doi:10.1039/c4ay02726d
93. Deng SQ, Miao YL, Tan YL, et al. An Anionic Nanotubular Metal-Organic Framework for High-Capacity Dye Adsorption and Dye Degradation in Darkness. *Inorg Chem*. 2019;58(20):13979-13987. doi:10.1021/acs.inorgchem.9b01959
94. Tong M, Liu D, Yang Q, Devautour-Vinot S, Maurin G, Zhong C. Influence of framework metal ions on the dye capture behavior of MIL-100 (Fe, Cr) MOF type solids. *J Mater Chem A*. 2013;1(30):8534-8537. doi:10.1039/c3ta11807j
95. Luo S, Wang J. MOF/graphene oxide composite as an efficient adsorbent for the removal of organic dyes from aqueous solution. *Environ Sci Pollut Res*. 2018;25(6):5521-5528. doi:10.1007/s11356-017-0932-z
96. Li H, Cao X, Zhang C, et al. Enhanced adsorptive removal of anionic and cationic dyes from single or mixed dye solutions using MOF PCN-222. *RSC Adv*. 2017;7(27):16273-16281. doi:10.1039/c7ra01647f
97. Duan X, Yu J, Zhang Q, Cui Y, Yang Y, Qian G. A new anionic metal-organic framework for highly efficient removal of cationic pollutant in water. *Mater Lett*. 2016;185(3):177-180. doi:10.1016/j.matlet.2016.08.137
98. Zhang J, Li F, Sun Q. Rapid and selective adsorption of cationic dyes by a unique metal-organic framework with decorated pore surface. *Appl Surf Sci*. 2018;440:1219-1226. doi:10.1016/j.apsusc.2018.01.258

Acknowledgments

This work is not the effort of a single individual but represents the result of an incredible teamwork by a wonderful group of people. Therefore, I wish to give my heartful thanks to all the members of this group: my supervisor, Professor Maria Cristina Cassani, for having warmly welcomed me into the team and for the infinite dedication and care towards my work; my tutor Francesca Gambassi, for the patience, the kindness, the precious teachings and the tireless guidance given to me during these months; Professor Barbara Ballarin and Professor Daniele Nanni for their wise advices; Ilaria Ragazzini, whose affection and steaming Rock and Roll attitude lifted off a lot of the weight from the long hours of work; Riccardo Castagnoli, the true giant on whose shoulders this work stands.

A huge thanks goes also to Professor Elisa Boanini of the Department of Chemical Sciences of the University of Bologna, to Professor Davide Barreca and Professor Chiara Maccato of the Department of Chemical Sciences of the University of Padova, to Dr. Alessandro Kovtun of CNR-IMM, and to Dr. Norberto Masciocchi of the Institute of Crystallography, To.Sca.Lab, University of Insubria, whose precious collaboration is always vital for the works of the group.

A special thanks goes to Professor Davide Pinelli and Professor Ivano Vassura whose illuminated insights have been extremely useful for the redaction of this thesis.

The years of the master's degree are usually a time of great challenges, changes, and uncertainties, which can be tough at times, even in normal situations. In our case, those years happened in the middle of a period that has been all but normal, but I was lucky enough to have shared those years with many people who made the difficulties less heavy.

First of all, my family, which I do not define exclusively in terms of blood ties, but more in terms of heart ties, as cheesy as it may sound.

Then, my course-mates who shared with me the stress of these confusing and chaotic months of online lessons, exams, and paper works, always finding a way to have a laugh about the surreal situations we found ourselves in. An honourable mention to the hardcore-Venezio fanbase, inexhaustible source of memes and jokes.

Finally, all the wonderful friends I made along the years, who in some way or another have supported me, showed me their love in various shapes, and endured my ramblings about chemistry, philosophy, the Meaning of Life, the existence of God, Cedrata Tassoni, obscure Japanese doom metal bands, and intricated Star Wars lore. It would take me an entire semester to list them all, but I am sure they know who they are.

To all of you, my infinite gratitude.

May the Force be with you. Michele